Microscopic Structure of Plasma Turbulence in the Torsatron TJ-K

Dissertation zur Erlangung des Doktorgrades der
Mathematisch-Naturwissenschaftlichen Fakultät der
Christian-Albrechts-Universität zu Kiel

vorgelegt von
Carsten Lechte
Kiel, 2003

Referent/in: _____

Korreferent/in: _____

Tag der mündlichen Prüfung: _____

Zum Druck genehmigt: Kiel, _____

Zusammenfassung

Turbulenz kommt in vielen Gasen, Flüssigkeiten und Plasmen vor und ist bis heute nicht vollständig verstanden. Sie äußert sich in Fluktuationen von Größen wie Dichte, Druck, Temperatur und Flussgeschwindigkeit auf allen Zeit- und Raumskalen, in Plasmen kommen noch Fluktuationen der elektrischen und magnetischen Felder dazu. Speziell in magnetisch eingeschlossenen Plasmen führt Turbulenz dazu, dass ein erhöhter Teilchen- und Energietransport senkrecht zum einschließenden Feld stattfindet, der es unmöglich gemacht hat, mit bisherigen Fusionsexperimenten einen technisch nutzbaren Energieüberschuss zu erzielen.

Die experimentelle Untersuchung turbulenter Plasmen in Fusionsgeometrie ist der Gegenstand dieser Arbeit. Das Besondere am Kieler Torsatron TJ-K sind seine relative kalten Plasmen, die diagnostische Techniken ermöglichen, die an heißen Fusionsplasmen nicht zur Verfügung stehen. So können Dichte, Potential und turbulenter Transport mit Vielfach-Sondenanordnungen im Einschlussbereich des Plasmas gemessen werden. Die daraus gewonnenen Wellenzahlspektren geben Aufschluss über die räumlichen Skalen, auf denen Fluktuationen und Transport stattfinden. Ein einfaches Skalierungsgesetz für die Größer dieser Skalen wurde gefunden.

Von besonderem Interesse ist die Kreuzphase zwischen Dichte- und Potentialfluktuationen. Zum Einen ist sie Ausschlag gebend für die Größe des turbulenten Transports, zum Anderen erlaubt sie die Unterscheidung zwischen den zwei wichtigsten Instabilitäten, die in TJ-K betrachtet werden. Die in TJ-K gefundene Kreuzphase von ungefähr null weist auf die Driftwelleninstabilität hin, während eine Phase um $\pi/2$ zur Austauschinstabilität gehört.

Die Ergebnisse der Vielfach-Sondenmessungen werden mit Ergebnissen aus Simulationsrechnungen verglichen, die im Rahmen einer anderen Doktorarbeit entstanden sind.

Schließlich kann mit der Methode der konditionellen Mittelung mit einfachen Zwei-Punkt-Messungen ebenfalls der raum-zeitliche Verlauf von turbulenten Strukturen detektiert werden. Dieser stimmt mit den Ergebnissen aus den Wellenzahlspektren überein.

Abstract

Turbulence is observed in many gases, fluids and plasmas and it is still not totally understood. It is characterised by the fluctuation on all temporal and spatial scales of quantities such as flow velocity, density, pressure, temperature and, in the case of plasma turbulence, of the electric and magnetic fields. In the special case of magnetically confined plasmas, turbulence causes an increased particle and heat transport across the magnetic field lines. This is responsible for the inability of today's fusion experiments to deliver an energy surplus for electricity generation.

The focus of this work is the experimental investigation of turbulent plasmas in fusion geometry. The torsatron TJ-K has relatively moderate plasma parameters, which allow diagnostic techniques to be employed that are unavailable in hot fusion plasmas. Density, potential and mean transport in the confinement region are measured using Langmuir probe arrays. The wave number spectra gathered from the data give insight into the spatial scales of plasma fluctuations and transport. A simple scaling law for the size of these scales is found.

The cross phase between density and potential fluctuations is of special interest, because it determines the level of turbulent transport. Its value also allows to distinguish between the two major instabilities that are considered in TJ-K. The observed cross phase of zero indicates that the drift wave instability is the dominant turbulent mechanism in TJ-K. A cross phase of $\pi/2$ is associated with the interchange instability.

The results of the probe array are compared with results from turbulence simulations, that were carried out in a different PhD. thesis.

Finally, the conditional averaging method was used to detect the spatio-temporal structure of turbulent events with simple two probe measurements. The results are in agreement with the results from the probe array.

Contents

Chapter 1

Introduction

Turbulence is observed in many gases, fluids and plasmas. It is characterised by the fluctuation on all temporal and spatial scales of quantities such as flow velocity, density, pressure, temperature and, in the case of plasma turbulence, of the electric and magnetic fields. Turbulence has been investigated as early as Leonardo da Vinci and is still not totally understood [1, 2, 3, 4, 5]. Although the basic equations (Navier-Stokes for fluids, magneto-hydrodynamic equations for plasmas) are well-known, the host of possible phenomena is overwhelming. This arises out of the fact that one is dealing with a many-body system that has an infinite number of degrees of freedom represented by partial differential equations, in contrast to a chaotic system, which at a first glance shows similar traits, but which can be represented by a few *ordinary* differential equations [1].

In magnetically confined fusion plasmas, anomalous particle and heat losses were observed [6, 7]. In a hot (100 million Kelvin) hydrogen plasma, this is a major obstacle on the way to achieving controlled nuclear fusion with a net energy surplus. It was found [8, 9, 10] that turbulent fluctuations give rise to elevated levels of transport perpendicular to the confining magnetic field. Consequently, turbulent transport has been investigated in a number of experiments [11, 12, 13, 14] and it is well established that it plays an important role in tokamaks [15, 16, 17, 18, 19] and stellarators [20, 21]. Although the importance of turbulent transport is well established, many questions about the underlying instabilities and the microscopic structure are still unanswered.

In hot fusion plasmas, the main experimental problem is the absence of diagnostics with a high spatial and temporal resolution in the bulk plasma. The use of Langmuir probes is confined to the edge plasma, where the plasma has direct contact with the wall via open field lines. Wall contact may drastically change the turbulent properties compared to the confinement region

of the plasma.

The torsatron TJ-K [22, 23] is an experiment whose main objective is the investigation of turbulence in magnetically confined plasmas. The device and its discharges are introduced in Chap. 3. TJ-K uses rather low temperature plasmas that are confined in the same way as fusion plasmas, but are easier to diagnose than their hot counterparts. The ability to employ Langmuir probe arrays in the whole plasma volume is a major advantage of TJ-K, because highly resolved spatio-temporal measurements of the fluctuation quantities are necessary for meaningful investigations of turbulence. TJ-K is also more flexible in its choice of working gases than conventional fusion experiments, which opens up a larger range of parameters, especially for the *drift scale* ρ_s. At the same time, the dimensionless parameters which govern turbulence are comparable to those of fusion edge plasmas [24].

An important element of the approach adopted in TJ-K for uncovering the general workings of turbulence is the comparison of experimental results with simulations [24, 25] using the DALF3 drift-Alfvén code [26, 27], introduced in Chap. 2.

Since turbulence is an apparently random motion of fluid elements with characteristic structures, statistical techniques have to be employed for characterisation. Another reason is that while the time traces of a certain turbulent quantity at two adjacent points in space may be radically different (and do indeed hold too much information), quantities like the probability distribution function (PDF) or the power spectra may be identical [1, 2, 5]. Statistical techniques relevant to this work will be explained in Chap. 2.

The scope of this work is the experimental investigation of plasma turbulence in the TJ-K experiment and comparison not only with general theoretical results on turbulent behaviour, but also with simulations that were carried out especially for TJ-K conditions. The goal is to gain a deeper understanding of turbulence as a universal phenomenon in plasmas.

Specifically, this work describes the design and execution of Langmuir probe measurements, using computer controlled movable multi-tip probes and 64-tip poloidal probe arrays. The fluctuation data was analysed using spectral techniques and conditional averaging. The wave number resolved spectra of turbulent transport, density and potential fluctuations, which are not normally available for fusion plasmas, yield results that are compared to the turbulent structures found with the conditional averaging method. In contrast to previous turbulence studies in fusion devices, turbulence data is gathered in the confinement region of the plasma. The wave number range accessible to the probe array is 1.5 orders of magnitude, which is sufficient for the investigation of the scaling properties of the spectra.

Complementing the turbulence studies, a simple energy and particle bal-

ance analysis [28] has been done, which sets upper limits on the simultaneously achievable densities and temperatures in TJ-K.

Chapter 2

Turbulence in Plasmas

In this section, the basic equations used to model turbulence in toroidal plasmas are introduced. Then the fundamental drifts in magnetised plasmas are treated, because they are essential for understanding plasma flows and the transport caused by them. In toroidal fusion plasmas, a major contribution to transport is caused by turbulence. This turbulent transport and the instabilities responsible for it are reviewed, followed by the data analysis techniques used in this work. Finally, some general properties of turbulence in neutral fluids and plasmas are presented.

2.1 Basic Equations for Plasma Turbulence

Turbulence is an emergent phenomenon that is inherent to fluids, gases and plasmas. It usually arises from the non-linearity of the governing equations. The most general equation for an N-body system is the Liouville equation, but with $6N$ independent variables, it is unwieldy for real-world systems of $\gg 10^{10}$ particles. However, we do not need all the information that is contained in Newton's equations of motion for all particles. We are usually dealing with atomic particles that are indistinguishable among their species and we are only interested in macroscopic properties (like densities). It is therefore sufficient to study the *Boltzmann distribution function*

$$f \;=\; f(x, y, z, v_x, v_y, v_z, t) \tag{2.1}$$

which only depends on six phase space variables and the time. When multiplied by the size of the phase space cell, it gives the probability to find a particle of a particular species in the region $dxdydzdv_xdv_ydv_z$ around point (x, y, z) with a velocity of (v_x, v_y, v_z, t).

The evolution of f is given by the *kinetic equation*

$$\frac{\partial}{\partial t} f(\mathbf{r},\mathbf{v}) + \mathbf{v}\nabla f(\mathbf{r},\mathbf{v}) + \mathbf{b}\nabla_v f(\mathbf{r},\mathbf{v}) = \left(\frac{\partial f(\mathbf{r},\mathbf{v})}{\partial t}\right)_{coll.} \tag{2.2}$$

where $\mathbf{r} = (x, y, z)$ and $\mathbf{v} = (v_x, v_y, v_z)$ and the t dependence has been dropped. $\mathbf{b}$ is the acceleration due to forces, e.g. for electromagnetic forces $\mathbf{b} = q(\mathbf{E} + \mathbf{v} \times \mathbf{B})/m$. ∇_v is the gradient in velocity space. The expression on the right hand side is the *Boltzmann collisional term.* While collisions between particles of the same species do not change the total momentum and energy of the species, collisions between different species do and the collisional term becomes non-zero. If the collision term is set to zero, the equation becomes the *Vlasov equation.*

2.1.1 Two Fluid Equations

But even the Vlasov equation is often too complicated to be conveniently simulated on a computer. The next step is the transition from the microscopic particle picture to the macroscopic fluid picture. Instead of a probability density, we regard the plasma as a charged fluid with continuous particle, momentum and energy density for each particle species. Formally, this is done by calculating moments of the distribution function.

$$\begin{aligned} \langle \mathbf{g}(\mathbf{r},t) \rangle &= \frac{\int d^3v\, \mathbf{g}(\mathbf{r},\mathbf{v},t) f(\mathbf{r},\mathbf{v},t)}{\int d^3v\, f(\mathbf{r},\mathbf{v},t)} \\ n(\mathbf{r},t)\, \langle \mathbf{g}(\mathbf{r},t) \rangle &= \int d^3v\, \mathbf{g}(\mathbf{r},\mathbf{v},t) f(\mathbf{r},\mathbf{v},t) \end{aligned} \tag{2.3}$$

The moment function $\mathbf{g}$ is a power of the velocity $\mathbf{v}$. The first three moments for example lead to the conservation laws for mass, momentum and energy.

$$\begin{aligned} g &= m \\ \mathbf{g} &= m\mathbf{v} \\ g &= mv^2/2 \end{aligned} \tag{2.4}$$

To make a long story short: The two-fluid equations for electrons and ions are the continuity equation and the equation of motion (momentum equation) for each particle species

$$\frac{\partial}{\partial t} n_\alpha + \nabla(n_\alpha \mathbf{u}_\alpha) = 0 \tag{2.5}$$

$$m_\alpha n_\alpha \left(\frac{\partial}{\partial t} + \mathbf{u}_\alpha \nabla\right) \mathbf{u}_\alpha = -\nabla p_\alpha + n_\alpha q_\alpha \left(\mathbf{E} + \mathbf{u}_\alpha \times \mathbf{B}\right) + q_\alpha n_\alpha (\mathbf{u}_\alpha - \mathbf{u}_\beta)/\sigma$$

where the indices α and β denote the particle species, q is the particle charge, $\mathbf{u}$ the drift velocity and σ is the conductivity of the plasma. The bracket on the left hand side of the momentum equation is called the *convective derivative*. It represents the total time derivative in the frame of the co-moving plasma volume. The pressure tensor in the momentum equation has been simplified to the gradient of the scalar pressure. The electromagnetic fields in the Lorentz force term are determined by external conditions and the self-consistent fields of the charge and current distributions. The last term on the right hand side of the momentum equation governs the momentum transfer between different particle species through collisions. It is also possible to add a viscous damping term to this side of the equation.

Another approach is to start with the fluid picture and then derive continuity and momentum balance equations by looking at a test volume and using the Stokes' and Gauss integral equations, an approach that is also used for the *Navier-Stokes equation* for neutral fluids.

In both cases, the system of equations must be closed by an additional equation, because a moment term $\propto v^1$ produces an expression $\propto v^2$, namely the energy in $p = nk_BT$. The closure is often to replace the energy equation by assuming adiabatic or isothermal processes. The entire set of *Maxwell equations* completes the system.

The fluid picture is powerful enough to describe e.g. drift waves, but anything that alters the energy distribution function from the Maxwell distribution cannot be modeled in it. This includes well-known effects like Landau damping. It is important to notice that the scales must be large and slow enough that gyro radius effects do not matter. Also the plasma in the regarded fluid elements must always be thermalised.

2.1.2 MHD Equations

The next simplification is the transition to the single fluid *MHD equations* with only one mass density ρ_m using the quasi-neutrality condition. The unified charge density becomes ρ and the joint drift velocity is $\mathbf{u}$. The net current density is given by $\mathbf{j}$.

$$\begin{aligned} \rho_m &= \rho_{me} + \rho_{mi} \approx \rho_{mi} \\ \mathbf{u} &= (\rho_{me}\mathbf{u}_e + \rho_{mi}\mathbf{u}_i)/\rho_m \\ \mathbf{j} &= \rho_e\mathbf{u}_e + \rho_i\mathbf{u}_i \approx \rho_e(\mathbf{u}_e - \mathbf{u}_i) \\ \rho &= \rho_e + \rho_i \end{aligned} \tag{2.6}$$

The continuity and momentum equations then become

$$\begin{aligned} \frac{d\rho_m}{dt} + \rho_m(\nabla \mathbf{u}) &= 0 \\ \rho_m \frac{\partial \mathbf{u}}{\partial t} &= \rho \mathbf{E} + \mathbf{j} \times \mathbf{B} - \nabla p \\ \nabla \mathbf{j} &= 0 \\ \mathbf{j} &= \sigma(\mathbf{E} + \mathbf{u} \times \mathbf{B}) \end{aligned} \tag{2.7}$$

with the third equation expressing the quasi-neutrality condition. The last equation is Ohm's law for the current $\mathbf{j}$ with conductivity σ.

Together, these equations are able to describe such phenomena as the global plasma behaviour of toroidal devices and instabilities like the *interchange instability*. A simple relation that holds for the equilibrium is

$$\mathbf{j} \times \mathbf{B} = \nabla p \tag{2.8}$$

2.1.3 Particle Drifts in Magnetised Plasmas

In the presence of a background magnetic field, charged particles cannot move freely in the plasma. The turbulence dynamics perpendicular to the magnetic field are therefore determined by the particle drifts that are caused by the interaction with the gyro motion.

The *Lorentz force* makes all charged particles gyrate around the magnetic field lines with the cyclotron frequency $\omega_{c\alpha}$ and the mean gyro or Larmor radius ρ_α

$$\begin{aligned} \omega_{c\alpha} &= qB/m_\alpha \\ \rho_\alpha &= \sqrt{2m_\alpha k_B T_\alpha}/|q|B \end{aligned} \tag{2.9}$$

where α stands for ions or electrons, m is the mass, q the charge, B the magnetic field and T the temperature. Along the magnetic field, the motion happens as if there was no field. Perpendicular to the field, however, a force acting on the particle does *not* lead to an acceleration of that particle in the direction of the force, at least not at time scales larger than a gyration period. Because of the periodic deformation of the drift orbit, the particle will actually drift into a direction perpendicular to the field and perpendicular to the force, with an unaccelerated velocity that is proportional to the force $\mathbf{F}$:

$$\mathbf{u}_D = \frac{\mathbf{F} \times \mathbf{B}}{qB^2} \tag{2.10}$$

There are several possibilities for the force term. The most important is the $E \times B$ *drift* with $\mathbf{F} = q\mathbf{E}$. Since the charge cancels out, this is an

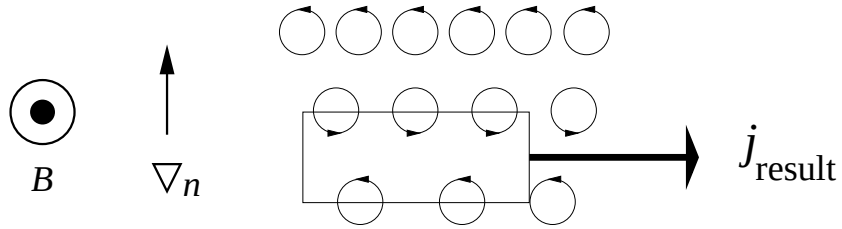

Figure 2.1: Illustration of the diamagnetic drift. The current represented by the gyro motion of the particles on the high-density side is only partially compensated by the particles on the low-density side.

ambipolar drift that does not cause a charge separation, so it can cause large-scale convection of the plasma. In contrast, the other drifts are in the opposite directions for electrons and ions: the *curvature drift* arises from the centrifugal force on particles following magnetic field lines with a curvature radius $\mathbf{R_c}$.

$$\mathbf{u}_c = \frac{2W_\parallel}{R_c^2}\frac{\mathbf{R_c}\times\mathbf{B}}{qB^2} \tag{2.11}$$

The *gradient drift* has $\mathbf{F} = W_\perp \nabla_\perp B/B$ ($W_\perp$ is the kinetic particle energy perpendicular to B). The *diamagnetic drift* is proportional to the pressure gradient and the *polarisation drift* is caused by a temporally varying electric field.

The diamagnetic drift only shows in the fluid description. In a homogeneous plasma the currents represented by the gyrating particles all cancel out. If the plasma has a density gradient, then the currents do not cancel (Fig. 2.1). On an equi-density line, the total currents of all particles on the high-density side are higher than the total currents on the low-density side, which go into the opposite direction. A net current remains although the gyro centers of the particles themselves stay stationary. The drift velocity is

$$\mathbf{u}_{dia} = -\frac{\nabla\mathbf{p}\times\mathbf{B}}{qnB^2} \tag{2.12}$$

where n is the density, p the plasma pressure and q the charge of the regarded particle species.

2.1.4 Hasegawa-Mima and Hasegawa-Wakatani Equations

Until now, the equations (MHD, two fluid) were still general in the sense that no assumptions about the background magnetic field or time and space scales

were made. In order to describe the magnetised plasmas of fusion reactors, further simplifications have to be made without losing the features essential for turbulence. Electromagnetic waves e.g. are optional, but the non-linear convective derivative should be kept.

In the following, the background magnetic field B will always be in the $\hat{z}$ direction. This introduces an anisotropy into the plasma: The dynamics perpendicular to B are dominated by the gyration of the particles and hence by the drifts, while the dynamics along the magnetic fields lines are governed by resistivity effects. In the limit of an adiabatic electron response parallel to B, the problem becomes basically two-dimensional ($k_\parallel \approx 0$). Spatial derivatives will usually be decomposed into their perpendicular $\nabla_\perp$ and parallel $\nabla_\parallel$ parts. Also a distinction between background quantities (e.g. n_0) and fluctuating quantities (n) is necessary.

With the simplification that density and potential follow the Boltzmann relation with electrostatic potential Φ

$$n_e = n_0 \exp\left(\frac{e\Phi}{T_e}\right) \tag{2.13}$$

it is possible to eliminate the density field, yielding the single-field *Hasegawa-Mima equation* [29], presented here in the form given in [30]

$$\frac{d}{dt}\left(\nabla_\perp^2 - 1\right)\phi - (\nabla\phi \times \hat{\mathbf{z}}) \cdot \nabla\left(\nabla_\perp^2 - 1\right)\phi + \frac{\nabla n_0}{n_0} \times \nabla\phi \cdot \hat{\mathbf{z}} = 0 \tag{2.14}$$

with the normalised quantities potential ϕ and background density n_0. $\hat{\mathbf{z}}$ is the unity vector in the z direction. The HM equation basically describes (linearly stable) *drift waves*, which are treated in more detail in Sec. 2.3.3.

A set of equations that retains the density independently from the potential is the *Hasegawa-Wakatani* set of equations [31], which permits the density and potential perturbations to develop a phase difference, allowing the treatment of unstable drift waves.

2.1.5 DALF3

DALF3 is a three dimensional two fluid code that incorporates MHD, drift wave and Alfvén wave dynamics in a toroidally confined plasma [26, 27]. A general review of simulation techniques is given in [32]. DALF3 is used as a complement to experimental investigations in TJ-K [24, 25]. The code simulates a flux tube around a magnetic field line, which in turn winds helically around the torus. The magnetic field strength along this orbit is not

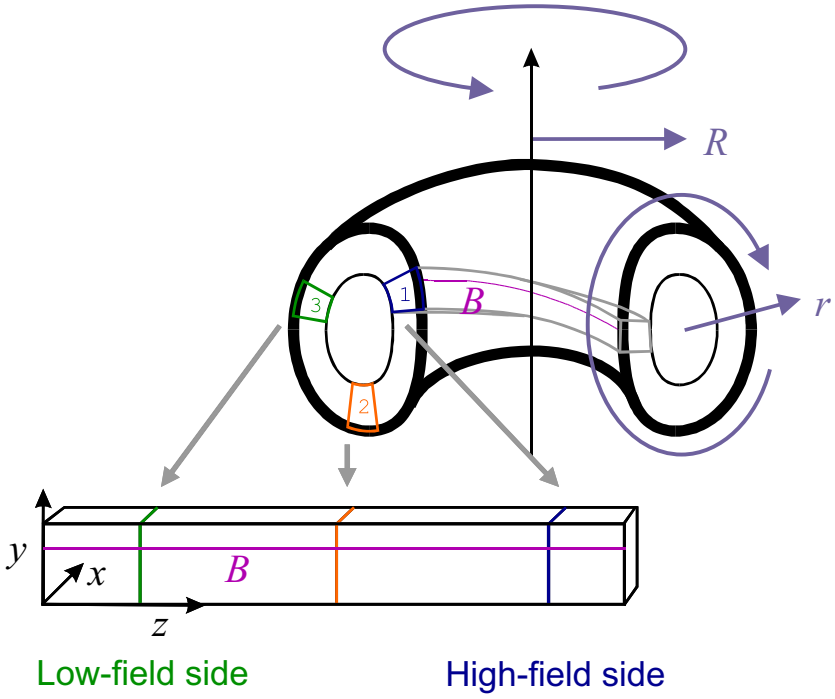

Figure 2.2: Torus and DALF flux tube geometry. Φ, θ and r are the toroidal, poloidal and radial torus coordinates, respectively. The flux tube coordinates x and y are in the direction parallel and perpendicular to the density gradient. The z coordinate is along the magnetic field line. The flux tube makes three toroidal revolutions, traversing both the high- and low-field regions.

constant, but changes as $|B| \propto 1/R$ with R along the major radius. The toroidal coordinates and the flux tube geometry are illustrated in Fig. 2.2. Since TJ-K has a rotational transform of about 1/3, the flux tube makes three toroidal revolutions and closes in itself. The magnetic field geometry used is that of a tokamak equivalent to TJ-K. While a tokamak is axisymmetric in the toroidal direction, a stellarator has to be treated in all three dimensions. The effect of the stellarator geometry has been studied elsewhere [33].

The relevant non-linear equations in normalised units are charge conservation, parallel electron momentum conservation and one Maxwell equation,

respectively:

$$\begin{aligned} \left(\frac{\partial}{\partial t} + v_e \cdot \nabla\right) \nabla_\perp^2 \phi &= \nabla_\parallel J_\parallel \\ \beta_e \frac{\partial}{\partial t} A_\parallel + \mu_e \left(\frac{\partial}{\partial t} + v_e \cdot \nabla\right) J_\parallel &= \nabla_\parallel (p_e - \phi) - \mu_e \nu_e J_\parallel \\ J_\parallel &= -\nabla_\perp^2 A_\parallel \end{aligned} \tag{2.15}$$

Additionally, an energy equation is solved. The system is similar to the Hasegawa-Wakatani equations. The code uses the flow velocity v_e, the pressure p_e, the potential ϕ, the parallel current $J_\parallel$ and the parallel component of the electromagnetic vector potential $A_\parallel$. The coupling between parallel and perpendicular dynamics happens via the parallel gradient of the parallel current.

The normalised parameters are the normalised plasma beta β_e, which drives the interchange instability, the mass ratio μ_e, which determines the ratio of the time scales of parallel to perpendicular dynamics, and finally the normalised collisionality ν_e which governs the parallel resistivity, which is responsible for the drift wave instability. The spatial scale is given by the drift scale ρ_s.

$$\begin{aligned} \nu_e &= \frac{\nu_{ee} L_\perp}{c_s} \\ \beta_e &= \frac{\beta}{2} \left(\frac{R}{\imath L_\perp}\right)^2 \\ \mu_e &= \frac{m_e}{m_i} \left(\frac{R}{\imath L_\perp}\right)^2 \\ \rho_s &= \frac{c_s}{\omega_{ci}} = \frac{\sqrt{m_i T_e}}{eB} \end{aligned} \tag{2.16}$$

where ν_{ee} is the electron-electron collision frequency, normalised to the the density gradient length $L_\perp$ and the sound speed c_s. The rotational transform $\imath$ determines the parallel connection length $L_\parallel = R/\imath$. ω_{ci} is the ion cyclotron frequency.

2.2 Transport in Toroidal Plasmas

In fusion experiments, "transport" always means transport in the radial direction, perpendicular to the magnetic field lines. One usually differentiates between *classical*, *neoclassical* and *anomalous* or *turbulent transport*. General reviews of anomalous transport measurements and theory are given in [11, 12].

Classical theory sees transport as a random walk process with a step size of the gyro radius and a step frequency given by the frequency of 90° collisions. An undisturbed particle can gyrate around its field line indefinitely. In a 90° collision, the direction of the particle's motion changes, leading to a displacement of the center of the gyration motion by approximately one gyro radius. The collision has to be with a different particle species because there is no net momentum transfer within a species. Since toroidal plasmas have a density gradient, this random walk gives rise to a diffusive type of transport into regions of lesser density. The magnitude of classical transport is several orders too small to account for the observed level of transport.

In neoclassical theory, the influence of the toroidal geometry on the particle orbits are investigated. Due to the drifts, the particles are not perfectly bound to their magnetic field line. Because of the helical winding of the magnetic field lines, they traverse regions of high magnetic field strength on the inside of the torus, as well as regions of weaker magnetic field strength on the outside of the torus. This is a magnetic mirror configuration, where particles with too little parallel kinetic energy cannot enter the regions of high magnetic field and are reflected. On account of the curvature drift, the particle orbits deviate from the magnetic field line. The projection of this bouncing orbit on the poloidal plane gives a banana shape, so the orbits are called banana orbits. The width of the banana orbits is much larger than their gyro radius. Consequently, their random walk diffusion coefficient is typically a factor of ten larger than the classical one. Another neoclassical mechanism of particle loss are so-called direct loss orbits, commonly found in simple stellarator designs. Here, the particles leave the plasma *unless* they make a collision and are removed from their current orbit.

Since none of the above mechanisms can account for the observed transport [6, 7, 8], the term *anomalous transport* has been coined to describe the remaining high-yield loss mechanisms for particles and heat. It is generally accepted that plasma turbulence is the responsible cause for anomalous transport [9, 10] Two such turbulent mechanisms will be treated here.

In high β plasmas, where plasma pressure is close to the stability limit, it is conceivable that the magnetic field lines are distorted in such a manner that temporarily, they point radially outwards. This allows particles to ex-

perience a radial displacement while moving along a field line, which is only restricted by ohmic resistance. Although ambipolar fields inhibit massive particle transport, there is still a substantial heat transport in this scenario, which is called electromagnetic turbulence.

The electrostatic anomalous transport is caused by drifts due to the fluctuating electric field. The poloidal component of these perturbations causes a radial flow via the $E \times B$ drift. If the relation between flow perturbations and density perturbations is such that a density increase always occurs when the flow is directed outward, a net outward transport happens even though the density and flow perturbations each have a zero mean. For this kind of transport, the magnetic dynamics can be neglected. In the following, we will regard only electrostatic turbulence which is believed to be the dominant effect. See Secs. 2.3.2 and 2.3.3 for examples of instabilities that can cause this kind of transport. Turbulent transport has the potential to account for the observed high transport levels in fusion plasmas [12].

The electrostatic turbulent transport for frequencies below the ion cyclotron frequency is given by the average of the fluctuating radial flow velocity $\widetilde{E}_\theta/B$ times the density or pressure fluctuations:

$$\begin{aligned} \text{Particle transport} \quad \Gamma_\alpha &= \langle \widetilde{E}_\theta \widetilde{n}_\alpha \rangle / B \\ \text{Energy transport} \quad Q_\alpha &= \frac{3}{2} n_\alpha \langle \widetilde{E}_\theta k_B \widetilde{T}_\alpha \rangle / B + \frac{3}{2} k_B T_\alpha \langle \widetilde{E}_\theta \widetilde{n}_\alpha \rangle / B \end{aligned} \tag{2.17}$$

The average is over time when the measured quantities are time dependent and over space when they are space dependent. Fluctuating quantities are denoted with $\widetilde{}$, $\widetilde{E}_\theta$ is the poloidal electric field strength, B is the toroidal magnetic field, n and T are density and temperature and α enumerates the particle species. Quasi-neutrality and the ambipolar nature of the $E \times B$ drift mandate that particle transport for electrons and ions should be the same and the index α can be dropped in the particle transport equation. In the following, only the electrostatic particle transport will be investigated.

It is advisable to calculate the turbulent transport in the frequency or wave number domain as well as the time or space domain. The reason is that a Fourier transform of a transport time series will give the transport fluctuation level at each scale. By the very nature of Fourier modes, the modes are mean free, and all the net transport is lumped together into the zero mode. Furthermore, the transport fluctuations are independent of the cross phase between density and potential, which are vital for the determination of the mean transport.

If one takes the Fourier representation of $\widetilde{E}_\theta(x)$ and $\widetilde{n}(x)$, the transport

can be expressed as

$$\begin{aligned} \Gamma(x) &= \widetilde{E}_\theta(x)\widetilde{n}(x)/B \\ &= \sum_j \sum_l E_{\theta j} \exp(ik_j x) n_k^* \exp(-ik_l x)/B \end{aligned} \tag{2.18}$$

where $E_{\theta j}$ and n_j are the complex Fourier coefficients of $\widetilde{E}_\theta$ and $\widetilde{n}$ and k_j is the wave number. The sums go from $-\infty$ to $+\infty$. If x is the poloidal direction, then we have to average over x to compute the total transport

$$\langle \Gamma \rangle_x = \sum_j \sum_l E_{\theta j} n_k^* \langle \exp(ik_j x) \exp(-ik_l x) \rangle_x /B \tag{2.19}$$

The averages vanish for products of unequal modes ($j \neq l$):

$$\langle \exp(ik_j x) \exp(-ik_l x) \rangle_x = \delta_{jl} \tag{2.20}$$

The mean transport at a given mode k_j is then given by the fluctuation level of electric field and density and by the cross phase γ_k at that mode

$$\begin{aligned} \Gamma(k) &= |E_{\theta k} n_k^*|/B \\ &= |E_{\theta k}||n_k| \cos(\gamma_k^{En})/B \\ \gamma_k^{En} &= \arg(E_{\theta k} n_k^*) \end{aligned} \tag{2.21}$$

The same calculations can be done in the time domain. While there will usually be some correlation between the mean transport level and the transport fluctuations, the mean transport is a signed value as opposed to the transport power spectrum.

Also it has to be observed that transport fluctuations at a certain wave number mostly stem from fluctuations of density and fields at half that wave number, because the product of two sines is two minus the cosine at double the frequency. This means that the mean transport $\Gamma(k)$ at wave number k oscillates around that mean value with $2k$. In the following, a clear distinction will always be made between transport fluctuation levels and mean transport. If the cross phase between density and potential is regarded, the cross phase term in Eq. (2.21) has to be replaced by $\sin(\gamma_k^{\Phi n})$

2.3 Instabilities

The transition from the quiescent to the turbulent state is caused by *linear instabilities*. If a mode is found to be linearly unstable, its amplitude grows without bounds, until the assumptions that were made for the linear analysis in the first place are no longer valid.

The most popular instabilities found in fluids and plasmas are the *Rayleigh-Taylor instability*, the *(MHD) interchange instability* [34] and the *drift wave instability* [35, 36]. Other instabilities which are also present in fusion devices, like the tearing instability or temperature gradient driven modes are not treated here. An overview of instabilities present in fusion plasmas can be found in [32]. Common to all instabilities is a source of free energy (gravitational field, pressure gradient). If a random perturbation taps the free energy in such a way that the perturbation is amplified, the mode becomes unstable. A generic example is that of a steep sand hill, which seeks to flatten its flanks because its total potential energy is less when more sand is nearer to ground level. The gradient-flattening process is opposed by the friction between the sand grains, which leads to an equilibrium somewhere between an infinitely high and an infinitely flat pile.

The fluctuations caused by the instability can then give rise to transport as discussed in the previous section. In fully developed turbulence, the linear instability is supplanted by the non-linear instability, which has different growth rates for its modes. However, simple signatures like the cross phase between density and potential fluctuations can still be valid for transport studies, since they determine the transport level regardless of the mechanism that created them. As we will see now, it is therefore important to analyse the cross phases.

2.3.1 Rayleigh-Taylor Instability

This instability is also present in neutral fluids. A dense fluid is stacked on top of a less dense fluid in a gravitational field along the z axis. A small perturbation occurs at the interface, located at $z = 0$, between the two fluids, leading to the situation illustrated in Fig. 2.3. A half-wave b of dense material is now in the region of the light fluid and a half-wave a of less dense fluid is in the region $z > 0$. Because of incompressibility, regions a and b are of the same size. Since half-wave b is more dense than a, the center of mass of the whole system has shifted downwards, towards less potential energy. This trend increases, because the fluid in the perturbation now also has more kinetic energy, enabling it to grow further. In a later stage, a sheared flow between upward and downward motion develops, which becomes Kelvin-Helmholtz

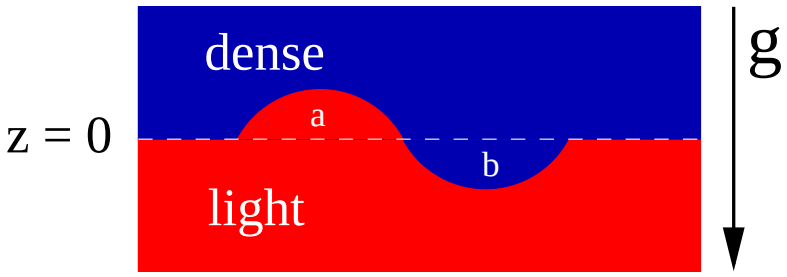

Figure 2.3: Rayleigh-Taylor instability: A dense fluid above a less dense fluid lowers its total potential energy with a perturbation (regions a *and* b*).*

unstable. This is where the non-linearities come into play.

2.3.2 Interchange Instability

The interchange instability is an MHD phenomenon similar to the Rayleigh-Taylor instability. In plasmas with a curved magnetic field in combination with a pressure gradient, particle drifts can arise which amplify random pressure perturbations and make them (linearly) unstable [34]. In contrast to the drift wave instability, this is a two dimensional process that is homogeneous along the magnetic field ($k_\parallel = 0$).

Figure 2.4 shows the two cases we need to observe: in the volume element on the left (a) the curvature radius R_c and the pressure gradient are parallel to each other, as is the case on the high-field side of a toroidal plasma. The volume element on the right (b) has them anti-parallel, a situation one would find on the low-field side of a toroidal plasma. In both cases, the magnetic field B is directed into the plane. Without any perturbation, the vertical curvature drift (Eq. 2.11) only convects plasma along lines of equal pressure. When a perturbation is present as shown in Fig. 2.4, ions that drift from the high pressure region into a low pressure region cause a surplus of positive charge at the interface, because the counterflowing electrons come from the low pressure region and cannot fully neutralise the positive charge. The opposite charge appears where electrons flow from the high to the low pressure region. The only difference between the situation on the left and on the right is the location of the positive and negative charges. If one regards periodic pressure and potential perturbations, the spatial phase between pressure and potential are $\pi/2$ in one case and $-\pi/2$ in the other case. This has the consequence that the electric field caused by the potential perturbation is oriented differently in both cases. In the “good curvature”

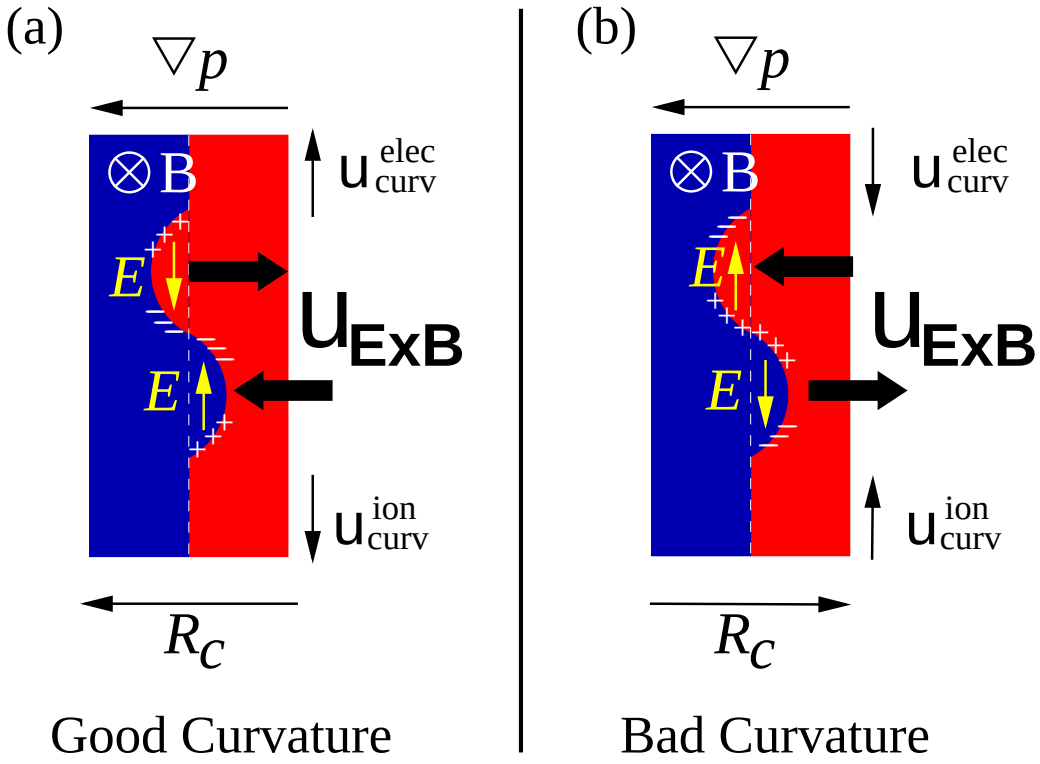

Figure 2.4: The interchange instability. A random perturbation occurs which breaks the homogeneity of the density along the direction of the curvature drift. The following charge separation gives rise to an $E \times B$ drift. This can either be stabilising (a) or destabilising (b), depending on the orientation of the magnetic curvature with respect to the pressure or density gradient. R_c is the curvature radius of the magnetic field.

case (a), the resulting $E \times B$ drift works against the initial perturbation, pushing the plasma back where it came from. In the "bad curvature" case, the drift goes into the opposite direction and increases the initial pressure perturbation. This mode becomes unstable.

In a toroidal fusion experiment with its magnetic field strength inversely proportional to the major radius, regions of good curvature are always on the inside (high-field side), while bad curvature is located on the outboard (low-field) side. Since the magnetic field lines helically wind around the torus, they connect regions of good and bad curvature, which has a stabilising effect.

The important signatures of this instability are the dependence on good/bad curvature and the phase difference of $\pi/2$ between pressure (density) and potential. The former can lead to *ballooning,* i. e. an asymmetry in

fluctuation amplitudes between the high and the low field side of the torus.

2.3.3 Drift Wave Instability

Drift waves can occur in many magnetised laboratory plasmas [35]. When they become unstable, they cause particle transport [36, 37]. The two fluid equations are necessary to describe them. The basic drift wave mechanism is illustrated in Fig. 2.5. The density or pressure gradient ∇n is perpendicular to the homogeneous magnetic field $B \| z$. A density perturbation with a finite wavelength $L_\| < \infty$ leads to instantaneous parallel movement of the adiabatic electrons to a region where the density perturbation is in the opposite direction. Due to the perpendicular structure, the ensuing $E \times B$ drift increases the perturbation on one side and decreases it on the other. This makes the density perturbation propagate in the direction of the diamagnetic electron drift, perpendicular both to ∇n and B. Since the density perturbation is not homogeneous along B, there is also a small but finite k_z, making the whole drift wave a three dimensional phenomenon.

The parallel dynamic is important for drift waves and decides if it is stable or unstable. If, due to resistivity, the electrons do not follow the density perturbations instantaneously, a phase difference between density and potential perturbations is introduced, making the drift wave unstable. In Fig. 2.5, the arrows indicating the $E \times B$ velocity are then shifted e.g. upwards. The section boxed in green is where the $E \times B$ flow then serves to increase the already present density perturbation.

The characteristic velocity is the diamagnetic velocity from Eq. 2.12, the characteristic scale is the *drift scale*

$$\rho_s \;=\; c_s/\omega_{ce} \tag{2.22}$$

where c_s is the ion sound speed and ω_{ce} is the electron gyro frequency.

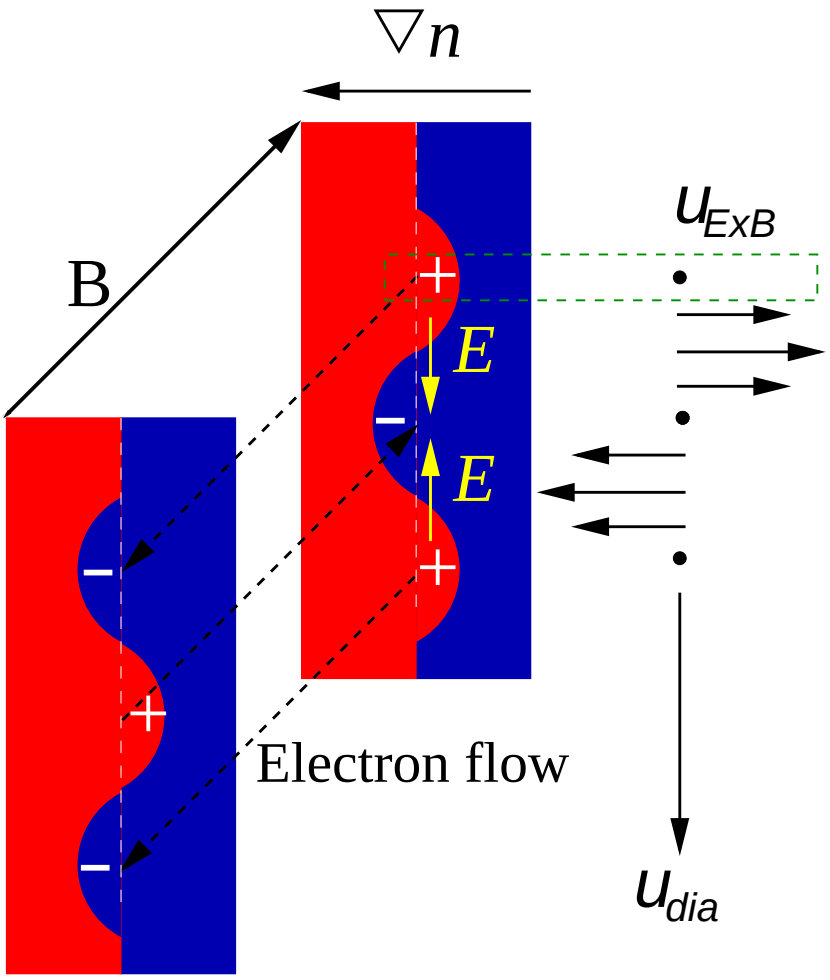

Figure 2.5: Illustration of a drift wave with adiabatic electron response in the parallel direction. Electrons escape from the positive density perturbation along the magnetic field. The ensuing potential perturbation is in phase with the density perturbation. The $E \times B$ drift leads to a propagation in the electron diamagnetic drift direction, but $k_{\parallel}$ is finite. The drift wave is stable, since the density perturbation is not amplified (green box).

2.4 Suppression of Turbulent Transport

Suppression of turbulence can happen in a number of ways. Apart from stabilising the underlying instability itself, it is possible to break apart the transport structures by sheared flows [38]. The former can for example be achieved by optimised designs that move areas with bad curvature into regions where the magnetic field has a strong poloidal and a small toroidal component [39]. In a toroidal fusion plasma, shearing apart the transport structures means that poloidal flows must be generated. These flows would then cause the shearing of the turbulent eddies, thus reducing their radial correlation length, which in turn reduces their capability for radial transport. Another mechanism is the phase decorrelation between density and potential fluctuations, resulting in a reduction of transport. This can be achieved by biasing [40].

In fusion devices, the spontaneous formation of internal transport barriers in the core (ITB) and edge regions of the plasma (H-mode) is attributed to the turbulence suppression by sheared flows [41, 42, 43, 44]. Examples of sheared flows are zonal flows (with poloidal mode number $m = 0$) or geodesic acoustic modes ($m = 1$). One possible drive of sheared flows is the turbulent viscosity or Reynold's stress, which is a mechanism for transferring radial momentum into poloidal momentum [45].

In this work, the emphasis is on diagnosing the generic turbulence inherent in confined plasmas using the new experiment TJ-K. Special transport barrier physics and sheared flows will be addressed in later investigations.

2.5 Data Analysis Techniques

For the analysis of turbulence data, statistical methods have to be used. The data processing techniques shown in this chapter can be used on data from a variety of diagnostics. For the purposes of this work, they are only used on Langmuir probe and simulation data. Most of the techniques used here are described in [1] and other textbooks.

2.5.1 Probability Distribution Functions

The *probability distribution function* (PDF) $P_X(x)dx$ gives the probability that a stochastic variable X will assume a value between x and $x + dx$ [1]. The moments of the PDF are formed by integrating over the PDF multiplied by a power of x. The first four moments are the *mean value* $\bar{x}$, the *standard deviation* σ, the *skewness* S and the *kurtosis* K. The skewness is a measure of how asymmetric the PDF is, and the kurtosis measures how much flatter a PDF is compared to a Gaussian, which has $S = 0$ and $K = 0$.

$$\begin{aligned} \bar{x} &= \int_{-\infty}^{\infty} P_X(x) x dx \\ \sigma &= \sqrt{\int_{-\infty}^{\infty} P_X(x)(x-\bar{x})^2 dx} \\ S &= \int_{-\infty}^{\infty} P_X(x)(x-\bar{x})^3 dx/\sigma^3 \\ K &= \int_{-\infty}^{\infty} P_X(x)(x-\bar{x})^4 dx/\sigma^4 - 3 \end{aligned} \tag{2.23}$$

The Gaussian PDF with mean $\bar{x}$ and standard deviation σ is given by

$$P_G(x) = \frac{1}{\sqrt{2\pi}\sigma} \cdot \exp\left\{-(x-\bar{x})^2/2\sigma^2\right\} \tag{2.24}$$

In turbulence, many quantities exhibit a Gaussian or near-Gaussian PDF. It is also very common to have a dominant mode on top of the turbulence. This is sometimes the case in ECRH discharges in TJ-K (Sec. 3.4.1). A time series of a sinusoidal signal spends most of its time at the extreme values, so there are two peaks on the positive and the negative flank of the PDF. It is therefore a worthwhile experience to look at the different spatial or temporal scales of a signal and to get a PDF for each scale separately. An efficient way of doing this uses wavelet analysis.

2.5.2 Scale Separation and Structure Functions

For the scale separation it is customary to compute the spatial or temporal *increments* of a quantity X [1]

$$\begin{aligned} \delta X(\mathbf{l}) &= X(\mathbf{r}+\mathbf{l},t) - X(\mathbf{r},t) \\ \delta X(\tau) &= X(t+\tau) - X(t) \end{aligned} \tag{2.25}$$

Computing the increments gives a new timeseries for each scale τ or $|\mathbf{l}|$ for which e.g. the PDFs are computed. A turbulent Gaussian process will usually display a dependence of the PDF on the scale τ or $|\mathbf{l}|$. For large increments, the PDF will tend to the original PDF because the distant fluctuations are essentially independent of each other. At small scales, an *intermittent* behaviour can become apparent, where the PDF develops broad tails. This is treated in more detail in Sec. 2.6.

If the bulk flow velocity u is much larger than the turbulent flows, then the *Taylor hypothesis* holds and one can replace the spatial increment by a temporal one. Then the second form of Eq. 2.25 is used and $\tau = l/u$. This makes it possible to rely on single point measurements instead of the much more complex, spatially resolved measurements with many probes. It is not certain if the Taylor hypothesis is always valid for TJ-K plasmas.

A different way of looking at the data is the *structure function* approach [1]. The structure function of order p is defined as

$$S_p(l) = \langle (\delta X(l))^p \rangle \tag{2.26}$$

where for X the flow velocity is used and $\delta X(l)$ is its increment as defined above. The angle brackets denote the taking of the average. The increments can be restricted to e.g. increments parallel to the flow velocity (longitudinal structure function). Structure functions are attractive because of the possibility to derive universal scaling laws for them [1, 2, 3, 4] (see Sec. 2.6). The difficulty of measuring the structure function increases with p, with $p > 5$ becoming almost impossible to assess [46].

2.5.3 Spectral Analysis and Correlation Functions

In its simplest form, spectral analysis means just taking the Fourier transform (FT) $\hat{X}$ in time and/or space of the data signal X

$$\begin{aligned} \hat{X}(\omega) &= \frac{1}{\sqrt{2\pi}} \int_{-\infty}^{\infty} X(t) \exp(-i\omega t) dt \\ X(t) &= \frac{1}{\sqrt{2\pi}} \int_{-\infty}^{\infty} \hat{X}(\omega) \exp(i\omega t) d\omega \end{aligned} \tag{2.27}$$

The Fast Fourier Transform (FFT) is an efficient algorithm for computing the FT of a discretely sampled signal [47].

It is also possible to calculate higher-order spectra (bi-spectra), which reveal information about the presence of three-wave interactions [48].

The correlation function gives information on how the values of a physical quantity at different points in space or time relate to each other. The normalised cross correlation $C_{XY}(\tau)$ between two time series $X(t)$ and $Y(t)$ is given by

$$\begin{aligned} C'_{XY}(\tau) &= \int_{-\infty}^{\infty} X(t)Y(t+\tau)dt \\ C_{XY} &= \frac{C'_{XY}}{\sqrt{C'_{XX}(0)C'_{YY}(0)}} \end{aligned} \tag{2.28}$$

The correlation function is a measure of how similar two signals are. A turbulent structure that passes location r at one time t and location r' at a later time $t+\Delta t$ would cause the cross correlation $C_{XX'}$ of the signals $X(r,t)$ and $X'(r',t)$ to have a peak at $\tau = \Delta t$. The auto correlation function always has a peak at $\tau = 0$. Its width is a measure of how long coherent events are. This also applies to the spatial domain.

It is important to keep in mind that homogeneity in time or space is assumed here. If this is not the case, the correlation function becomes a function not of the displacement, but of two points in time or space [20].

Finally, the efficient computation of the correlation function is given by the Wiener-Khintchine theorem [49], which allows the use of the FFT algorithm

$$C'_{XY}(\tau) = \int_{-\infty}^{\infty} \hat{X}(\omega)\hat{Y}^*(\omega)\exp(i\omega t)d\omega \tag{2.29}$$

2.5.4 Conditional Averaging

Conditional averaging or conditional sampling is method that uses a reference signal to pick sub-timeseries out of the main data signal each time when the reference signal meets a certain condition [50, 51]. It is assumed that the data signal consists of some stationary background, an incoherent noise part and a coherent, not necessarily periodic part.

In the experimental setup, a reference signal X_0 is taken at a fixed position $\mathbf{r}_0$ in the plasma. In order to detect coherent events, a condition is imposed on the reference signal. This can be of the form that a certain value, e.g. two times the standard deviation is reached. The N points t_i in time that are selected by the condition are then used to pick sub-timeseries $[t_i - \tau/2, t_i +$

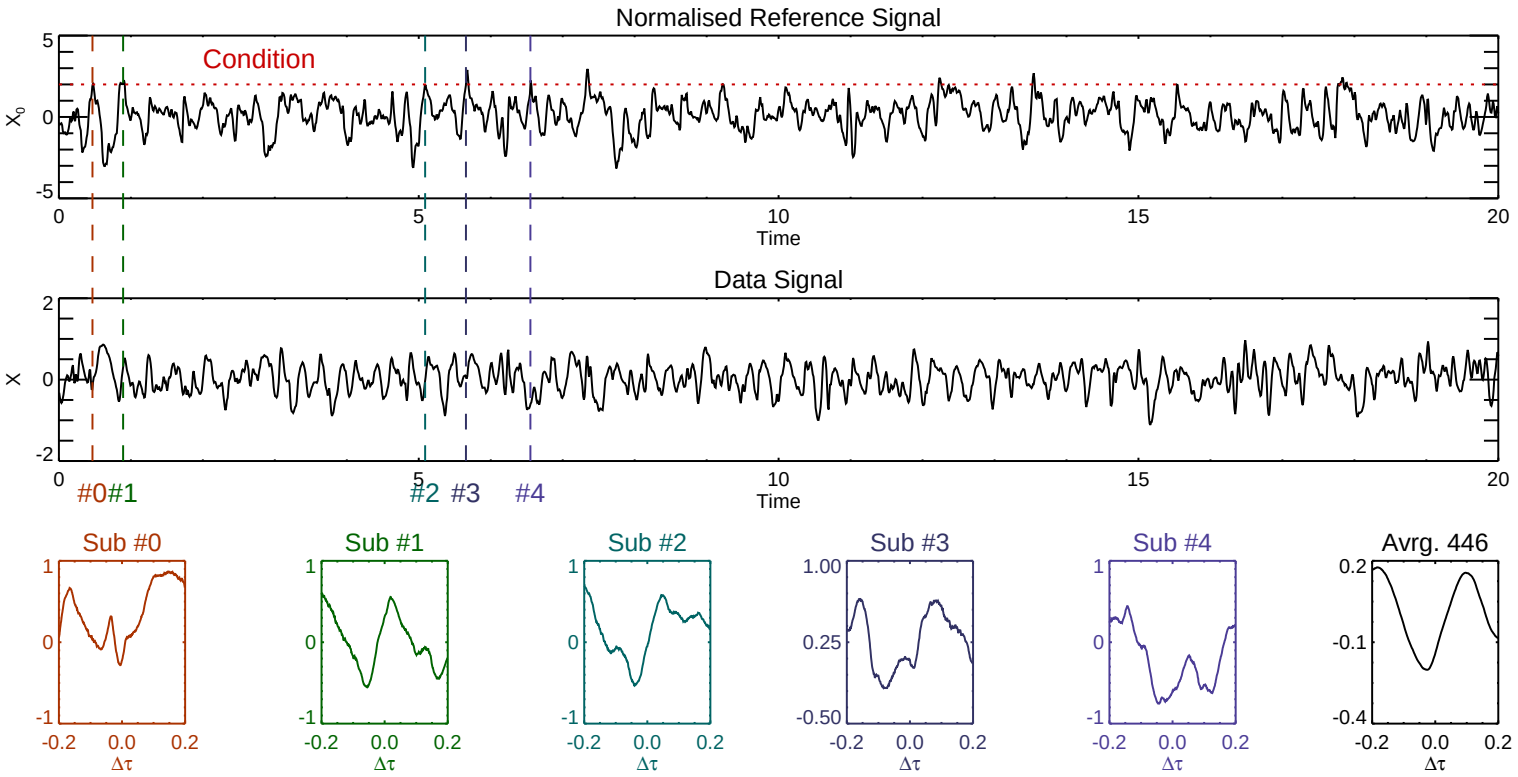

Figure 2.6: Illustration of the conditional sampling technique. Where the reference signal (top) meets the condition $X_0 = 2$ on a rising flank, a sub-timeseries is picked from the data signal (middle). The first five sub-series are plotted at the bottom. The last plot shows the average of all 446 sub timeseries. Only 2% of the data and reference signal from discharge #1896 are shown.

$\tau/2]$ of length τ from the second probe, called the data signal $X(\mathbf{r}, t)$ here, which is simultaneously acquired at a different spatial position $\mathbf{r} = \mathbf{r}_0 + \Delta\mathbf{r}$. If the coherent event propagates past the second probe, it is contained in the sub-timeseries, which should be as long as a correlation time. The ensemble average over all time series extracts the coherent part from the incoherent background noise, as illustrated in Fig. 2.6 with data from TJ-K. The procedure is repeated for different positions of the data probe. From these measurements, a spatio-temporal picture X_{CA} of the coherent events can be assembled.

$$\begin{aligned} X_{CA}(\mathbf{r}, t) &= \frac{1}{N} \sum_{i=1}^{N} X(\mathbf{r}, t_i + t) \\ t &\in [-\tau/2, \tau/2] \end{aligned} \tag{2.30}$$

The linchpin of the entire technique is the proper formulation of the condition, which has to be done *before* anything is known of the results. In addition to specifying the value of X_0 in terms of the standard deviation σ, lower and upper bounds for X_0 in the time window τ can be given, or a condition on the derivative (rising or falling flank, local extremum). The latter is especially useful for helping ensure that a coherent structure is always detected at the same phase with respect to the time window. However, a certain amount of jitter cannot be avoided, which leads to a smearing out of the averaged structure. In the results presented here, a condition of $+2\sigma$ or -2σ and a positive derivative was used.

A pathological case would be the presence of two totally differently shaped coherent events that both satisfy the condition. If they occur with a similar frequency, the averaged result will be a combination of the two shapes, which can be misleading [52]. If the life times of these two events are different, it is possible to separate them in the analysis.

A further shortcoming is that in turbulence, small structures usually also have small fluctuation amplitudes, so they tend to be buried by the large structures. Band-pass filters have (non-systematically) been applied to the data prior to conditional averaging in order to attempt a scale separation.

2.6 General Properties of Turbulence

In this section, some universal properties of turbulent flows will briefly be presented. A system is regarded as turbulent, when it displays fluctuations in the relevant physical quantities at all spatial and temporal scales. For fluid dynamics, this means that the *Reynolds number*

$$R = \frac{LV}{\nu} \tag{2.31}$$

is large, where L and V are the characteristic scale length and flow velocity and ν is the kinematic viscosity.

For neutral fluids, investigations usually concentrate on the flow velocity, since the flows are taken to be incompressible and of uniform density. In plasma turbulence, the general case would involve density, temperature, electric and magnetic field fluctuations. In this work, the focus will be on electrostatic turbulence, where density and potential fluctuations alone are important and additionally, temperature fluctuations are neglected. With the static background magnetic field, the turbulent flows are determined by the electric fields via the $E \times B$ drift.

Turbulence displays an infinite number of degrees of freedom, so that a particular time evolution is usually not repeated. This necessitates a statistical treatment of turbulence. The simplest quantity in this regard is the *probability distribution function* (PDF) and its moments, defined in Sec. 2.5.1

Basic fluctuating quantities normally have a Gaussian or near-Gaussian PDF, as shown in Fig. 2.7. The deviation of potential, density and electric field from a Gaussian is different for different discharges. The *turbulent transport* fluctuations (see Sec. 2.2) however always show a distinct non-Gaussian shape. It has a more peaked PDF with broad wings ($K > 0$), where large values are more probable than in a Gaussian PDF. A Gaussian reaches the value 10^{-6} at six standard deviations, while the transport PDF in Fig. 2.7 only reaches this value at 13 standard deviations. It is also often skewed into the direction of the transport (i.e. if the mean is positive then the skewness is also positive). The exact shape depends on how much the signals for the field and the density fluctuations are correlated. The high probability of large transport events leads to a bursty or *intermittent* behaviour of the transport time evolution. The intermittent behaviour manifests itself in the scale resolved PDF, which grows more peaked at small scales. On TJ-K, this is work in progress [53].

A product of two nearly Gaussian quantities cannot also be Gaussian. Depending on the correlation $\gamma \in]-1, 1[$ between density and electric field fluctuations, the PDF of their product assumes a skewness $S \in [-2.83, 2.83]$

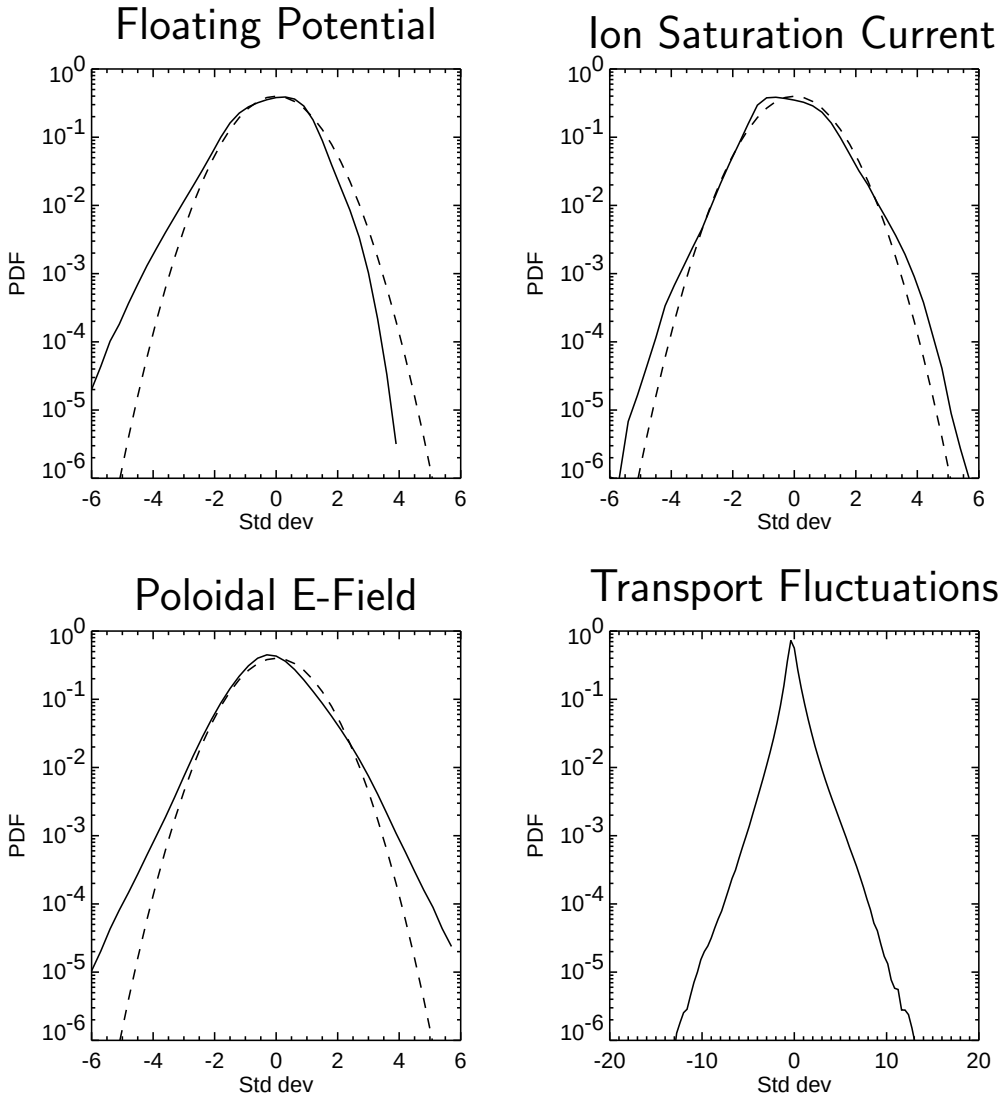

Figure 2.7: Normalised probability distribution functions (PDFs) of the floating potential Φ_{float}, the ion saturation current I_{sat}, the poloidal electric field $E_\theta = -\nabla_\theta \Phi_{float}$ and the transport fluctuations Γ from an ECRH discharge at $n = 1.2 \times 10^{18}\, m^{-3}$ and $T_e = 19\, eV$. The data was taken with the poloidal probe array and averaged over the flux surface. The dashed line represents a Gaussian distribution.

and a kurtosis $K \in [6, 12]$ [54]. The burstiness of the transport fluctuations is a direct consequence of the Gaussian character of the density and electric field fluctuations. The correlation and the cross phase α are directly related

$$\cos\alpha \equiv \frac{\left\langle \widetilde{E}_\theta \widetilde{n} \right\rangle}{\left\langle \widetilde{E}_\theta^2 \right\rangle^{1/2} \left\langle \widetilde{n}^2 \right\rangle^{1/2}} = -\gamma \tag{2.32}$$

The skewness S and kurtosis K can then be expressed completely in terms of α

$$\begin{aligned} S &= -2\gamma \frac{3+\gamma^2}{(1+\gamma^2)^{3/2}} \\ K &= 3\frac{3+14\gamma^2+3\gamma^4}{(1+\gamma^2)^2} - 3 \end{aligned} \tag{2.33}$$

An important prediction for the wave number spectra of turbulent flows was derived by Kolmogorov as early as 1941 [2, 3, 4]. It is usually referred to as "K41." In the limit of infinite Reynolds numbers, it is assumed that the turbulent flows are stationary, isotropic, homogeneous and scale invariant[1], at least in a statistical sense at scales smaller than the integral scale l_0 and away from boundaries and that the flow has a finite non-vanishing mean rate of energy dissipation ε per unit mass. Then the third order longitudinal structure function (see Eq. (2.26)) depends only on the longitudinal increment $l \ll l_0$ and the energy dissipation ε

$$\left\langle (\delta v_\parallel(l))^3 \right\rangle = -\frac{4}{5}\varepsilon l \tag{2.34}$$

which is called the *four-fifths law*.

From Kolmogorov's *two-thirds law* for the second order structure function follows the famous expression for the energy spectrum $E(k)$ of the flow:

$$\begin{aligned} \left\langle (\delta \mathbf{v}(l))^2 \right\rangle &= C\varepsilon^{2/3} l^{2/3} \\ E(k) &= C\varepsilon^{2/3} k^{-5/3} \end{aligned} \tag{2.35}$$

According to K41, the dimensionless constant C is the same for all flows (*universality*). This may not be true [1]. The turbulent energy spectrum is illustrated in Fig. 2.8. Energy is injected into the system at large scales l_0 and dissipated at small scales. The intervening wave number range through which the energy cascades is called the *inertial range*. The exponent in the power law is also called the *spectral index*.

[1] Basically, all symmetries of the Navier-Stokes equation are restored

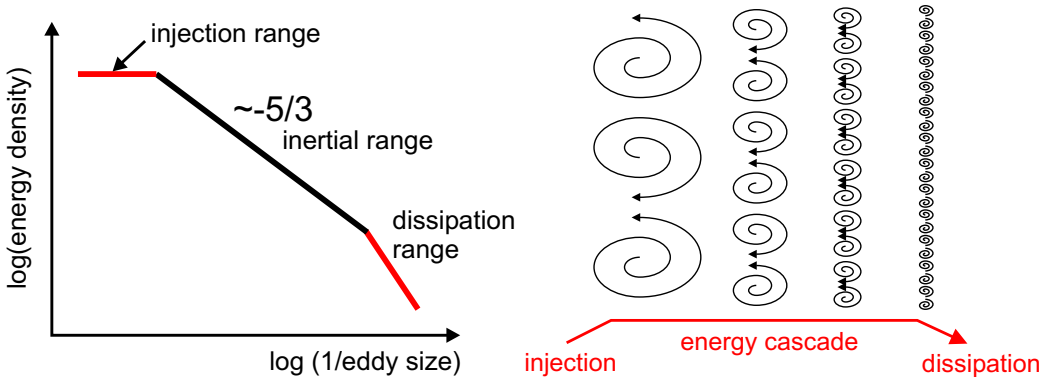

Figure 2.8: Energy spectrum according to K41. Turbulence is generated at the integral scale l_0. An energy cascade transfers the energy to the Kolmogorov dissipation scale $\eta = \nu^{3/4}/\varepsilon^{1/4}$.

These results apply only to three dimensional fluid turbulence. For magnetised plasma turbulence, the dynamics could be essentially two dimensional in the plane perpendicular to the magnetic field. Rotating fluids like the atmosphere of planets also show a two dimensional behaviour. In contrast to K41, there are now two inertial ranges with spectral indices $-5/3$ and -3 and a dual cascade of energy and enstrophy [5]. Figure 2.9 shows the schematic energy spectrum. The energy going into large scales implies the formation of eddies comparable in size to the whole system, which is indeed observed in the atmosphere of e.g. earth and Jupiter.

For turbulence in magnetised plasmas, it is not yet decided how important the three dimensional properties are compared to the two dimensional turbulence perpendicular to the magnetic field.

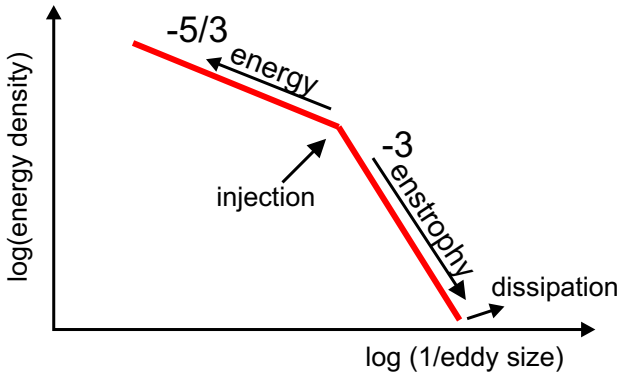

Figure 2.9: Energy spectrum for two dimensional fluid turbulence according to [5]. A dual cascade of energy and enstrophy is present.

Chapter 3

The Torsatron TJ-K

3.1 The Experimental Setup

TJ-K is an $l = 1, m = 6$ torsatron [22, 23] with a major radius of 0.6 m and a minor plasma radius of 0.1 m. The magnetic field strength B is up to 0.3 T, the rotational transform ι is about 1/3. Fig. 3.2 shows the main helical coil and the vertical field coils used to partially compensate the helical coil's vertical field. The small vertical field coils are not currently used on TJ-K. By varying the current in the vertical field coils with respect to the current in the main coil, the position and shape of the magnetic flux surfaces can be controlled, as can other field parameters like magnetic shear and magnetic well depth. Figure 3.3 shows flux surfaces that were calculated using the GOURDON field line tracing code [55]. Each contour shows the intersection of one magnetic field line with the poloidal plane as it is traced many times around the torus. The toroidal angles $\Phi = 10°, 30°, 50°, 60°$ correspond to the position of the 24 access ports on the vacuum vessel. Because of the sixfold symmetry of the main coil, the ports repeat every 60°. The 18 ports on the top, bottom and outboard sides are big ISO-KF250 flanges, while the six flanges on the inboard side are only ISO-KF63 because of the presence of the main coil.

The coils are connected in series to a 1200 A, 800 V cw power supply. For useful magnetic configurations, the current through the vertical field coils must be between a factor of $R_{v/h} = 0.44$ and 0.63 of the helical main coil current. To modify $R_{v/h}$, a resistor and a DC-to-AC converter are connected parallel to the vertical field coils. The current ratio $R_{v/h}$ is varied by adjusting the amount of current that is taken by the DC-to-AC converter and fed back to the grid. One of the effects of different current ratios is the shifting of the magnetic axis with respect to the torus axis. This is shown in Fig. 3.4

Figure 3.1: Picture of the TJ-K device in Kiel

for the standard configuration and the extreme inward and outward shifted configurations. The magnetic axis moves from $R = 59\,\mathrm{cm}$ to $R = 71\,\mathrm{cm}$ when $R_{v/h}$ varies from 0.63 to 0.44.

The primary vacuum system consists of a 1500 l/s turbo pump in conjunction with a rotary pump. An ISO-KF250 gate valve can be used to separate probe setups from the main vessel. A small rotary pump is used as a roughing system to achieve a pre-vacuum in the separated volume prior to reconnection. The lowest residual pressure that was achieved with all diagnostics attached is $3 \times 10^{-7}\,\mathrm{mbar}$. At this value, water is the dominant partial pressure.

The working gases helium, argon and hydrogen are continuously supplied to the torus and pumped out by the turbo pump. Reasonable pressures are between 2 and $5 \times 10^{-5}\,\mathrm{mbar}$ for ECRH and between 10^{-4} and $10^{-3}\,\mathrm{mbar}$ for helicon discharges. These are raw values from the pressure gauge. Actual pressures for helium and hydrogen can be higher by a factor of five, while argon pressures are lower by a factor around two. The uncorrected values are used throughout.

The vacuum vessel and the coil system was originally the TJ-1U experiment at CIEMAT, Madrid [22], whose support is gratefully acknowledged.

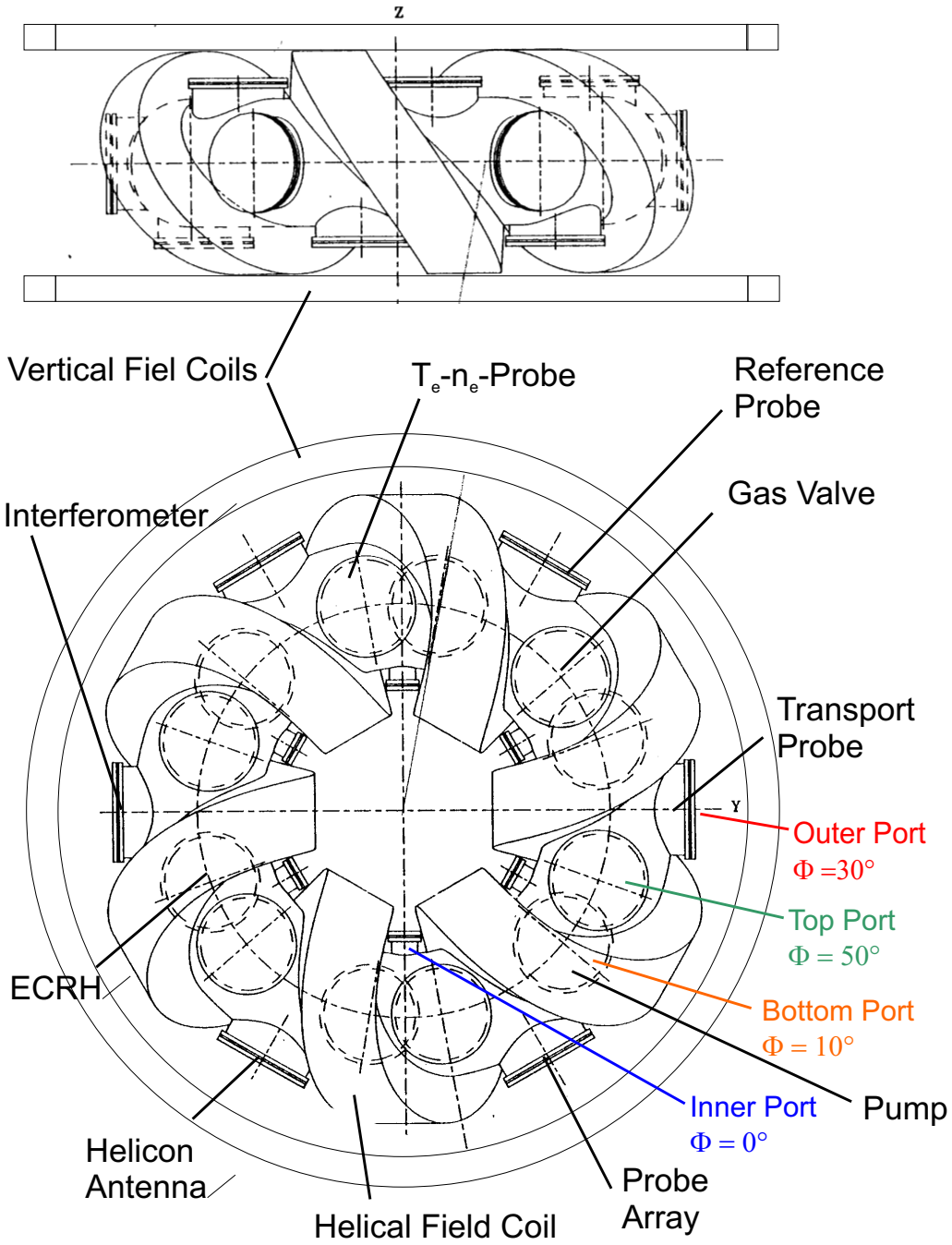

Figure 3.2: Coil system and vacuum vessel of TJ-K. Major and minor radius of the vacuum vessel are 0.6 and 0.175 m. The large vertical field coils have a diameter of 1 m. Also shown are the 24 access ports of the vacuum vessel.

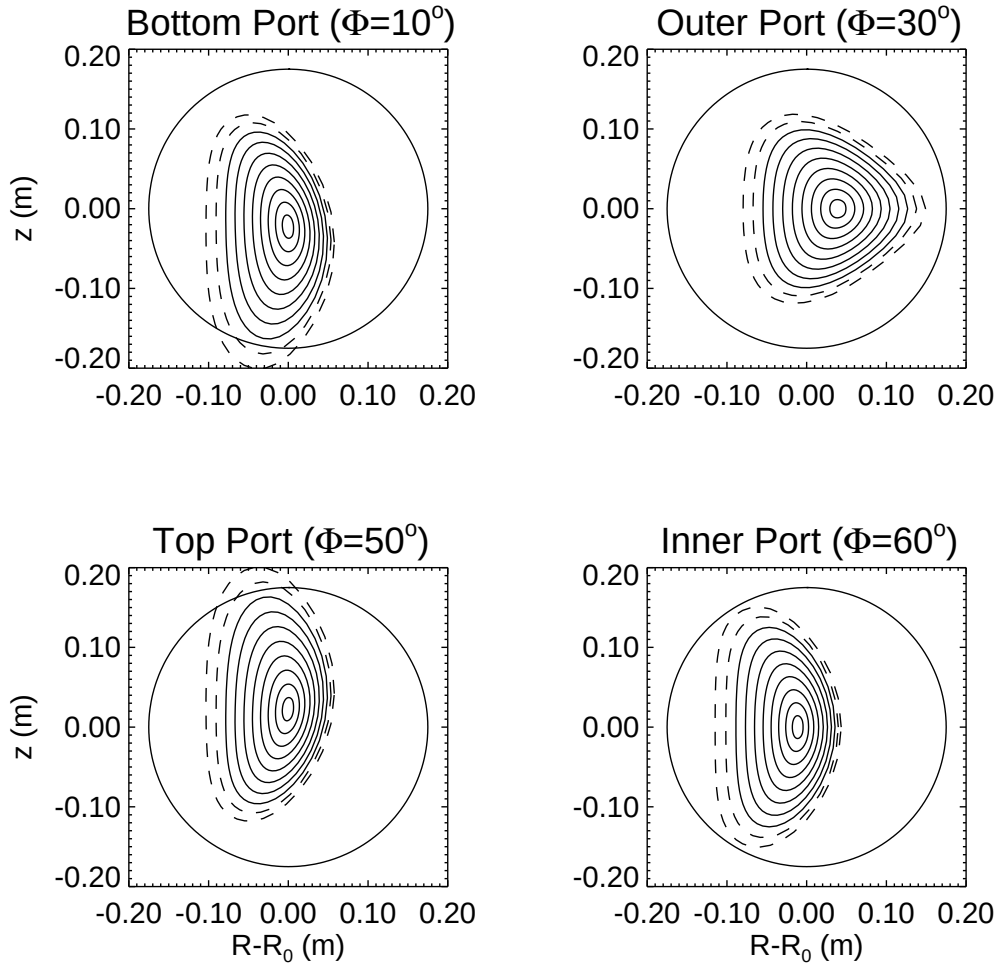

Figure 3.3: Poloidal cross section of the magnetic flux surfaces of TJ-K for a current ratio $R_{v/h} = 0.57$ at the toroidal locations of the ports. Dashed lines indicate that the flux surface intersects the vessel wall at some place. Φ is the toroidal angle at which the poloidal cross section is taken.

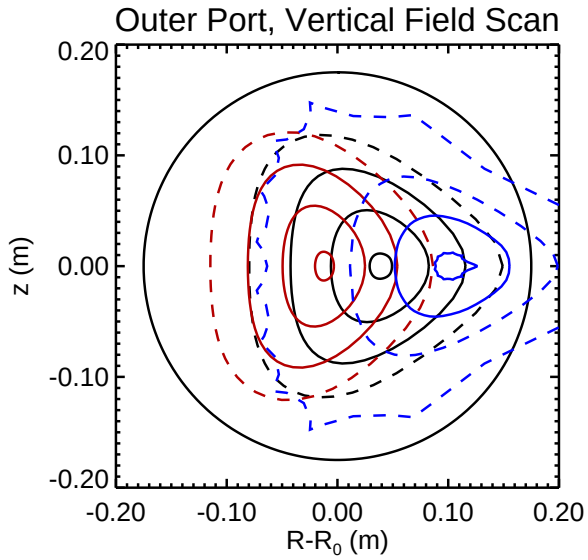

Figure 3.4: Magnetic flux surfaces of TJ-K at the toroidal position of the outboard port ($\Phi = 30°$). Red surfaces are for a current ratio $R_{v/h} = 0.63$ (inward shifted), black is the standard configuration $R_{v/h} = 0.57$, and blue is the extreme outward shift with $R_{v/h} = 0.47$. Dashed lines indicate that the flux surface intersects the vessel wall at some place.

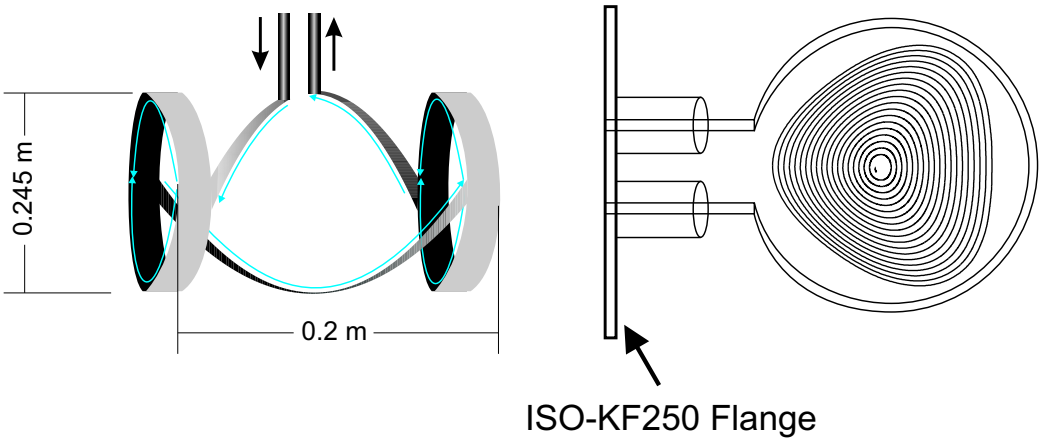

Figure 3.5: Left: Top view of the helicon antenna used in TJ-K. The circular parts enclose the plasma column. The connections come through an outboard port. Right: Position of the helicon antenna with respect to the magnetic flux surfaces.

3.2 Plasma Generation

There are two heating systems available in TJ-K, a helicon and an electron cyclotron resonance source. The 27.12 MHz helicon system uses a 3 kW radio frequency amplifier that is coupled to a special helicon antenna via an impedance matching network. Other frequencies are possible, but they are not normally used on TJ-K. The coupling is provided by a Nagoya type III half turn antenna as shown in Fig. 3.5. The antenna is coated with boron nitride in order to electrically insulate it from the plasma.

There are two mechanisms that couple the energy to the plasma. They are investigated in detail in [56]. In *inductive mode*, the currents in the antenna generate a varying magnetic field that induces currents in the plasma which cause heating. Since this happens close to the antenna at a radial position of about 10 cm, this mode is usually associated with hollow density profiles. In *helicon mode* [57], the field of the electromagnetic wave accelerates the plasma electrons directly. These *helicon waves* are basically whistler waves in bounded plasma. They depend on the magnetic field strength and propagate along the magnetic field lines. The exact energy coupling mechanism for helicon discharges in toroidal geometry is not fully understood. In a cylindrical geometry, a pure helicon discharge is characterised by a very high on-axis density that falls off rapidly towards the edges, where the antenna is located [58, 57, 59].

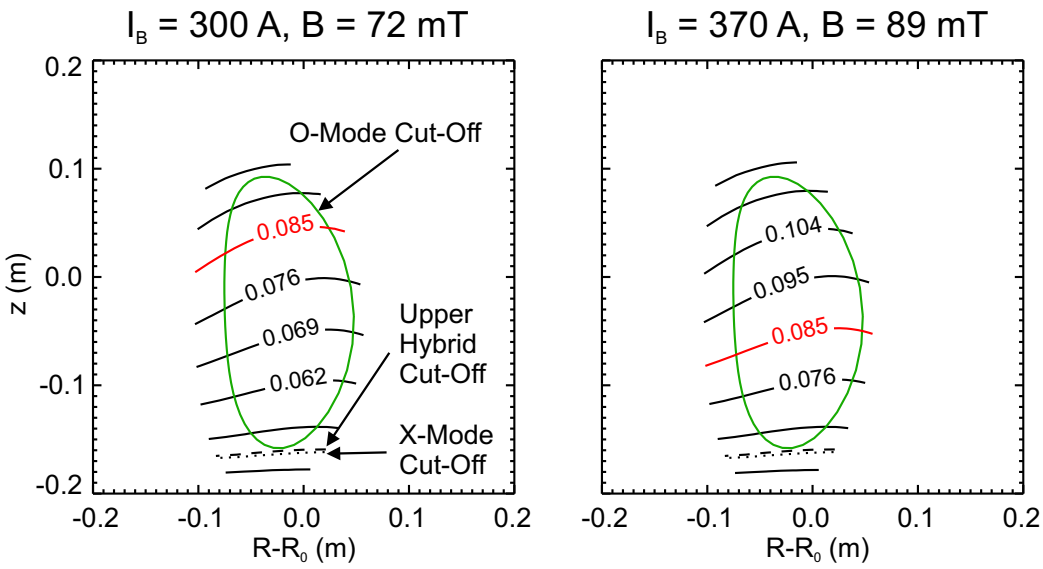

Figure 3.6: Contour plots of $|B|$ at the poloidal plane where the microwave is coupled to the plasma from a bottom port. The nominal magnetic field strengths are 72 and 89 mT, respectively. The electron cyclotron resonance layer at 85 mT is shown in red. The upper hybrid resonance, the X-mode and O-mode cut-offs for a plasma with a peak density of 10^{17} m^{-3} are indicated. Adapted from [60]

It is also possible that the electrical field between antenna and ground directly accelerates electrons *(capacitive mode)*. This is strongly hindered by the insulation of the antenna and the magnetic field which impedes the movement of the electrons perpendicular to it.

The advantage of the helicon system is that plasmas can be ignited at any desired magnetic field strength and that the magnetic field strength can be used for density control. A disadvantage is the proximity of the antenna to the plasma. Argon and helium both operate in the helicon mode and produce centrally peaked plasmas. In hydrogen, only inductively coupled hollow density profiles were achieved.

The second, more recently added system uses a 2.45 GHz microwave with a 6 kW magnetron. It is used for electron cyclotron resonance heating (ECRH) in the O-mode configuration, i. e. the electric field of the microwave is parallel to the confining magnetic field [61]. It was not possible to ignite a plasma using the X-mode. The microwave is coupled via waveguide through a quartz window in a bottom port. At nominal field strengths between 72 and 100 mT, the electron cyclotron resonance $\omega_{ce} = eB/m_e$ is within the

plasma radius. Figure 3.6 shows contours of the magnetic field strength $|B|$ on a poloidal cross section at the toroidal position of the bottom port with the important cut-offs and resonance layers indicated.

Since a resonant absorption is only expected in very hot plasmas and measured plasma densities in TJ-K are well above the cut-off density of $n = 7.1 \times 10^{16}\,\mathrm{m}^{-3}$, we suspect that we either have OXB conversion into electron Bernstein waves or that the absorption does indeed happen at the edge and we have an inward particle pinch which results in the observed centrally peaked density profiles. The investigations of the ECRH absorption process are just beginning. Throughout, the term ECRH will be used even if it may be a different absorption process.

Regardless of the actual heating mechanism, there are upper limits to the plasma density and temperature that depend on particle and energy losses alone. An energy and particle balance analysis [28] that incorporates the atomic processes (ionisation, recombination, excitation and elastic collisions) and transport shows which densities are attainable at a certain electron temperature. The model assumes a steady state plasma, in which particle sources (ionisation) are balanced by transport and recombination. The power balance demands that the input heating power is consumed by ionisation, radiation (because of collisional excitation of ions and neutrals by electrons), elastic collisions (electrons transferring energy to cold ions) and the loss of the kinetic energy of particles that recombine or are transported to the wall (convective heat loss). Conductive heat loss is taken to be proportional to convective heat loss. In the electron temperature range that is relevant for TJ-K ($T_e < 40\,\mathrm{eV}$), the atomic processes play the most important role in the discharge. Since we assume that the plasma parameters adjust themselves in such a manner that a steady state is reached, we do not make any assumptions with respect to the confinement properties of the plasma. The confinement is always such that the plasma is steady state. The model also cannot say which $T_e - n_e$ combination will actually be realised in the plasma. And, at last, the model uses a uniform temperature and density for the whole plasma volume of $0.12\,\mathrm{m}^3$.

Our results for the gases hydrogen, helium and argon at standard parameters are shown in Fig. 3.7. The general trend is that at constant heating power, high electron temperatures lead to low densities and vice versa. Since the various gases' atomic rate coefficients differ by factors of ten, it is not surprising that the curves for the density at any given temperature also vary accordingly, with helium densities larger than hydrogen and argon.

Another trend seen in Fig. 3.7 is that higher neutral densities lead to higher plasma densities (at reduced temperatures), because the ionisation rate is proportional to the neutral density. This does not hold for low tem-

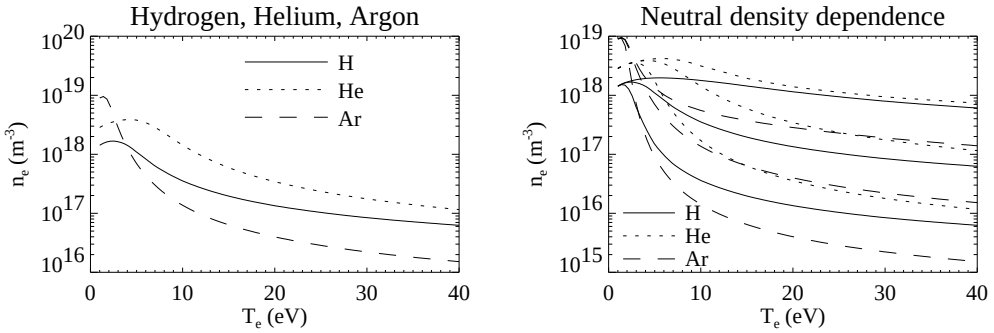

Figure 3.7: Plasma parameter limits from a particle and energy balance. The plots give the maximum attainable density for a given electron temperature. Left: Heating power is 3 kW, neutral pressure $p_0 = 10^{-4}$ mbar. Right: Same plot but with $p_0 = 10^{-5}$, 10^{-4}, and 10^{-3} mbar. At higher temperatures, the major losses (ionisation and excitation of neutrals) are proportional to n_0, so higher plasma densities correspond to lower *neutral densities.*

peratures, where ionisation is not a major process. Increasing the power at fixed T_e has the expected result of shifting the whole curve towards higher densities.

Actual measurements of temperatures and densities in TJ-K plasmas are presented in Secs. 3.4.1 and 3.4.2. Usually, the achieved parameters are well below the theoretical maximum. When they seem to exceed the maximum, this is due to uncertainties in determining the temperature and due to strong radial variations of the temperature, which remain undetected because of the single-point measurement.

3.3 Main Diagnostics in TJ-K

The diagnostics on TJ-K can be cast into two categories: (fast) turbulence diagnostics and (slow) discharge diagnostics. The latter are used for basic measurements of plasma density and temperature, which are used to classify our discharges and also to have an idea of the reproducibility of discharge parameters across different realisations of a specific discharge type. The microwave interferometer used for the density measurement is described in Sec. 3.3.1. Section 3.3.2 describes the slowly swept Langmuir probe that measures the electron temperature. No density measurements from this probe are used. In the near future, the ion temperature will be accessible through spectroscopy.

The turbulence diagnostics usually operate at a sampling frequency of 1 or 2 MHz. It is technically very demanding to operate swept Langmuir probes at these frequencies, so that on TJ-K, Langmuir probes used for turbulence measurements are operated either in the saturation current or the floating potential configuration (Sec. 3.3.2).

For investigations of the electromagnetic wave field of the helicon discharge, the $\dot{B}$ probes had to be sampled with 1 GHz, well above the helicon frequency of 27 MHz. The results are discussed elsewhere [56].

3.3.1 Microwave Interferometry

For the density measurement, we employ a single cord heterodyne microwave interferometer [62, 63, 64] at 64 GHz. Density measurements with electromagnetic waves rely on the fact that plasma's index of refraction N_P depends on the electron density. The phase shift incurred by a microwave traveling over a path l through a plasma with electron density n is

$$\begin{aligned} \Delta\Phi &= \int_0^l (N_P - N_{air})\frac{\omega}{c} dl \\ N_P &= \sqrt{1 - \frac{\omega_p^2}{\omega^2}} = \sqrt{1 - \frac{n}{n_c}} \end{aligned} \tag{3.1}$$

where ω_p is the plasma frequency and $n_c = 5.1 \times 10^{19}\,\mathrm{m}^{-3}$ is the cut-off density at 64 GHz, where the microwave frequency ω equals the plasma frequency. Electromagnetic waves below the plasma frequency cannot propagate because the plasma can instantaneously shield the electric field of the wave, which is consequently reflected. These considerations are valid for the O-mode, where the electric field of the microwave is parallel to the confining magnetic field.

The microwave feed-throughs and horn antennas are mounted on an outer port. The microwave traverses the plasma in the plane of the torus axis and is reflected by a mirror on the inboard side of the vacuum vessel. The reflected microwaves are received by a second horn antenna directly beside the emitting antenna. The phase shifted wave is fed back to the interferometer and mixed with the reference wave. After mixing to an intermediate frequency of 60 MHz, a phase comparator delivers a voltage that is proportional to the phase shift. From this phase shift, the integrated line density is calculated. For a chord length of four times the plasma radius $l = 4a = 40\,\mathrm{cm}$, the scale factor is $6.7 \times 10^{17}\,\mathrm{m}^{-3}/\mathrm{V}$.

3.3.2 Langmuir Probes

Langmuir probes are a powerful, yet technically undemanding diagnostic [65]. By sticking an electrode into the plasma, the electron density, temperature and plasma potential can be inferred by analysing the current-voltage characteristic of the probe. Good spatial resolution is possible, and with some limitations, even the time resolution necessary for turbulence measurements can be reached. The most serious limitation is the heat load that a material probe incurs in a plasma, which limits their use to plasmas temperatures $< 100\,\mathrm{eV}$. In fusion plasmas, Langmuir probes can only be employed in the edge regions, at best a few cm past the separatrix. In TJ-K, the whole plasma can be probed, which makes it so interesting for turbulence research. Application to fusion plasmas is treated in [66, 67].

When an insulated wire, with only the tip exposed, is inserted into a plasma, due to their higher mobility, more electrons than ions will flow onto it. If the probe is not connected (i.e. it is *floating*), it will be charged negatively until electrons and ions flows on the probe are ambipolar. The measured voltage is called the *floating potential* Φ_{float}. It can be measured with a high-impedance volt meter against (vessel) ground. Although the probe is charged negatively with respect to the plasma, it can still be at a positive potential with respect to ground.

When a bias voltage is applied, a probe characteristic like the one shown in Fig. 3.8 is obtained. Starting from the floating potential with zero current, a positive bias voltage has the effect of attracting more and more electrons until the *plasma potential* is reached, where all electrons that would normally intersect the area of plasma where the probe is now situated are collected by the probe. Increasing the voltage should yield no additional electron current (dashed blue line), the probe would go into electron saturation. But since the probe disturbs the plasma when it is not at plasma potential, its electric fields actively attracts electrons whose orbits would not normally have

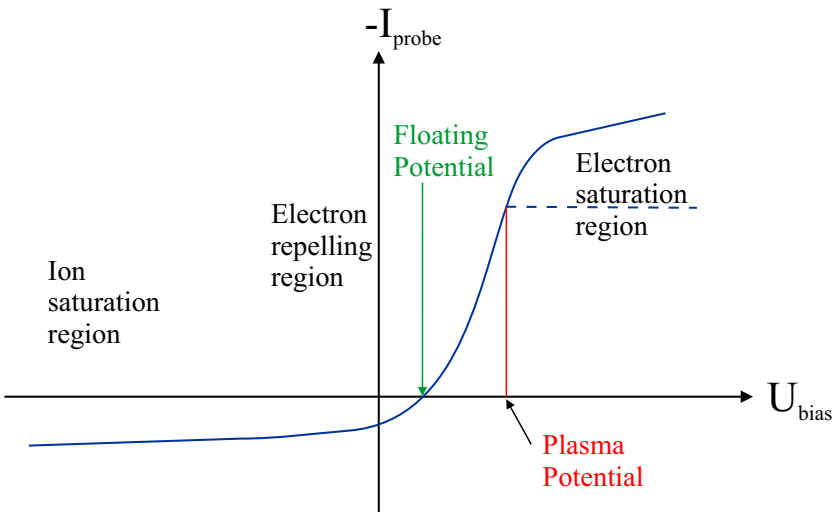

Figure 3.8: Idealised current-voltage characteristic of a Langmuir probe.

brought it onto the probe surface. The actual curve shape beyond the plasma potential is determined by the geometric shape of the probe: an infinitely large planar probe would indeed exhibit a saturation of the probe current, while a spherical or a cylindrical probe would show a further increase of the probe current.

A probe at plasma potential Φ_P has no potential barrier against charged particles impinging on its surface. If a negative voltage U_{bias} with respect to Φ_P is applied, a potential wall is raised that can only be overcome by electrons whose kinetic energy is sufficiently high. This region is called the *electron repelling region*, where the electron part of the probe current depends on the cumulative energy distribution of the electrons.

At high negative bias voltages, no electrons can flow to the probe and only the ions in the vicinity of the probe contribute to the probe current. As with the electron saturation current, the ion current does not really saturate, although the effect is usually much smaller. Due to the higher mass, the ion current is much smaller than the electron saturation current.

A quantitative analysis [65] for unmagnetised plasmas with cold ions yields the following expressions for the saturation currents $I_{e,sat}$, $I_{i,sat}$ and

the current I_e in the electron repelling region:

$$\begin{aligned} I_{i,sat} &= 0.61 \cdot enS\sqrt{T_e/m_i} \\ I_e &= I_{e,sat} \exp\left(\frac{-e(\Phi_P - U_{bias})}{T_e}\right) \\ I_{e,sat} &= -enS\sqrt{T_e/2\pi m_e} \end{aligned} \tag{3.2}$$

S is the surface area of the probe, n is the density of the plasma and T_e is the electron temperature in electronvolt, e is the unit charge and the particle masses are denoted by m. This simple picture does not take into account realistic probe geometries which prevent the electron current from saturating. In all cases, the characteristic changes from convex curvature in the electron repelling region to concave curvature in the saturation region. This transition can be exploited to determine the plasma potential Φ_P. It is also possible to recover the whole electron energy distribution function [68].

It also becomes apparent that in regions of high electron current, the ion current can be neglected, since $I_{e,sat}/I_{i,sat} \sim \sqrt{m_i/m_e}$. The case of hot ions is not discussed here.

From Eq. (3.2) it follows that high electron temperatures stretch the Langmuir characteristic along the U_{bias} axis. Looking at Fig. 3.8 it becomes apparent that this results in a bigger difference between Φ_P and Φ_{float}. The quantitative relation is

$$\Phi_{float} = \Phi_P + 0.61\frac{T_e}{e}\ln\sqrt{2\pi\frac{m_e}{m_i}} \tag{3.3}$$

Substituting Eq. (3.3) into Eq. (3.2), a formula is obtained that contains T_e and n as free parameters which can be fitted to experimental Langmuir characteristics.

The spatial resolution of the probe is limited be the sheath and presheath thickness, which can extend to several Debye lengths. Another issue is that the drawing of high saturation currents can influence the whole plasma equilibrium and dynamics.

For fast turbulence measurements ($f > 100\,\mathrm{kHz}$), it is very demanding to acquire an entire characteristic for each data point and determine n, T_e and Φ_P from that [69]. For this reason, only the ion saturation current (at a fixed bias voltage) and the floating potential are measured. The ion saturation current gives an estimate of the plasma density and the floating potential is taken as a measure of the plasma potential. Especially when the main interest is in the fluctuations, this is a valid approach if temperature fluctuations can be neglected. This has been studied in [20]. In the following,

saturation current and floating potential will be used interchangeably with density and potential.

One important aspect that has so far been neglected are the effects of magnetic fields on the characteristic. When the probe is smaller than the gyro radii of the particles (low field strength), the probe is unaffected by the field. If the probe size is comparable or larger than the gyro radii, then the reduced mobility of the particles perpendicular to the field will cause the forming of a depleted flux tube around the probe, diminishing the electron saturation current. While the temperature measurement is normally still usable, the density will have a large systematic error. An approach that takes this anisotropy into account by using a diffusion model [70, 71] also makes it possible to recover the electron energy distribution function.

When the Langmuir probe is swept much slower than the dynamics in the plasma, an averaged characteristic is obtained. The plasma parameters determined from this characteristic need not necessarily be the average of the fluctuating plasma parameters, since the characteristic is highly non-linear. In rf generated plasmas, the plasma potential oscillates with the rf frequency, often by many T_e/e. When this oscillation is rectified at the characteristic, the resulting analysis would normally overestimate the electron temperature. An rf compensation method has been proposed [72], but it is not used on TJ-K, since the part around the floating potential that is used for determining T_e is relatively insensitive to the rf distortion. For microwave plasmas, the oscillations are too fast to have such an effect on the characteristic. At TJ-K, the more serious problem was rf noise that couples into the data acquisition system between the filters and the digitisers.

3.3.3 Emissive Probes

Emissive probes are a way of measuring the plasma potential directly. By direct or indirect heating, an electron current is generated that flows from the probe to the plasma. In the total probe current, this counts like an ion current, because it flows into the opposite direction compared to the normal electron current. The effect of this extra current is shown in Fig. 3.9. Above the plasma potential, the emitted electrons are re-absorbed by the probe. Below the plasma potential, the electrons can flow into the plasma, causing a sharp fall in the probe characteristic. The floating potential is now much nearer to the plasma potential. Thus, a measurement of the floating potential practically yields the plasma potential.

Technically, emissive probes are built by executing the probe tip as a tungsten loop through which the heating current flows. The current is increased until the probe characteristic is sufficiently deformed. The heat load

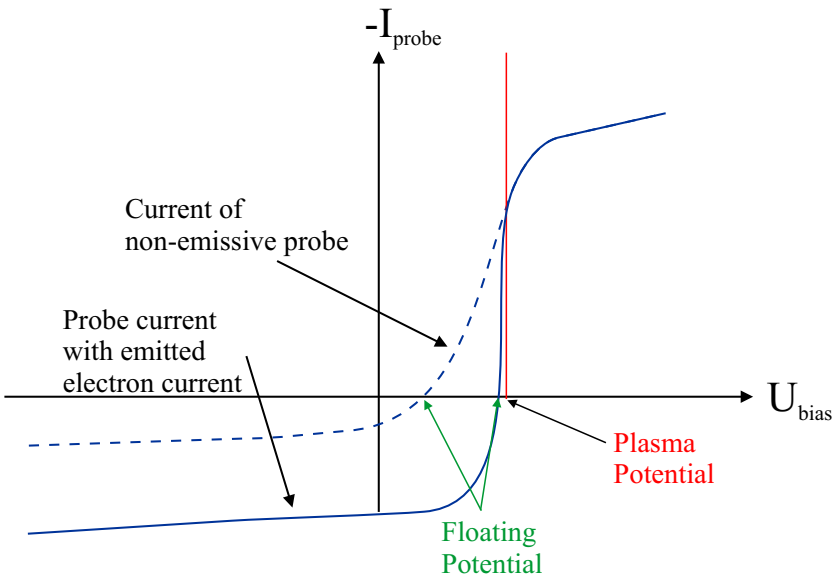

Figure 3.9: Idealised current-voltage characteristic of an emissive Langmuir probe. The emitted electron current counts like a large increase in the ion current, shifting the floating potential nearer to the plasma potential.

from the plasma can heat a probe indirectly. The difference between an optimally adjusted emissive probe and a burnt out emissive probe is small. Due to technical difficulties in ensuring a proper connection between the probe tip and the current feeds and the volatility of emissive probes in the relatively high temperature plasmas in TJ-K, no emissive probes were used for turbulence measurements.

3.3.4 The Transport Probe

All Langmuir probes in TJ-K are made from alumina ceramic tubes with a diameter between 0.6 and 2.7 mm, a length of up to 400 mm and up to four bores. A 200 μm diameter tungsten wire serves as electrode and conductor to the LEMO connector in the stainless steel mounting bracket. The mounting bracket is connected to electrical vacuum feed-throughs with coaxial teflon insulated wires, whose shield is only connected at the vacuum feed-throughs. See Fig. 3.10 for the tip configuration of the transport probe. The setup allows the simultaneous measurement of the radial and poloidal electric field in the chord through the torus axis (in the approximation that $\nabla\Phi \approx \nabla\Phi_{float}$) and the density (in the approximation that the temperature fluctuations can

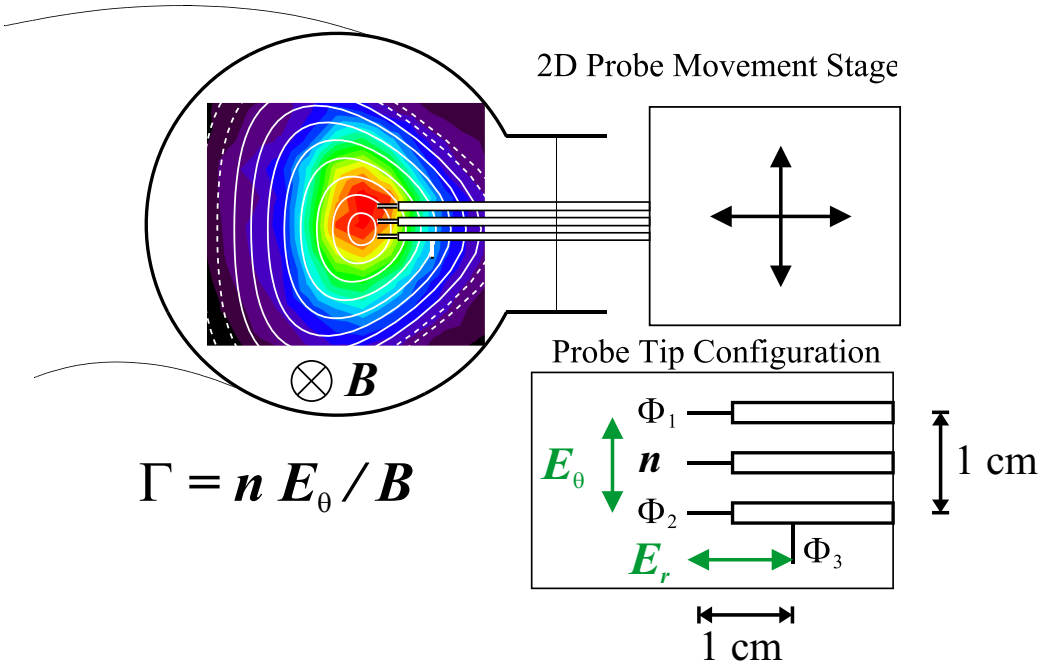

Figure 3.10: Schematic drawing of the movable transport probe with four tips. The vacuum vessel is outlined in black. The turbulent transport Γ *is defined in Eq. (2.18).*

be neglected). Above or below the chord of the torus axis, the electric field measurements do not coincide with the radial and poloidal direction anymore. When a whole poloidal cross section is measured, only density and potential measurements are done.

Positioning of the probes is achieved with servo motor driven movement stages, where the position can be set freely in the whole poloidal cross section via a LabView program that also controls the data acquisition. In some discharges, the presence of the probe influences the plasma to the point of e.g. reductions in interferometer determined density by ten percent.

An extra Langmuir probe is set up to acquire probe characteristics for determination of the electron temperature. It is mounted on a radial movement stage. Reference probes for the conditional averaging measurements were either mounted in additional movement stages or probes from the probe array were taken.

The measurement of the floating potential requires a high-impedance voltage measurement against vessel ground. The Tektronix AM502 amplifiers are used for low-pass filtering and driving the lines to the digitiser card in a Lab-

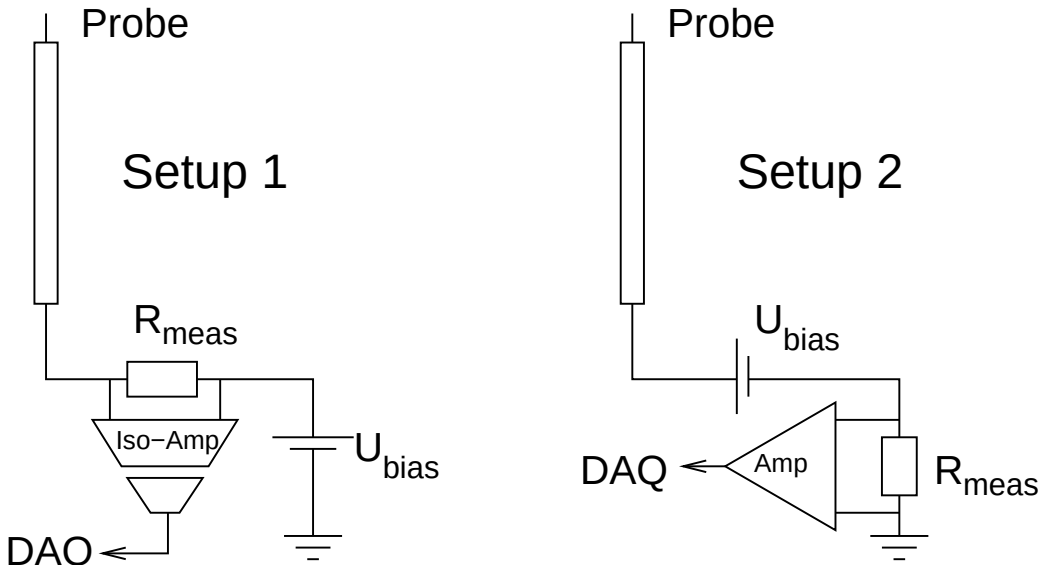

Figure 3.11: The two variants for measuring the probe current. Instead of the isolation amplifier, a DC-stop can be used, if only fluctuations are to be measured.

View controlled PC. Usually, a 20:1 voltage divider is necessary. Since the coaxial cable's capacitance, together with the plasma impedance, forms a low-pass filter, it is imperative that cable connections between probe and amplifier be kept short. In our case, they are below 1.5 m.

For the probe current measurement, a bias voltage is applied to the probe and the drawn current is determined by measuring the voltage drop over a shunt resistor (R_{meas} in Fig. 3.11). There are two possibilities for connecting the bias voltage supply and the shunt resistor with respect to ground. On TJ-K, setup number two is used, with a single 90 V battery pack for the ion saturation current bias voltage. Batteries have the advantage that they are guaranteed to be ground-free, as opposed to most commercially available power supplies.

3.3.5 The Poloidal Probe Array

The 64 probes of the poloidal probe array are mounted on a two-piece stainless steel mounting bracket, shown in blue in Fig. 3.12. The probe tips are arranged on a flux surface at about half the typical plasma radius. Each probe is individually mounted and connected to the SMB connector vacuum feed-through by a shielded coaxial cable. The finished array is shown in

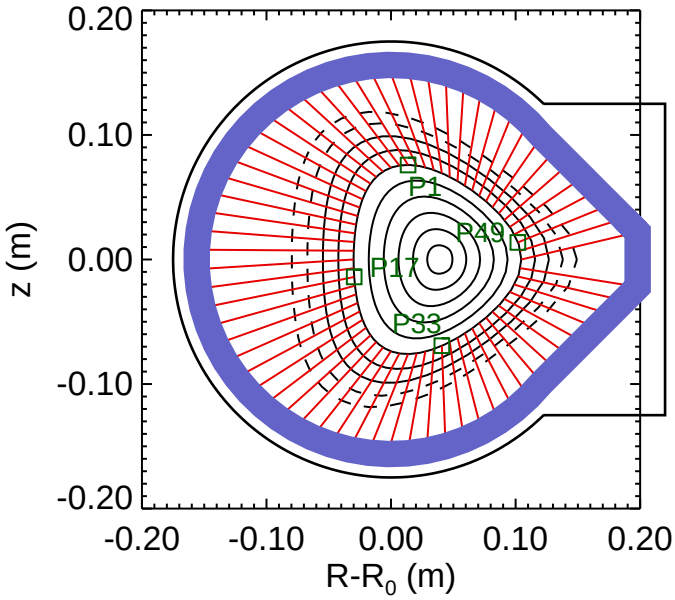

Figure 3.12: Schematic drawing of the poloidal probe array. The 64 probes shown in red are positioned on a flux surface at about half the plasma radius. The stainless steel mounting frame (blue) extends into the outer port flange on the right hand side. The vacuum vessel is outlined in black.

Fig. 3.13. Figure 3.17 on page 60 shows the array during an argon ECRH discharge. The circumference of the flux surface is 37.6 cm for the helicon discharges and, after a remodeling, 44.3 cm for the ECHR discharges.

For the probe array, neither 64 bias voltage supplies, nor 64 isolation amplifiers were available, so a modified setup with a capacitor instead of an isolation amplifier was used (Fig. 3.14). For ion saturation current measurements, all probes are connected to the single bias voltage battery pack. The voltage drop over the shunt R_s plus the bias voltage is connected to the capacitor C that strips off the DC signal, allowing only the (small) fluctuations to pass to the data acquisition system. The voltage divider module can be added independently.

The data acquisition system is a Nicolet 64 channel transient recorder with a memory of one megasample per channel. The maximum sample rate is 1 MHz.

For the helicon discharges, the voltage divider was used only for the float-

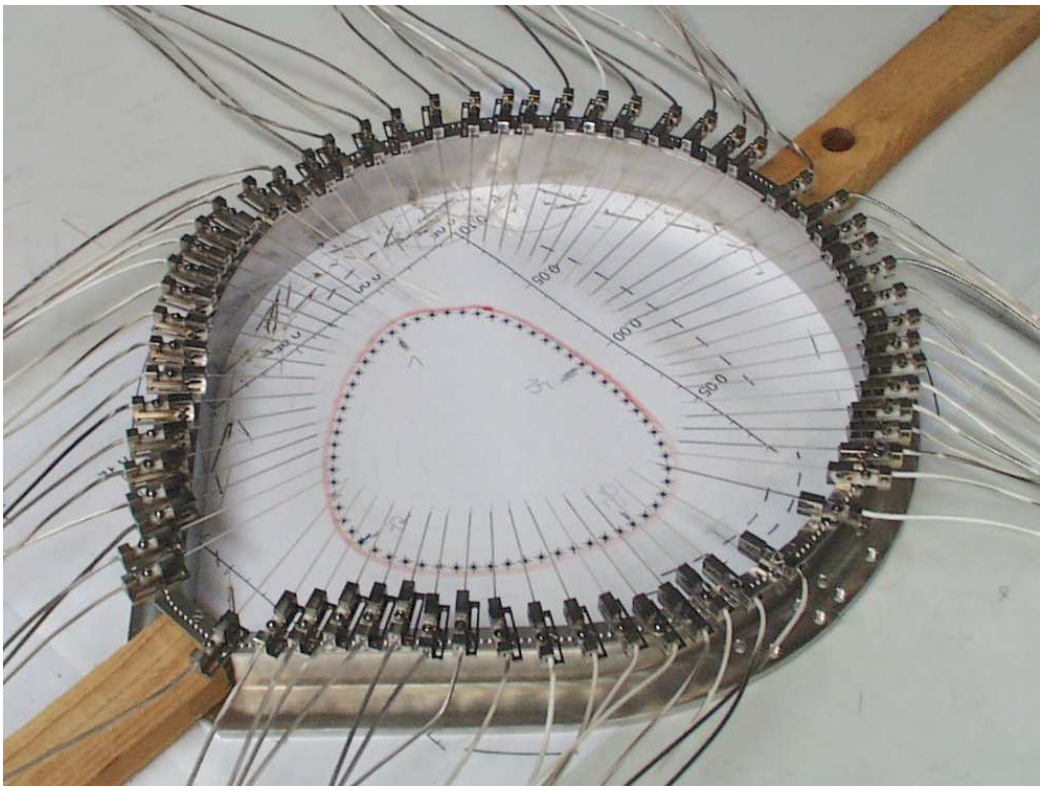

Figure 3.13: Picture of the completely assembled poloidal probe array with 64 tips, prior to installation in TJ-K. The red line denotes the flux surface onto which the probes are positioned, with the tips just touching the black dots.

ing potential measurements, while a 100 Ω resistor was used as a shunt for the ion saturation current measurement. For the ECRH discharges, an improved system using a permanent 61:1 divider and a 22 kΩ shunt were used. It was found that for ECRH discharges, the value of R_s should be at least 10 kΩ, otherwise there would be too much cross talk between ion saturation channels. The helicon discharges did suffer a small degree of cross talk.

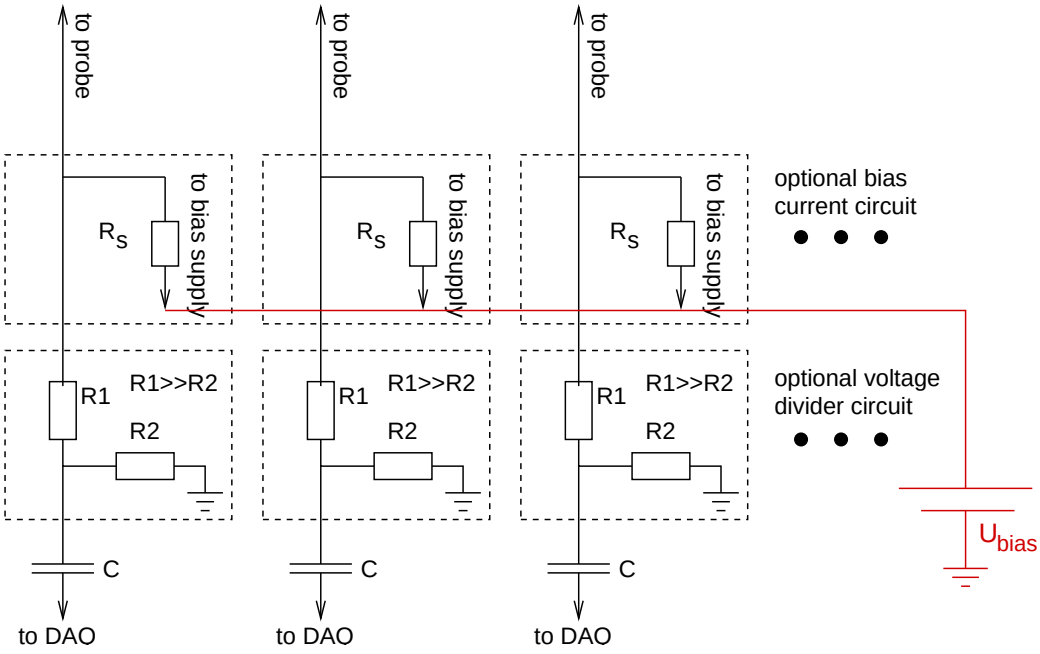

Figure 3.14: Modular probe circuits for the 64 tip probe array. The bias voltage supply connects to ground. The high bias voltage is rejected by the capacitor C before the fluctuating part is routed to the data acquisition system (DAQ).

3.4 Plasma Properties

3.4.1 Helicon Plasmas

Discharges with helicon heating were carried out at a residual pressure of 2×10^{-6} mbar with working gas pressures of usually $p_0 = 10^{-3}$ and 10^{-4} mbar in the various gases. The magnetic field strengths ranged from $B = 70$ to 270 mT, with $R_{v/h} = 0.57$ for helium and argon and $R_{v/h} = 0.60$ for hydrogen. The rf power was $P_h = 1$, 2 or 3 kW. From several antenna configurations, the boron nitride insulated design with the largest diameter has proven to yield the best results [56]. This refers to the achieved densities as well as the radial density profile, which was preferred to be centrally peaked. The antenna (Fig. 3.5) is a Nagoya type III half turn antenna with a diameter of 24.5 cm which encloses most of the plasma column. This means that the antenna does not act as a loss surface for the bulk plasma, which could introduce unwanted effects into the plasma dynamics. The helical half turn design selectively excites the $m = \pm 1$ helicon mode, which is circularly polarised around the magnetic field direction. It is commonly used for plasma production [58, 57, 59].

Figure 3.15 shows the achieved densities and electron temperatures for various values of neutral pressure and magnetic field. Densities are always line-averaged values from the interferometer and temperatures are always from Langmuir probe measurements near the center. The general trend is that argon plasmas are at higher densities and lower temperatures, while helium plasmas are hotter and less dense. Hydrogen has even lower densities at higher temperatures. For all gases, discharges at higher neutral pressures yield higher plasma densities, albeit at reduced temperatures. In a plasma parameter study [28],done before the magnet current ratio $R_{v/h}$ could be controlled, shows the same trends at $R_{v/h} = 0.44$.

Figure 3.16 shows poloidal profiles of ion saturation current and floating potential of all gases with calculated flux surfaces overlayed in white. They were measured with the transport probe (Fig. 3.10) with timeseries of 0.5 s length at a sampling frequency of 1 kHz. A profile is measured during a single 10 min discharge. Qualitatively, all discharges of one gas have similar properties, regardless of magnetic field strength, neutral gas pressure or rf heating power. The comparison with the microwave plasmas will be given in the next section.

A significant feature of hydrogen discharges is the strongly hollowed density profile, whereas helium and argon have centrally peaked profiles. The density of the hydrogen plasmas seems to be lower on the outboard side, which is at least partially due to the low spatial resolution (20 mm) of the

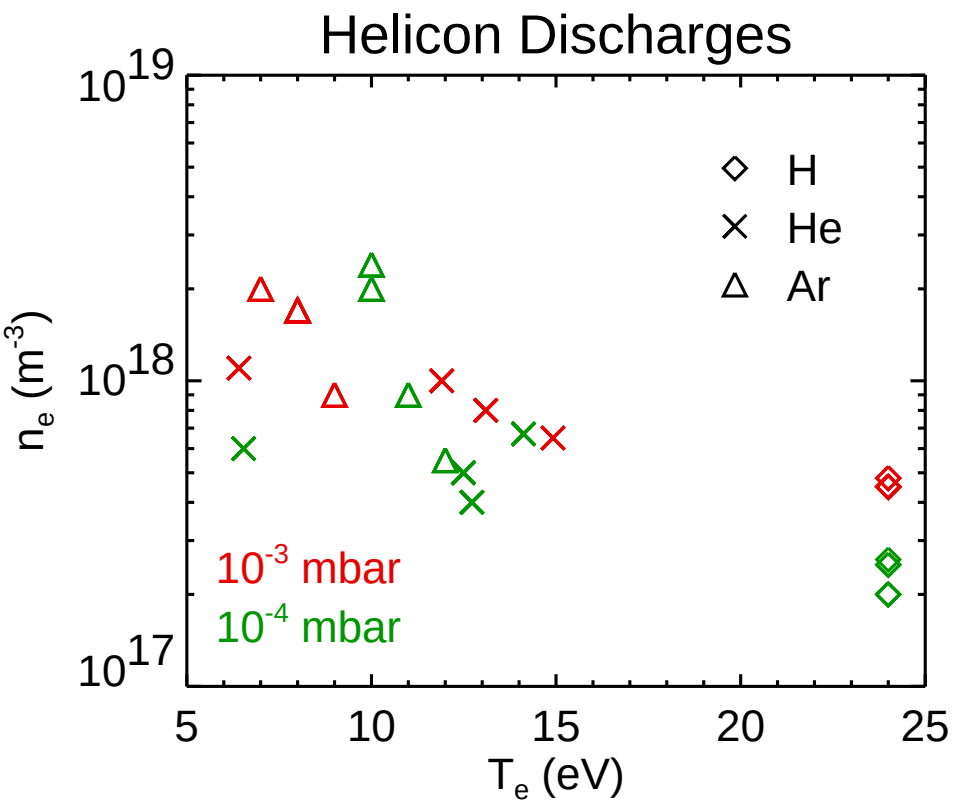

Figure 3.15: Densities and temperatures of helicon discharges in TJ-K, broken down by gas and neutral pressure. Red means high, green means low neutral pressure. Lighter gases tend to higher temperatures at lower densities.

measurement, which would miss the peak of a density ring that is only 40 mm across. Helium plasmas are strongly peaked, with a nearly constant density gradient going all the way from the center to the edge. Argon has steeper gradients and a small dip in the center, resulting in a plateau shape. Agreement of equi-density contours and flux surfaces is not perfect, even after taking into account the low spatial resolution of the density measurement. Preliminary measurements [73, 23] of the magnetic surfaces have shown differences between calculated and actual flux surfaces. Error fields, which would distort the flux surfaces, have not been investigated yet.

Fluctuation strengths are universally high at the edges, where the density is low, and low at the density maxima. In the three discharges chosen here, argon has the lowest fluctuation level going from 2% in the center to 15% at

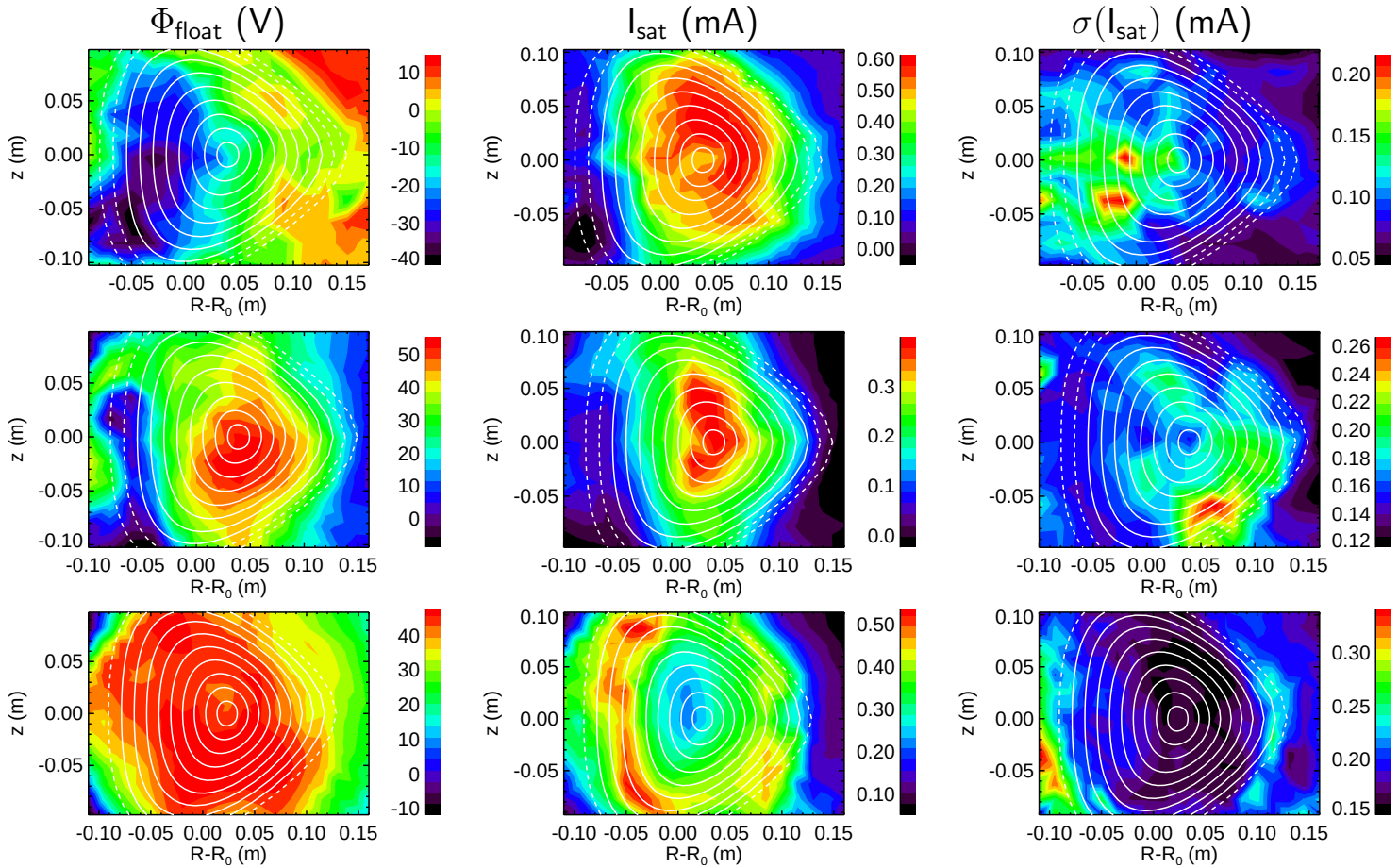

Figure 3.16: Poloidal plots of floating potential and ion saturation current for helicon discharges in argon (#812, top row, with $B = 144\,mT$, $p_0 = 10^{-4}\,mbar$, $P_h = 1\,kW$), helium (#922, middle, with $B = 72\,mT$, $p_0 = 10^{-4}\,mbar$, $P_h = 2\,kW$) and hydrogen (#964, bottom row, with $B = 72\,mT$, $p_0 = 10^{-3}\,mbar$, $P_h = 2\,kW$). Calculated flux surfaces are overlayed in white, dashed lines are open flux surfaces. The right column shows the fluctuation amplitude of the ion saturation current. The measurement grid is 20 mm by 20 mm.

the (inward) edge. Next is hydrogen with 6–20%, followed by helium with 6–35%. Fluctuations and transport are investigated in Chap. 4.

In fusion plasmas, the equi-potential contours are expected to coincide with the flux surfaces, just like the density. This is the case for hydrogen, although the profile is much less hollowed than the density profile. The profile for helium shows a significant departure both from the flux surfaces as well as from the density profile, but they are within acceptable limits, whereas the argon potential profile does not fit at all with the flux surfaces or the density profile. These deviations seem to be a particularity of the helicon discharge, and are totally absent in ECRH discharges (Sec. 3.4.2) and also in some helicon discharges in argon. Both helium and hydrogen exhibit a positive potential of about 40 V at the center which goes to near zero values at the edge. This results in a global counter-clockwise $E \times B$ drift.

The normalised parameters $\hat{\beta}$, $\hat{\nu}$ and ρ_s (see Sec. 2.1.5) that were achieved during helicon discharges at different control parameters are:

Gas	ρ_s (mm)	$\hat{\nu}$	$\hat{\beta}$
Argon	6.5–31.1	5.5–52.8	0.082–0.64
Helium	2.0–10.9	1.2–11.1	0.041–0.76
Hydrogen	1.9–7.0	0.09–0.2	0.028–0.85

One important aspect of helicon discharges in TJ-K is the presence of the helicon antenna, which intersects the edge of the plasma and influences the plasma dynamics. It has also been observed that “hot spots” of plasma production are located near the antenna.

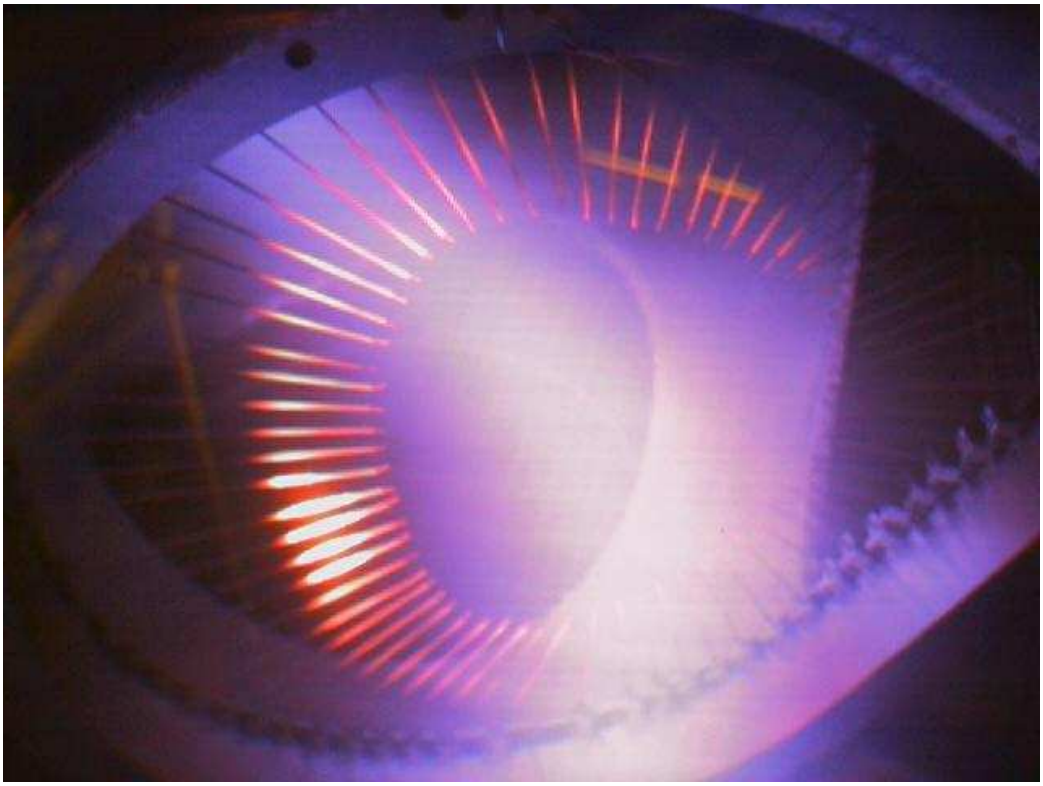

Figure 3.17: Image of an argon ECRH discharge with a line-averaged density of $n_e = 1.6 \times 10^{18}\,m^{-3}$ and $T_e = 12\,eV$. The view is from a top port onto the poloidal probe array (Fig. 3.12). The heat load on the alumina ceramic probe shafts makes them glow orange. The core plasma is visible as a whitish column.

3.4.2 Microwave Plasmas

Only recently, microwave heating (ECRH) became available on TJ-K. The ECRH discharges discussed here were all conducted at a residual pressure of $< 7 \times 10^{-7}$ mbar. The quartz microwave window was separated from the plasma by a 40 cm piece of vacuum wave guide. The helicon antenna was removed in order to avoid any influence of the loss surface represented by the antenna. Working gas pressures were $p_0 = 2 \times 10^{-5}$ and 5×10^{-5} mbar; the magnetic field strength was limited by the resonance condition to $B = 70$–100 mT, but not all field strengths lead to stable discharges. In all cases, a magnet current ratio of $R_{v/h} = 0.57$ was used. The microwave power was $P_h = 600$ and 1800 W. A visible light image of an argon discharge is shown in Fig. 3.17, which also shows the poloidal probe array that was present in

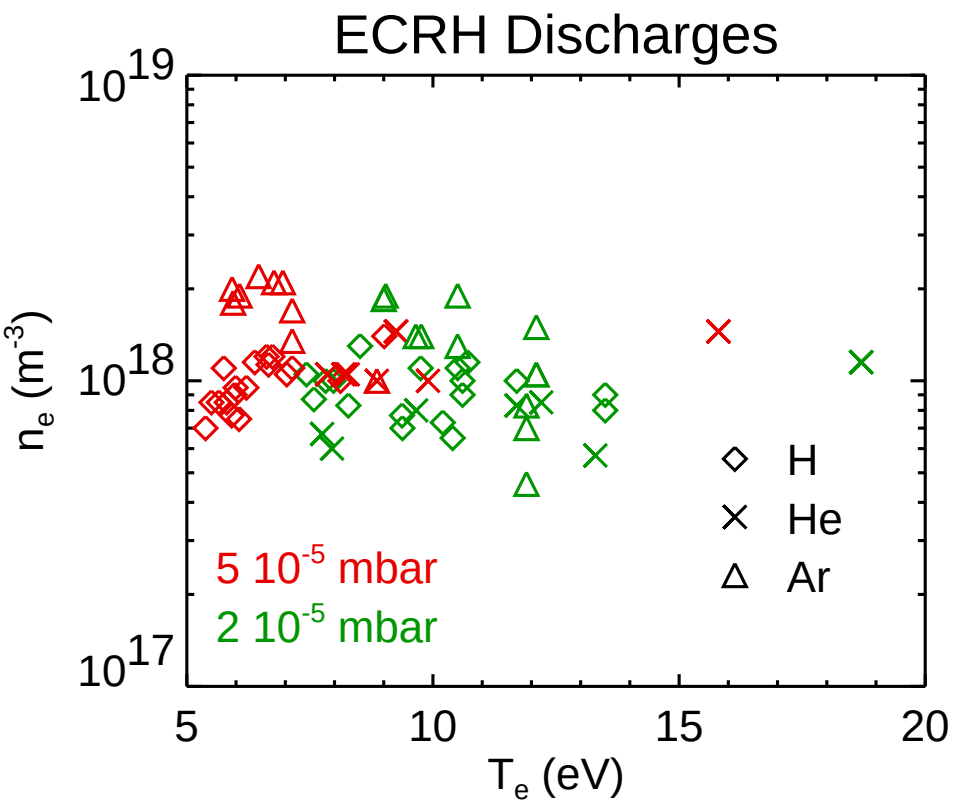

Figure 3.18: Densities and temperatures of ECRH discharges in TJ-K, broken down by gas and neutral pressure. Red means high, green means low neutral pressure. There is no clear preference of a particular gas for a certain density or temperature domain.

all discharges. If the array has any effect on the plasma dynamics, it is the same in all discharges.

The plasma densities and temperatures achieved with microwave heating are plotted in Fig. 3.18. Densities are line-averaged values from the interferometer and temperatures are from Langmuir probe measurements near the radial position of the probe array ($z = 0$, $R - R_0 = 9\,\mathrm{cm}$). In every discharge, the density clearly is well above the cut-off density $n = 7.1 \times 10^{16}\,\mathrm{m}^{-3}$.

In contrast to the helicon discharges, the gases do not prefer particular density or temperature domains. A striking trend is the low temperature of all discharges at the high neutral pressure. In contrast, there is only a slight trend that high density discharges also have a lower temperature. One might speculate that the microwave couples more efficiently to higher temperature

plasmas, so that a high density discharge can be sustained despite the higher power losses that are a consequence of the high temperature. The energy and particle balance for TJ-K plasmas has been investigated in more detail in [28].

Selected poloidal profiles of ion saturation current and floating potential are shown in Fig. 3.19, measured with the transport probe (Fig. 3.10). As with the helicon heating, the saturation current profile for argon shows a plateau shape with steep gradients and a nearly constant value at the center; the helium plasmas have similarly steep gradients, but a smaller plasma radius and a small dip at the center. Hydrogen has a pronounced hollow density profile with steep gradients, just as with helicon heating. Agreement with the theoretical flux surfaces is rather good, although there is some systematic rounding of the actual profile on the right (outboard) side. The relative fluctuation strength is low at the center and rises towards the edge. For helium it is 10–40%, for hydrogen 5–30% and for argon 5–40%.

In stark contrast to the helicon plasmas, the floating potential is practically congruent with the density, at least for argon and helium. In hydrogen, the potential follows the flux surfaces, but it is peaking in the center, regardless of the hollow density profile. A common feature of all gases is the positive value of 1–10 V at the center which decreases to negative tens of volts at the scrape-off layer and rises sharply again at vessel wall. This means that the global $E \times B$ drift runs counter-clockwise in the bulk plasma and clockwise outside the plasma. This flow reversal at the plasma edge is also observed in fusion plasmas, known as the shear layer of the plasma.

The normalised parameters $\hat{\beta}$, $\hat{\nu}$ and ρ_s that were achieved during ECRH discharges are:

Gas	ρ_s (mm)	$\hat{\nu}$	$\hat{\beta}$
Argon	16.4–31.2	4.7–72.7	0.28–1.57
Helium	5.9–11.3	1.5–7.2	0.11–1.81
Hydrogen	2.5–4.7	1.0–6.8	0.17–0.99

While ECRH discharges lack the flexibility of the helicon discharges in choosing the magnetic field strength, the achieved profiles are in better agreement with the flux surfaces and rf pickup of probes is not an issue.

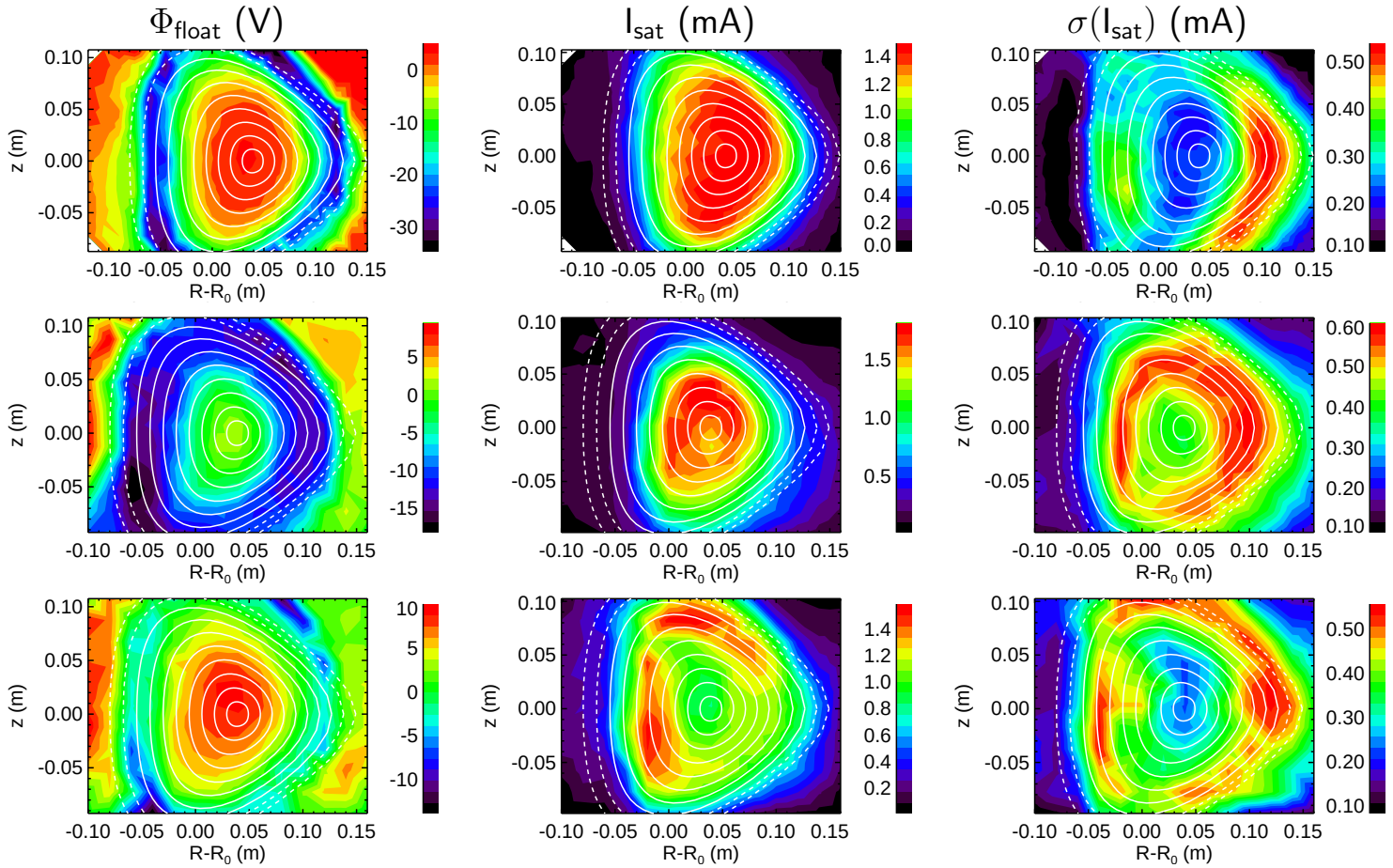

Figure 3.19: Poloidal plots of floating potential and ion saturation current for ECRH discharges in argon (#1761, top row, with $B = 72\,mT$, $p_0 = 5 \times 10^{-5}\,mbar$, $P_h = 1.8\,kW$), helium (#1885, middle, with $B = 72\,mT$, $p_0 = 5\times10^{-5}\,mbar$, $P_h = 1.8\,kW$) and hydrogen (#1921, bottom row, with $B = 89\,mT$, $p_0 = 5\times10^{-5}\,mbar$, $P_h = 1.8\,kW$). Calculated flux surfaces are overlayed in white, dashed lines are open flux surfaces. The right column shows the fluctuation amplitude of the ion saturation current. The measurement grid is 20 mm by 20 mm.

Chapter 4

Results

In this chapter, the results of the fluctuation measurements will be presented. Basically, three types of measurements were done on TJ-K, each with specific characteristics.

Radial profiles of the floating potential Φ_{float}, the ion saturation current I_{sat}, the poloidal $E \times B$ velocity v_θ and the radial transport Γ_r were measured with the transport probe (see Sec. 3.3.2) in order to see the radial variation of these properties. In addition, profiles of the background ion saturation current and floating potential were measured in the whole poloidal plane.

The conditional averaging method was employed for constructing a picture of the temporal and spatial evolution of coherent structures in the poloidal plane, as described in Sec. 2.5.4. The data was taken in the whole poloidal plane by the transport probe, with additional fixed position probes for the reference signals.

The results from conditional averaging show the shape of the turbulent structures, their poloidal and radial dimensions and propagation, and whether they occur as single blobs, dipoles or periodic quasi-coherent modes. Special emphasis is put on the cross phase between density and potential structures and the flows created by the fluctuating potential. An attempt at a crude scale separation is done by band-pass filtering the data in the frequency domain.

At last, results from the poloidal probe array (Fig. 3.12) will be presented. It allows the simultaneous measurements of the floating potential Φ_{float}, the ion saturation current I_{sat} and the radial transport Γ_r over a flux surface. While conditional averaging only detects the coherent structures related to the largest scale, the probe array measures all scales simultaneously and so allows true spatial scale separation.

The results from conditional averaging are then compared with the results from the probe array.

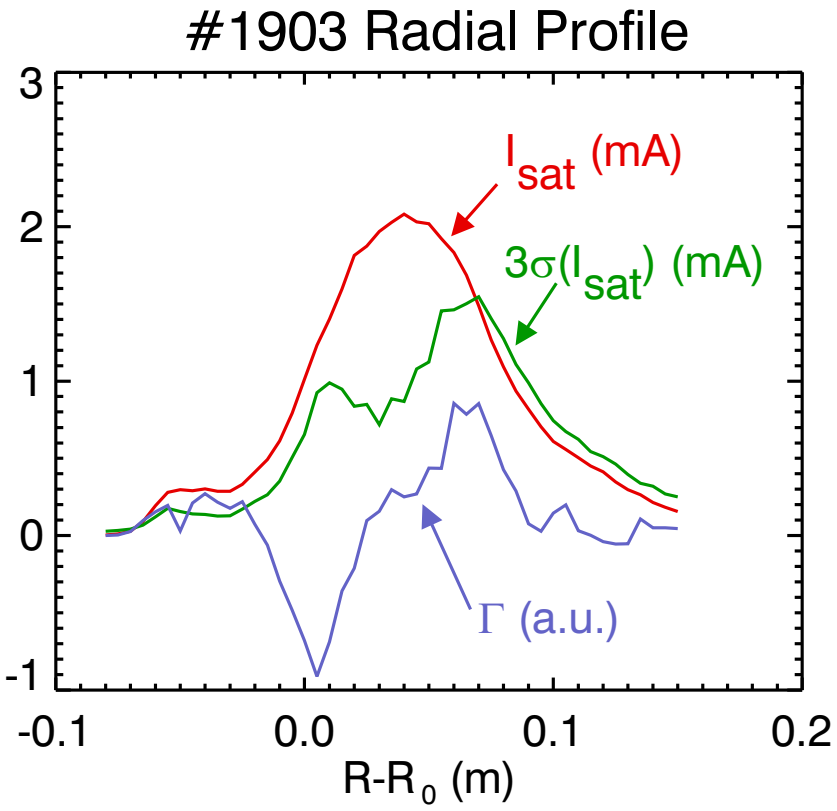

Figure 4.1: Radial profile of ion saturation current, its fluctuation level and the mean turbulent transport. The discharge was in helium with 1.8 kW of ECRH heating. The magnetic field strength was 72 mT and the neutral gas pressure was 2×10^{-5} mbar.

4.1 Radial Variation of the Fluctuations

In this section, a brief overview of fluctuations and transport and their dependence on the radial position is given. Figure 4.1 shows a radial profile of the ion saturation current, its fluctuation amplitude and the turbulent transport for a particularly noise-free ECRH discharge in helium. The measurement was carried out with the transport probe (see Fig. 3.10). The line averaged density is $2.1 \times 10^{18}\,\mathrm{m}^{-3}$ and the electron temperature is 12 eV. The density is centrally peaked and its fluctuations are largest in the region of the density gradient. This is expected because the free energy for the turbulence comes from the gradients.

The turbulent transport is also large in this region. Positive values are

into the outboard direction (to the right), so the transport is always radially outward from the plasma center. While the discharge shown here depicts ideal conditions, all other discharges are similar.

4.2 Conditional Averaging Results

The shape and propagation of the dominant turbulent structures is investigated in this section. The conditional averaging technique (explained in Sec. 2.5.4) yields the spatial structure and propagation of the dominating turbulent events. The structures are classified as follows: single density/potential maxima or minima are called *blobs*, maximum-minimum combinations are called *dipoles* and periodic structures are referred to as *quasi-coherent modes*. The propagation of these structures is due to the background $E \times B$ and diamagnetic flows on the one hand, and the fluctuating $E \times B$ flows generated by the potential fluctuations on the other hand. For the latter, the cross phase between the density and the potential fluctuations is important; a density blob that lies between two potential extrema (cross phase $\pi/2$) will experience a considerable $E \times B$ drift, while a density blob sitting directly on top of a potential blob (cross phase zero) will simply be convected in itself.

Experiments were carried out in hydrogen, helium and argon plasmas with either helicon or microwave (ECRH) heating. ECRH discharges had a magnet current ratio of $R_{v/h} = 0.57$, helicon discharges were done at $R_{v/h} = 0.51$. Results from selected discharges will be presented. In the helicon discharges, the conditional averaging results are as a rule noisier than the results from the ECRH heated plasmas. This may partly be due to rf noise from the helicon source, which at 27 MHz can be picked up very well by the probes. Consequently, only those helicon discharges that have yielded coherent structures at all are considered here. In contrast, all ECRH discharges have yielded very noise-free structures. The results are similar for different discharges in the same gas, so only one result per gas is presented here.

The upper two tips of the transport probe (see Fig. 3.10) were used to measure the floating potential and ion saturation current at different positions in the poloidal plane, while the fixed reference probes were inserted at a neighbouring outer port. The resulting toroidal distance was 60° or about 60 cm between the moving probes and the reference probes. This was due to the availability of access ports. Since the correlation along the magnetic field is 40–100%, the toroidal separation does not invalidate the measurement, where only the separation of the probes perpendicular to the magnetic field is taken into account. The parallel separation, however, may have contributed to the noise in the results from the helicon discharges Parallel correlation and dynamics in TJ-K have been investigated in more detail in [74].

For the helicon discharges, both ion saturation current and floating potential have been used as reference signals. It was found that either reference signal detects similar structures if both reference probes are at the same lo-

cation ($R - R_0 = 10\,\mathrm{cm}$, $z \approx 0\,\mathrm{cm}$), so instead of measuring two quantities at the same place, it is better to measure the same quantity at different locations. This was carried out with the ECRH discharges, where ion saturation current probes #54 and #40 of the poloidal array were used as reference probes (see Fig. 3.12). The probes are at a position of $R - R_0 = 8.2\,\mathrm{cm}$ and $z = \pm 4.2\,\mathrm{cm}$. This setup makes it possible to either find poloidal inhomogeneities in the turbulent structures or else validate one measurement with the other.

In total, four signals were acquired simultaneously for up to one second sampled at 1 or 2 MHz. All data was band-pass filtered at 4–400 kHz for the standard analysis and at 40–800 or 100–800 kHz for the scale separation. For the filtering, a finite impulse response digital filter was used. For each discharge, data was taken at 300–1000 different positions. In helicon discharges, a spatial grid of 5 mm, for the ECRH discharges one of 10 mm was used. Since it takes 40 minutes to take data at 1000 spatial points, in most cases the spatial resolution was reduced to save measurement time. This allows the use of higher magnetic fields, which cannot be sustained for more than 20 minutes due to the heating of the magnetic field coils.

Radial transport is characterised by the radially outward motion of positive density fluctuations or the radially inward motion of negative density fluctuations. The radial direction is defined by the gradient of the background density or potential. In the helicon discharges, where these quantities are not available, [1] the calculated flux surfaces are used as the plasma location. Since the radial displacement of the turbulent structures is of the same order of magnitude as the deviation of the equi-density contours from the calculated flux surfaces, no meaningful statement can be made about radial propagation in helicon discharges. In order to trace the motion of the structures which change their shape as they propagate, the center of mass of the density extrema is computed. Its movement over time is used to compute the propagation speed v. Together with the structure size l, the characteristic frequency $f = v/2l$ is calculated. For non-periodic blobs, the full width at half minimum or maximum (FWHM) is taken as the structure size.

In the following, the results from conditional averaging are presented. Since the ion mass has the strongest impact on the drift scale ρ_s and hence the turbulent structure size, the results are ordered by gas, from large ρ_s (argon) to small ρ_s (hydrogen).

[1] Since the variation between discharges is not negligible, the measurement has to be set up to acquire both fluctuations and background quantities simultaneously. This was only done for the ECRH discharges.

4.2.1 Conditional Averaging Results for Argon

In Figs. 4.2 and 4.3, respectively, the spatio-temporal structure of the conditionally averaged data for an ECRH and a helicon discharge in argon are shown. In all plots, the magnetic field points into the plane. In the ECRH discharge, a quasi-coherent $m = 2$ mode is visible that extends radially over the whole density gradient length, as can be seen from the overlayed ion saturation contours. The structure size of about 8 cm is more or less limited by the plasma size. It is more than three times as large as the drift scale $\rho_s = 2.3\,\mathrm{cm}$. The potential structures (bottom row) show the same behaviour. In order to help determining the phase difference between potential and density, a black potential contour at half the minimum and maximum values is plotted into the density plot and vice versa. It can be seen that the structures are not exactly identical, which gives rise to $E \times B$ drifts that alter the shape of the density structures. For example, the potential maximum generates a counter-clockwise flow along its edge. The FWHM potential contour can be regarded as the path of this flow. This flow is e.g. responsible for the accumulation of density below the potential maximum at $\tau = 50\mu$s.

In order to investigate the propagation of the density structure in more detail, the motion of the center of mass of the top halves of the density extrema has been traced in Fig. 4.4 (left). The motion of the mode is in the electron diamagnetic direction with $v = 900\,\mathrm{m/s}$ and the minimum can be seen to propagate very slightly radially outwards, while the maximum goes radially inwards with respect to the density profile. This is consistent with the observation that there is a very small cross phase between density an potential and only very little flow is generated that selectively transports density maxima into one radial direction and minima into the other.

The quasi-coherent mode is rather stable, the correlation time exceeds the time window of 256 μs. The propagation speed of 900 m/s, divided by its wavelength of about 25 cm results in a frequency of 4 kHz, which is prominently visible in the power spectra of ion saturation current and floating potential (Fig. 4.5). Power spectra and cross phase are calculated from the data time series at $R - R_0 = 0.09\,\mathrm{m}$ and $z = 0.0\,\mathrm{m}$. The cross phase between ion saturation current and floating potential at 4 kHz is zero, consistent with the findings form conditional averaging. The measurement of the cross phase is valid, because the spatial separation of 5 mm between the two probes is negligible compared to the structure size.

The density structures of the helicon discharge (Fig. 4.3) are smaller in amplitude than the ones of the ECRH discharge by an order of magnitude, even if it is taken into account that the overall background density is one fourth that of the ECRH discharge. The single positive density blob is irreg-

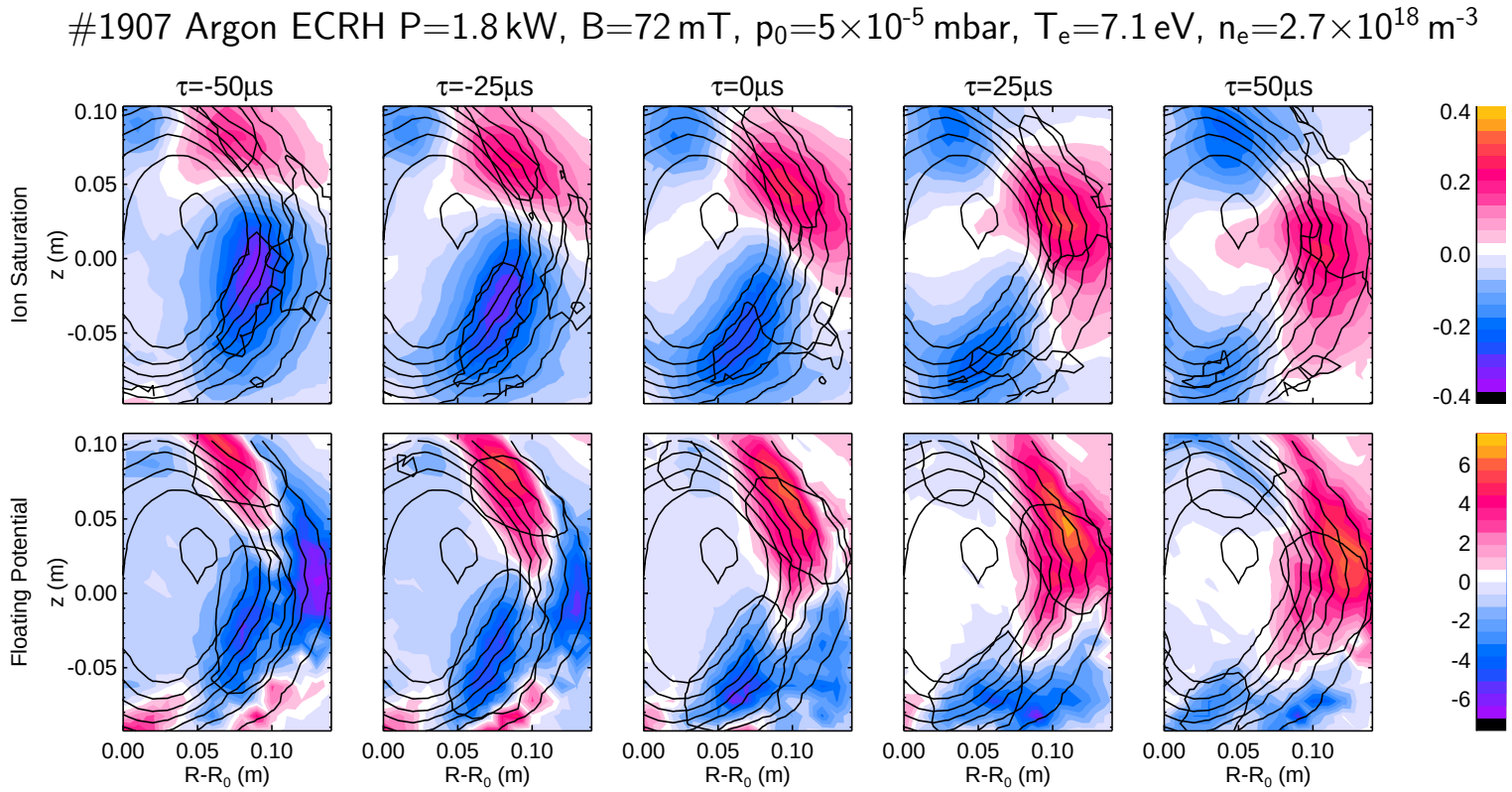

Figure 4.2: Time evolution of the conditionally averaged ion saturation current (top) and floating potential (bottom) structures. The units are mA and V, respectively. The magnetic field points into the plane. Overlayed are the background ion saturation current contours. Also a potential contour is plotted into the saturation current plot and vice-versa. The condition was set at minus two standard deviations on a rising flank.

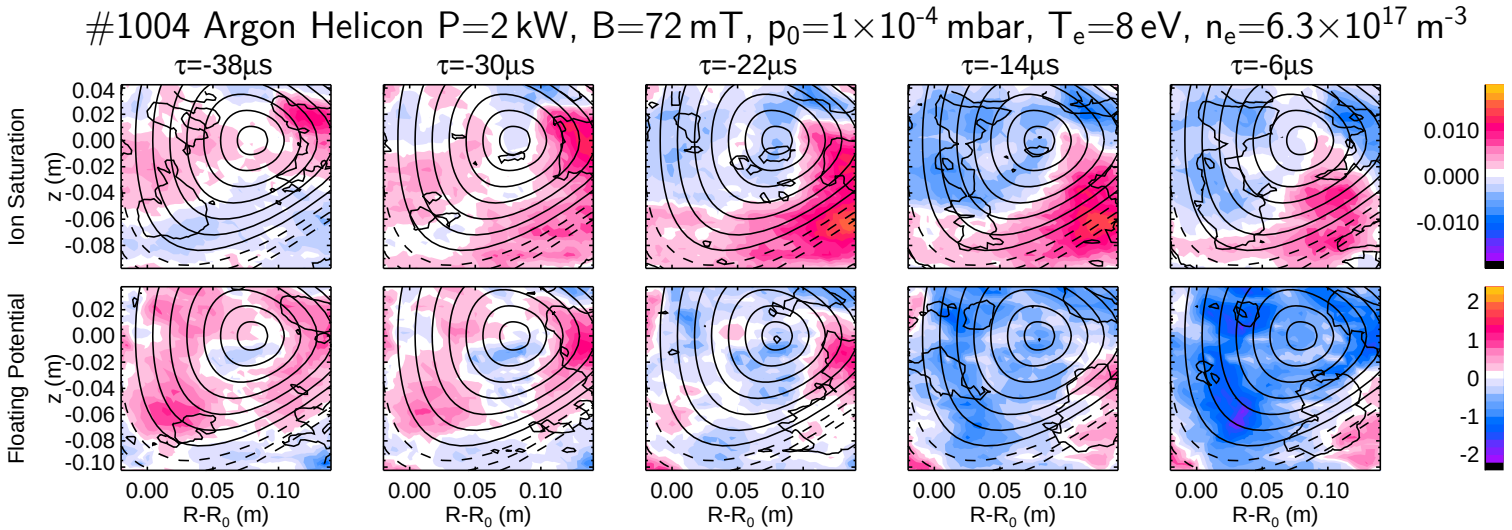

Figure 4.3: Time evolution of the conditionally averaged ion saturation current (top) and floating potential (bottom) structures. The units are mA and V, respectively. The magnetic field points into the plane. Overlayed are the calculated flux surfaces for $R_{v/h} = 0.51$. Also a potential contour is plotted into the saturation current plot and vice-versa. The condition was set at minus two standard deviations on a rising flank.

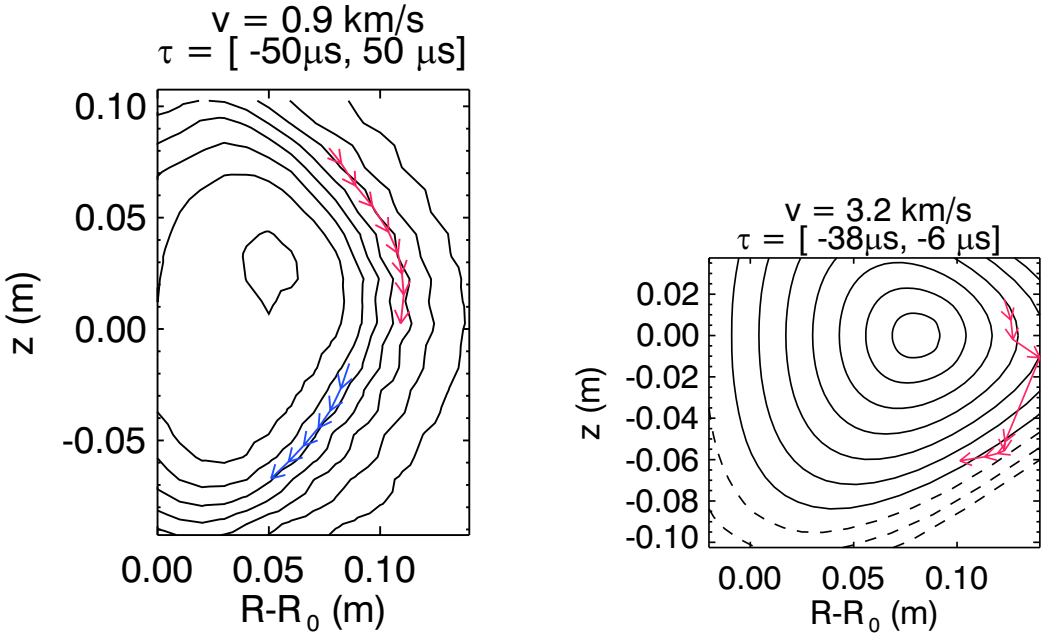

Figure 4.4: Trajectories of the density maxima (red) and minima (blue) for the time interval shown in the previous figures. The propagation speed v is computed from the trace of the maximum. The ECRH argon discharge shown on the left and the helicon discharge is shown on the right.

ular in shape. There is no corresponding potential structure. The correlation time of about 80 μs is much shorter then the correlation time for the ECRH discharge. The maximum correlation between data and reference signals is only 50%, compared to 100% for the ECRH discharge.

Figure 4.4 (right) shows the propagation of the 10 cm blob, which is four times the size of the drift scale $\rho_s = 2.5$ cm. The determination of the center of mass is disturbed by the noise level, but a propagation in the electron diamagnetic drift direction with a radially outward excursion is observable. With its propagation speed of 3.2 km/s and assumed wavelength of two times its poloidal FWHM size, a characteristic frequency of about 16 kHz is found. The floating potential spectrum in Fig. 4.5 shows a maximum near this frequency, while the ion saturation current has two maxima a few kHz above and below this value. This can be explained by the irregular, changing shape of the blob, which for example doubles its size between $\tau = -38\,\mu$s and $\tau = -22\,\mu$s.

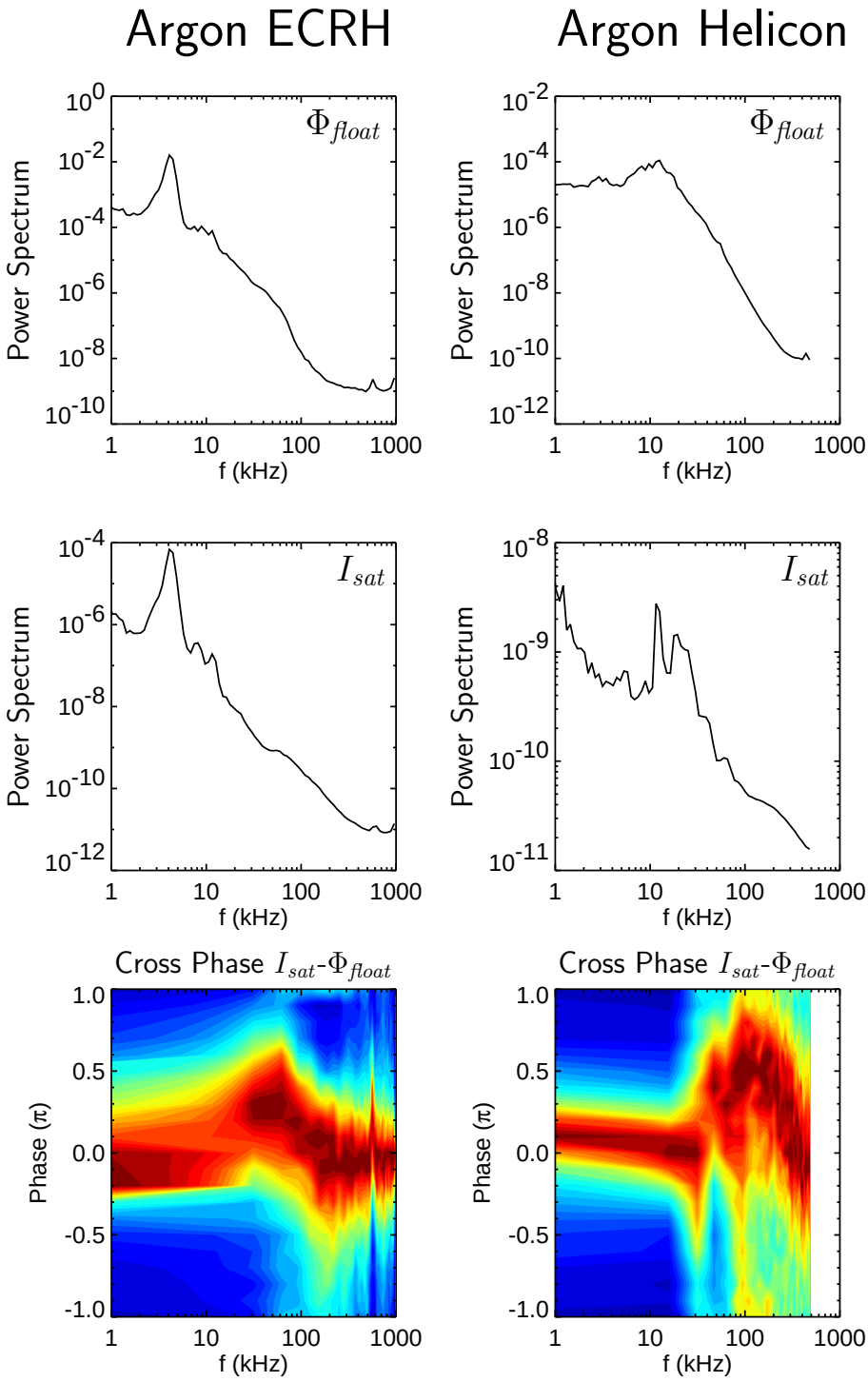

Figure 4.5: Spectra of floating potential (top) and ion saturation current (middle) fluctuations. The raw frequency resolved phase between saturation current and potential is given at the bottom. A phase correction that depends on the structure size has to be applied. The left column belongs to the argon ECRH discharge plotted in Fig. 4.2, the right one is for the argon helicon discharge from Fig. 4.3.

4.2.2 Conditional Averaging Results for Helium

The spatial and temporal structure of turbulent events in helium plasmas is shown in Figs. 4.6–4.8. The ECRH discharge has a slightly higher temperature (9.3 eV compared to 7.1 eV) than the ECRH discharge in argon. The magnetic field is 89 mT, compared to 72 mT, resulting in a drift scale of $\rho_s = 0.7$ cm, less than one third the value for argon. Consequently, the structure size of 5 cm observed in Fig. 4.6 is smaller than in argon, albeit not by the same factor as ρ_s. However, the structure size in argon is limited by the plasma size. The structure is a dipole in density and potential with a cross phase near zero. The flow generated by the potential minimum only serves the propagation in the electron diamagnetic direction (see Sec. 2.3.3). The elongated potential maximum at $\tau = -40\,\mu$s on the other hand generates an counter-clockwise flow that is best imagined as following the potential contour that is plotted into the ion saturation current plots in Fig. 4.6. This has the effect of shearing the elongated density maximum into the round shape seen at $\tau = 20\,\mu$s. The maximum stays on an equi-density line of the strongly outwards bulging background density profile, while the minimum moves slightly radially inwards (Fig. 4.9), resulting in a net outward transport.

A spatial scale separation is attempted by filtering out the low-frequency part of the signal, which is thought to be associated mainly with the large spatial scales. Figure 4.7 shows the turbulence structure of the same discharge, but with a band-pass filter of 40–800 kHz applied to the data prior to conditional averaging. The detected structure is a density maximum followed by a weak minimum. With a size of 2 cm it is considerably smaller than the structure filtered with the low band-pass at 4–400 kHz. The latter structure vanishes after a lifetime of about 30 μs, compared to $> 150\,\mu$s for the former. The radial size is 5 cm. The potential structure consists of a string of three alternating extrema that are generated in the upper part and propagate downwards and radially outwards. Up to $\tau = 0\,\mu$s, the density maximum moves radially outward at the edge of the potential maximum, then it moves inward (Fig. 4.9), while the potential maximum moves outward. The density blob's speed of 2.3 km/s is two times as high as the speed of the large structure.

The characteristic frequencies associated with the density structures are 11 for the large and 55 kHz for the small ones. The former barely shows up in the power spectra as a small dip present in Fig. 4.10, while the latter does not. This is a consequence of the fact that turbulent structures exist at all scales and no scale particularly dominates the dynamics. This is in contrast to the results from the argon ECRH discharge, where a quasi-coherent mode

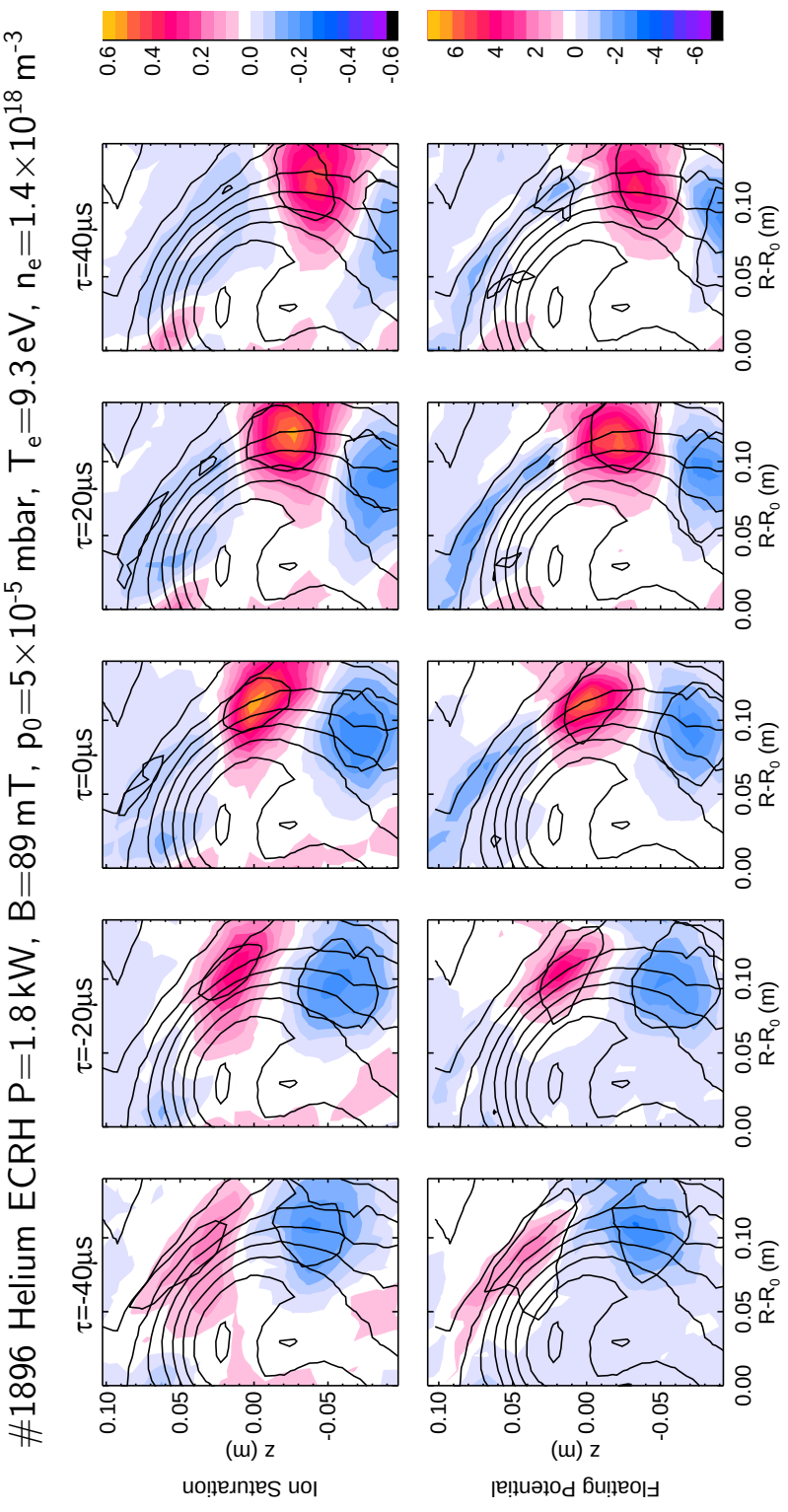

Figure 4.6: Time evolution of the conditionally averaged ion saturation current (top) and floating potential (bottom) structures. The units are mA and V, respectively. The magnetic field points into the plane. Overlayed are the background ion saturation current contours. Also a potential contour is plotted into the saturation current plot and vice-versa. The condition was set at two standard deviations on a rising flank.

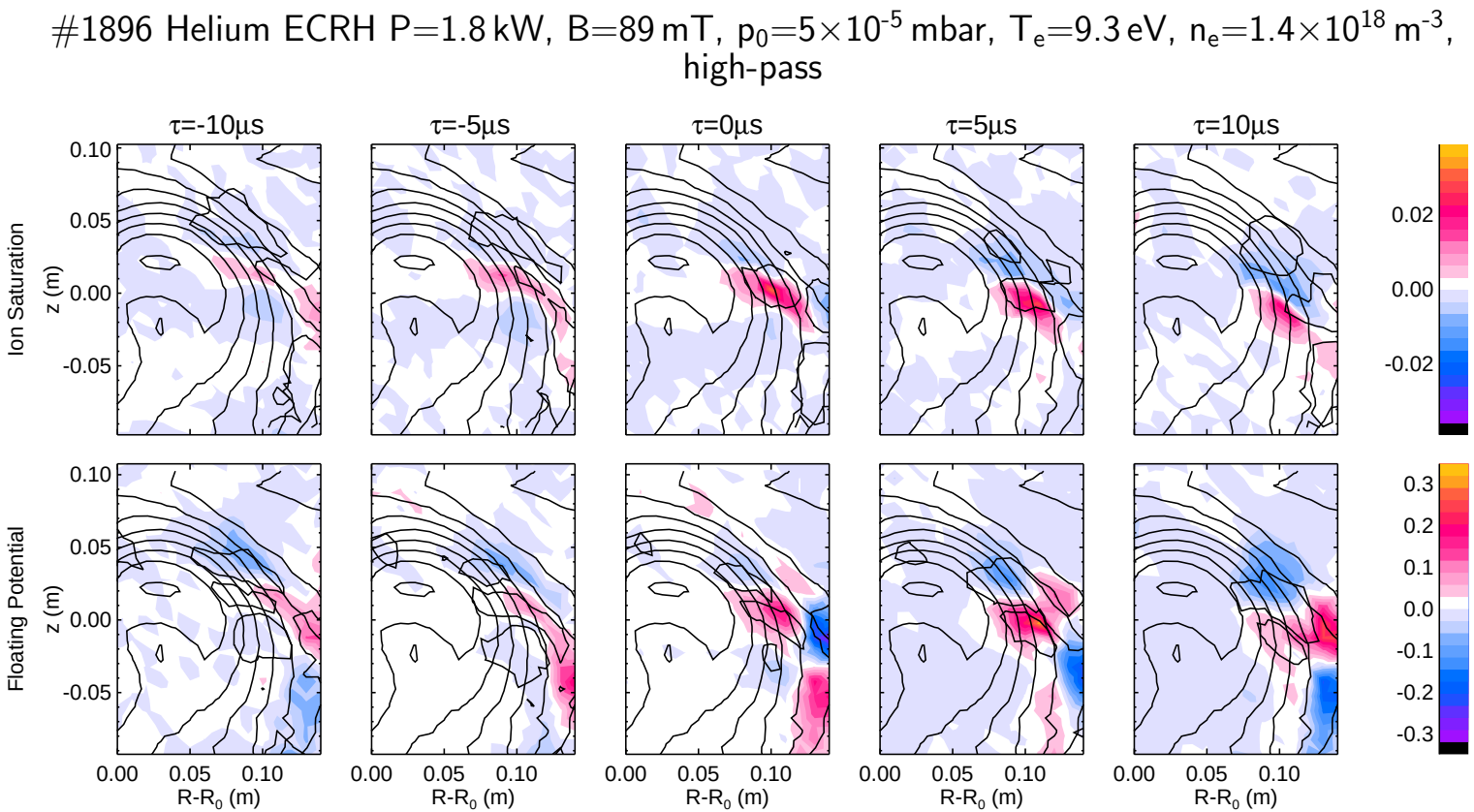

Figure 4.7: Time evolution of the conditionally averaged ion saturation current (top) and floating potential (bottom) structures. The units are mA and V, respectively. The magnetic field points into the plane. Overlayed are the background ion saturation current contours. Also a potential contour is plotted into the saturation current plot and vice-versa. The condition was set at two standard deviations on a rising flank. In contrast to the previous figure, a band-pass filter of 40–800 kHz has been applied to the data prior to averaging. The sampling frequency is 2 MHz.

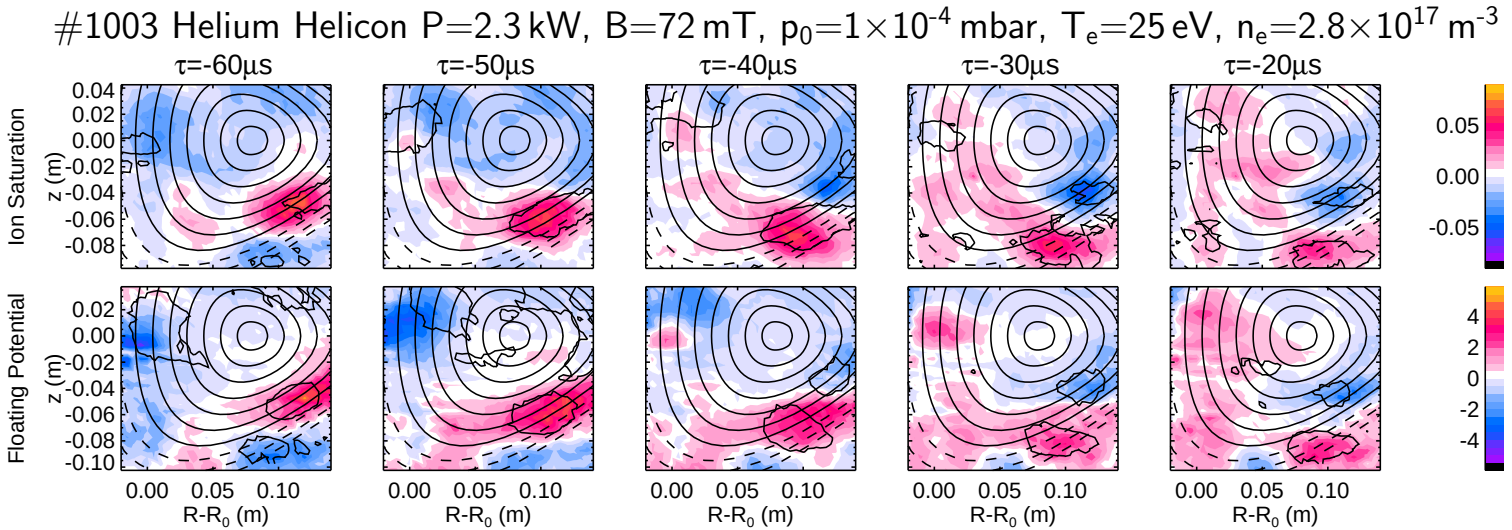

Figure 4.8: Time evolution of the conditionally averaged ion saturation current (top) and floating potential (bottom) structures. The units are mA and V, respectively. The magnetic field points into the plane. Overlayed are the calculated flux surfaces for $R_{v/h} = 0.51$. Also a potential contour is plotted into the saturation current plot and vice-versa. The condition was set at two standard deviations on a rising flank.

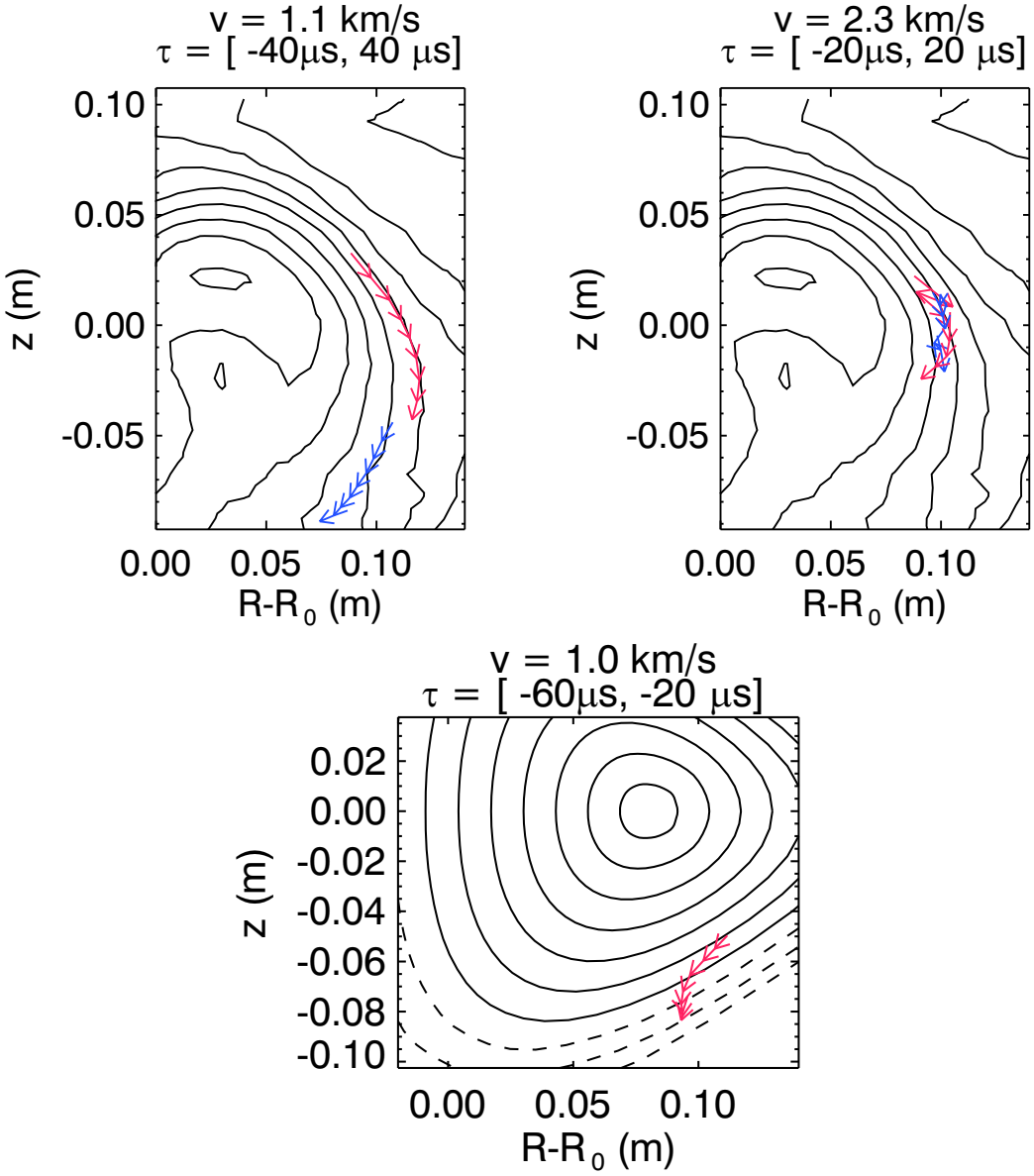

Figure 4.9: Trajectories of the density maxima (red) and minima (blue) for the time interval shown in the previous figures. The propagation speed v is computed from the trace of the maximum. The propagation of structures in the helium ECRH discharge is shown in the top row. In the analysis, a distinction is made between data filtered with a low band-pass (top left) and a high band-pass (top right). The blob propagation for the helicon discharge in helium is shown in the bottom row.

dominates the spectrum.

The factor of about 100 in the power spectra at the two frequencies corresponds nicely to the difference of about factor 10 in the amplitudes of the small and large structures (0.6 mA vs. 0.04 mA).

The small cross phase observed above is also evident in Fig. 4.10. For the small blob with size of 2 cm and corresponding wave length of 4 cm, the 5 mm separation of the probes used for measuring the cross phase results in a phase shift of $2\pi \cdot 5\,\mathrm{mm}/4\,\mathrm{cm} = \pi/4$. When this is subtracted from the value of the cross phase at the blob's characteristic frequency of 55 kHz, the phase is zero again.

The helicon discharge is much hotter (25 eV) and less dense ($2.8 \times 10^{17}\,\mathrm{m}^{-3}$) than either its argon or its ECHR counterpart, which results in a relatively large drift scale of $\rho_s = 1.4\,\mathrm{cm}$. Figure. 4.8 shows the motion of a single positive density blob with a size of 5 cm. Its lifetime of 70 μs lies entirely before the center of the conditional averaging time window, which is surprising and would point to a short parallel wavelength. This singular observation should be investigated further. Similar to the helicon discharge in argon, the parallel correlation only reached 40%, compared to 75% for the corresponding ECRH discharge, so the structure observed here has only a small signal-to-noise ratio. Nevertheless, the density blob is accompanied by a positive potential blob that slightly lags behind at $\tau = -40\,\mu\mathrm{s}$, allowing the flow generated by it to move the density blob radially outward, which can be seen in Fig. 4.9 (bottom). The poloidal propagation speed of 1 km/s is the same as for the ECRH discharges in helium and argon, in the direction of the electron diamagnetic drift. The band-pass filtering at higher frequencies did not yield another set of blobs.

The power spectrum of the ion saturation current shows a broad peak around the characteristic frequency of 10 kHz in Fig. 4.10. The width of the peak reflects the irregular shape of the blob.

The cross phase of about zero is not accurately reproduced in the cross phase plot, even after correcting for the probe separation. Due to the low quality of the data, it does not, however, contradict the above findings.

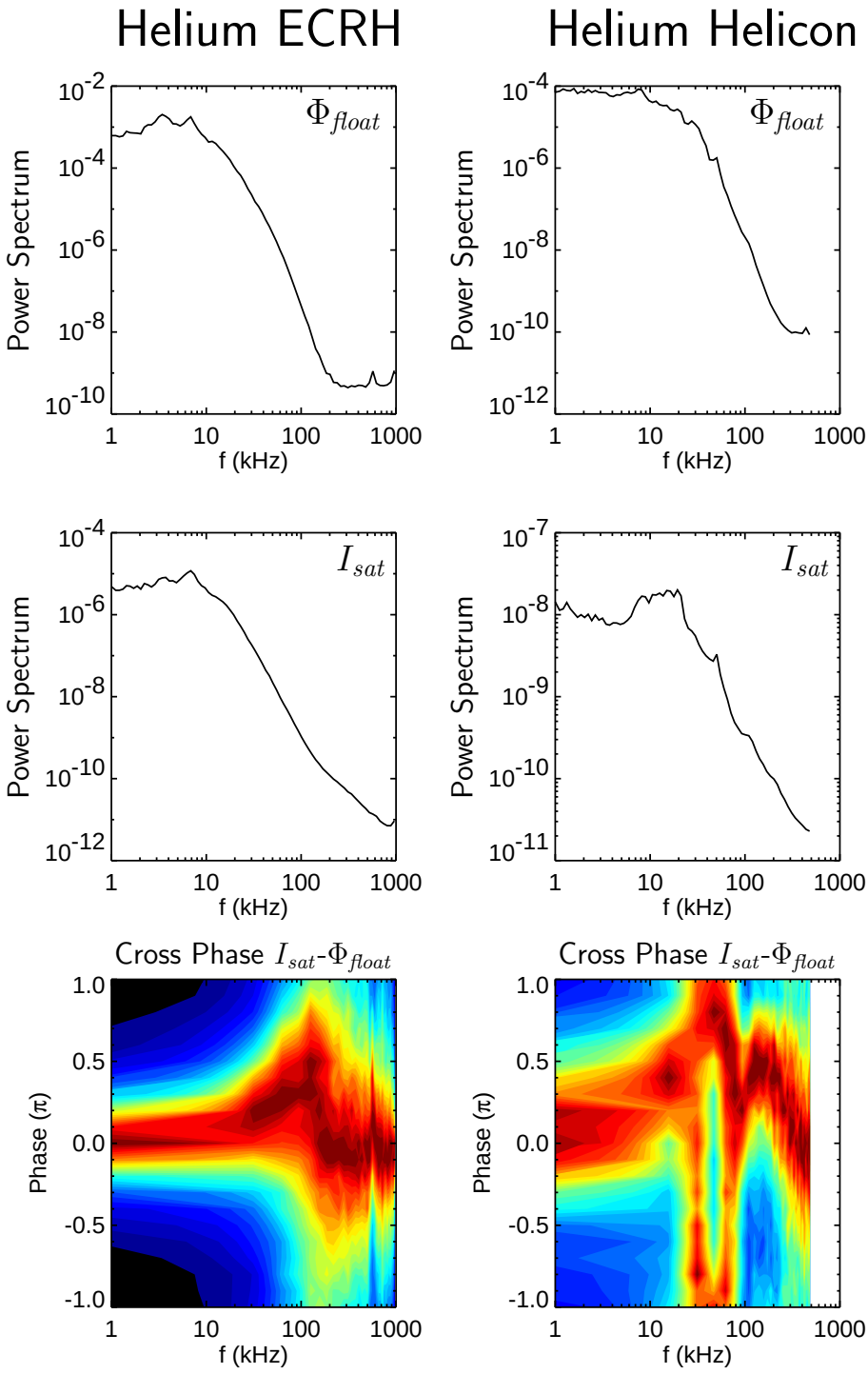

Figure 4.10: Spectra of floating potential (top) and ion saturation current (middle) fluctuations. The raw frequency resolved phase between saturation current and potential is given at the bottom. A phase correction that depends on the structure size has to be applied. The left column belongs to the helium ECRH discharge plotted in Figs. 4.6 and 4.7, the right one is for the helium helicon discharge from Fig. 4.8.

4.2.3 Conditional Averaging Results for Hydrogen

At the small end of the ρ_s scale lie the hydrogen discharges. The evolution of the turbulent structures is shown in Figs. 4.11–4.13. The ECRH discharge with a drift scale of $\rho_s = 4\,\mathrm{mm}$ displays a quasi-coherent mode with a wavelength of 7 cm and a velocity of 2.3 km/s (Fig. 4.11). A similar mode is seen in the data filtered with a band-pass of 40–800 kHz (Fig. 4.12). It has a wavelength of 6 cm and a propagation velocity of 2.8 km/s. Of the resulting characteristic frequencies of 33 and 47 kHz, respectively, only the 33 kHz show up in the power spectra (Fig. 4.16). The life time of the modes lies between 60 and 70 μs.

The cross phase between density and potential is large ($\sim \pi/4$). This is evident e.g. in the ion saturation current plot for $\tau = 10\,\mu\mathrm{s}$ in Fig. 4.11, where the black contour of the potential minimum is located between the two biggest density extrema. The flow generated by the potential minimum runs clockwise along the potential contour, convecting the density maximum outward and the density minimum inward. This is also seen in the trajectory plot in Fig. 4.15. Practically the same argument can be made for the high band-pass filtered structures shown in Fig. 4.12.

The velocities of the radial flows as computed from the poloidal electric field are 333 and 200 m/s. In Fig. 4.15, this translates to a respective radial displacement of 8 and 2.5 mm over the whole time window. The actual displacement is of the same order of magnitude.

When a band-pass with an even higher frequency of 100–800 kHz is used, a quasi-coherent mode with a wavelength of 2 cm and a frequency of 125 kHz is detected ($v = 2.5\,\mathrm{km/s}$). Figure 4.14 shows the radially elongated structures. The amplitude of the mode is an order of magnitude lower then the amplitude of the 47 kHz mode, corresponding to the power spectrum. The mode is at the spatial resolution limit of the probes, but a cross phase in the order $\pi/2$ is observed. The phase correction for the wavelengths of 7, 6 and 2 cm are 0.14, 0.17 and 0.5π, respectively. Together with the raw cross phase from Fig. 4.16, the observed result from above is confirmed.

The correlation along the magnetic field is 50%, hinting a shorter parallel structure size than for ECRH discharges in argon or helium.

The helicon discharge in hydrogen has a relatively high electron temperature of 24 eV, which results in a drift scale of $\rho_s = 6.2\,\mathrm{mm}$, larger than the ECRH counterpart and similar to the ECRH discharge in helium. Consequently, the dipole structure seen in Fig. 4.13 with size of 5 cm is larger than the structure size in the ECRH hydrogen discharge. The potential structure is smeared out over the whole plasma cross section. Its irregularity makes it meaningless to assign a cross phase to this structure.

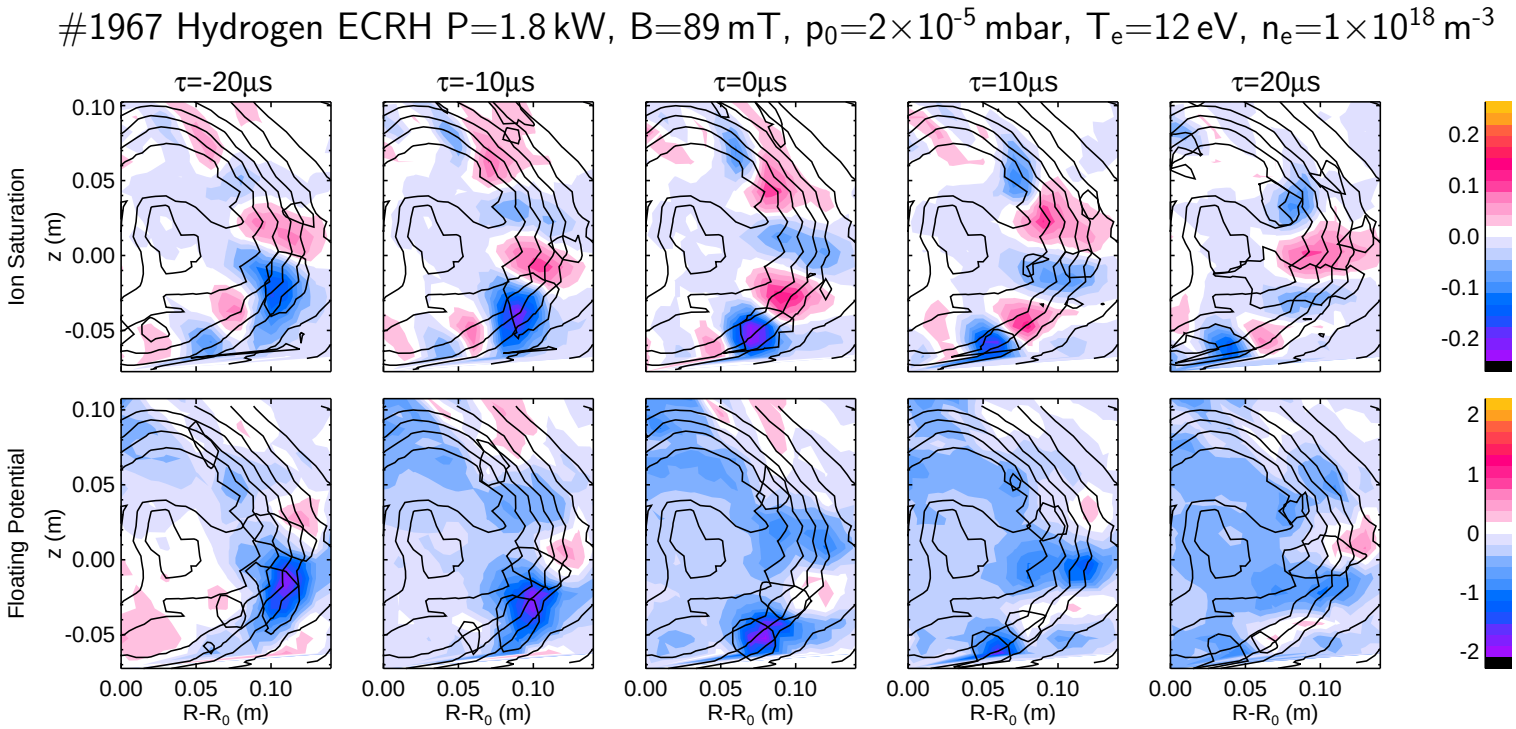

Figure 4.11: Time evolution of the conditionally averaged ion saturation current (top) and floating potential (bottom) structures. The units are mA and V, respectively. The magnetic field points into the plane. Overlayed are the background ion saturation current contours. Also a potential contour is plotted into the saturation current plot and vice-versa. The condition was set at minus two standard deviations on a rising flank.

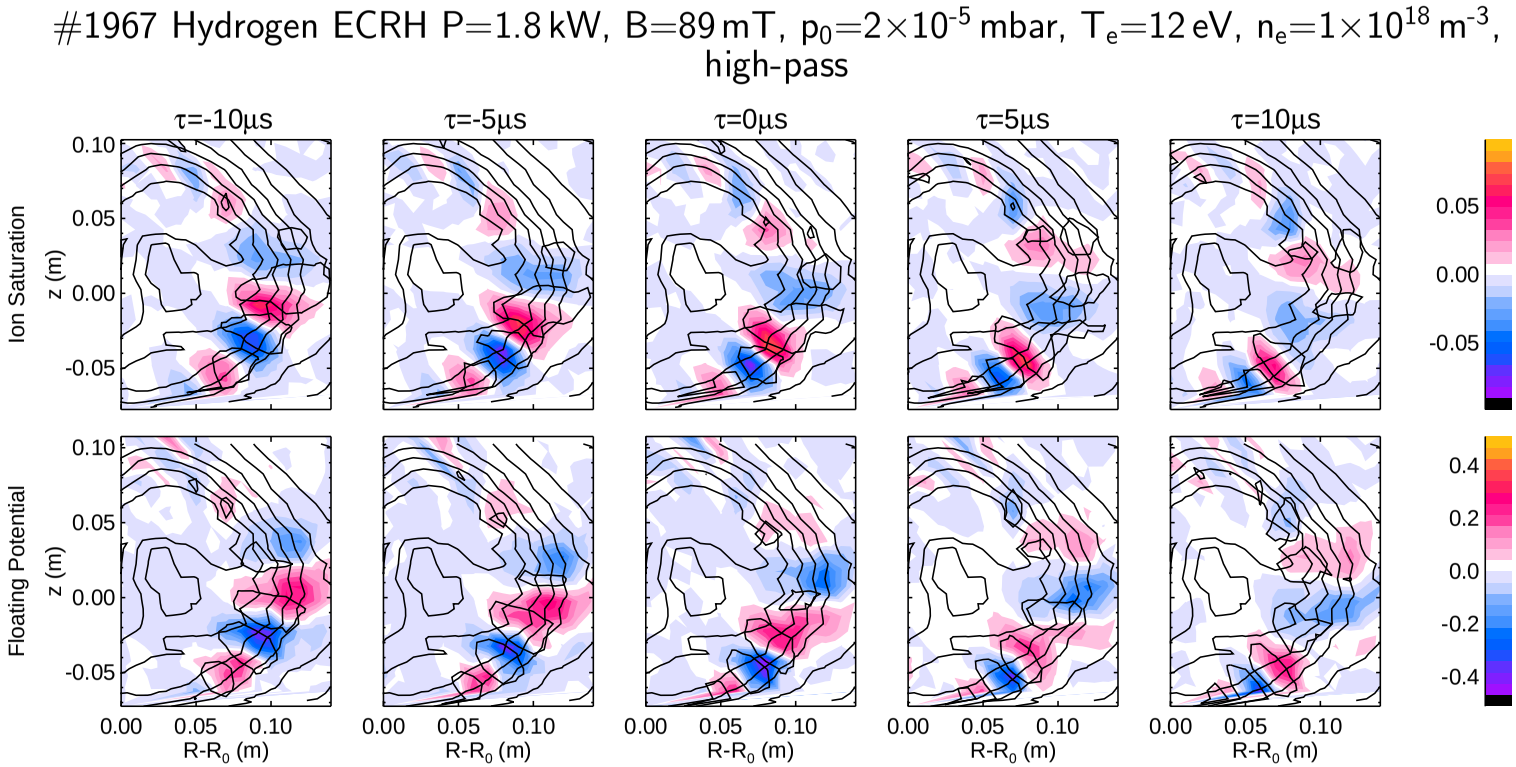

Figure 4.12: Time evolution of the conditionally averaged ion saturation current (top) and floating potential (bottom) structures. The units are mA and V, respectively. The magnetic field points into the plane. Overlayed are the background ion saturation current contours. Also a potential contour is plotted into the saturation current plot and vice-versa. The condition was set at minus two standard deviations on a rising flank. In contrast to the previous figure, a band-pass filter of 40–800 kHz has been applied to the data prior to averaging. The sampling frequency is 2 MHz.

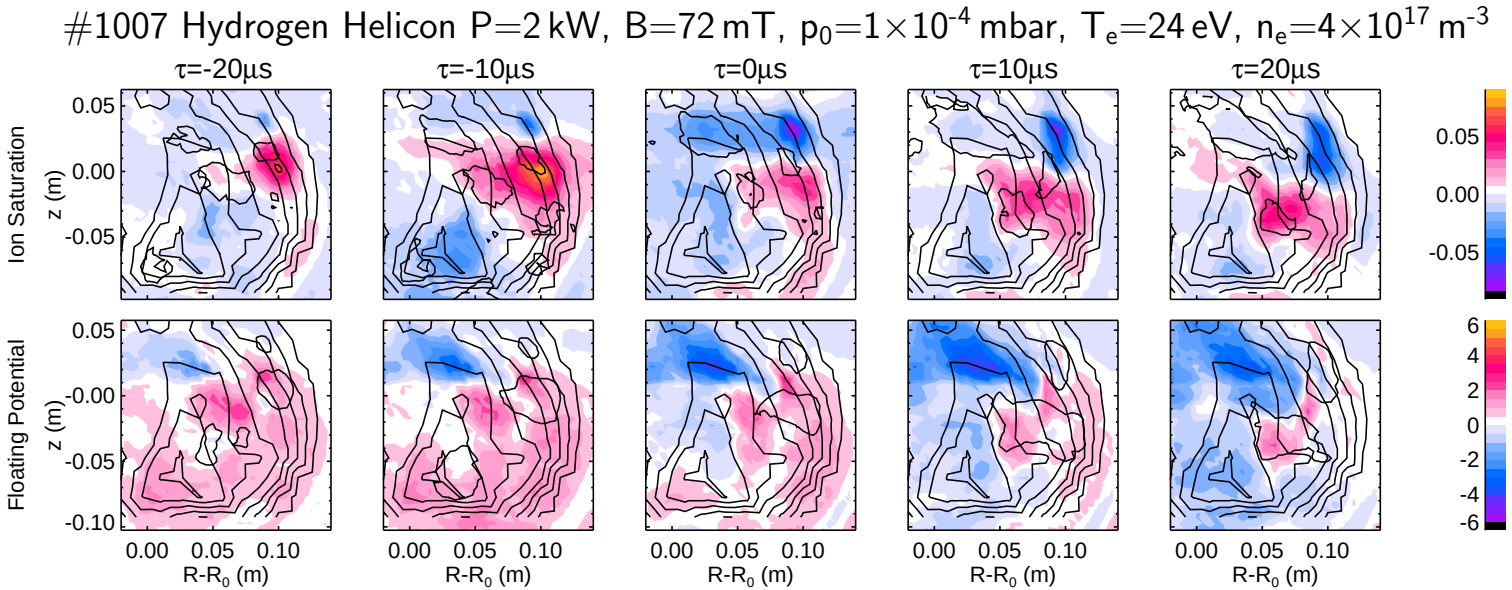

Figure 4.13: Time evolution of the conditionally averaged ion saturation current (top) and floating potential (bottom) structures. The units are mA and V, respectively. The magnetic field points into the plane. Overlayed are the background ion saturation current contours. Also a potential contour is plotted into the saturation current plot and vice-versa. The condition was set at minus two standard deviations on a rising flank. The ion saturation current contours were added from a different discharge with the same discharge parameters.

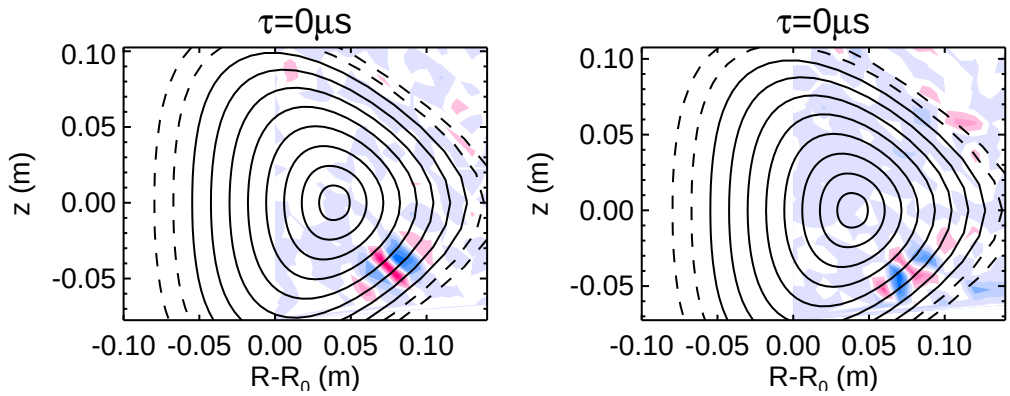

Figure 4.14: Ion saturation current (left) and floating potential (right) for the band-pass filtered data at 100–800 kHz of the ECRH hydrogen discharge. The amplitudes are 5 μA and 10 mV, respectively. The radial size is 4 cm, the poloidal wavelength is 2 cm

The strong inward propagation of the density maximum is shown in Fig. 4.15 (bottom). It is a consequence of the vertically oriented electric field going from the central potential maximum to the minimum in the upper left corner at $\tau = 10\,\mu$s. The propagation speed of 1.5 km/s is slower than the speed of the hydrogen ECRH discharge. The characteristic frequency of 15 kHz for the density structure is not apparent in the spectrum in Fig. 4.16.

The parallel correlation was 60%, which is somewhat higher than for the corresponding ECRH discharge.

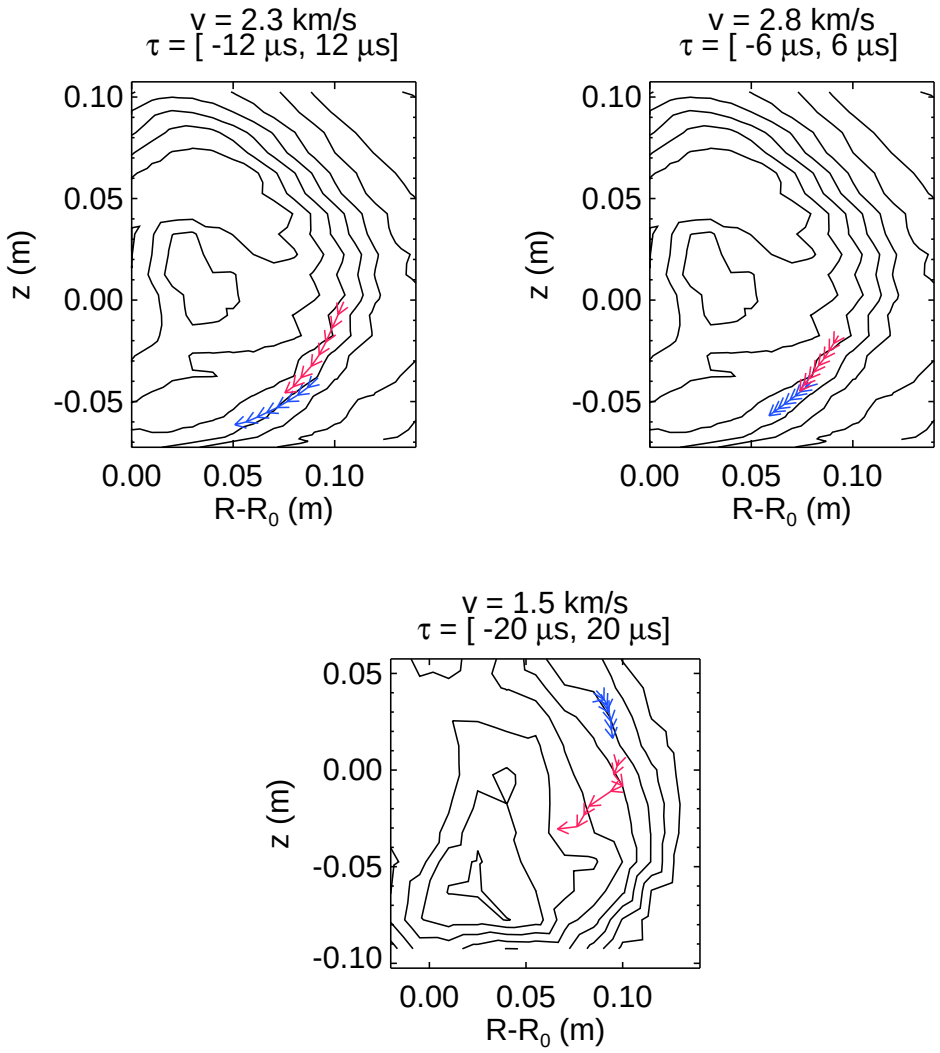

Figure 4.15: Trajectories of the density maxima (red) and minima (blue) for the time interval shown in the previous figures. The propagation speed v is computed from the trace of the maximum. The propagation of structures in the hydrogen ECRH discharges is shown in the top row. In the analysis, a distinction is made between data filtered with a low band-pass (top left) and a high band-pass (top right). The blob propagation for the helicon discharge in hydrogen is shown in the bottom row.

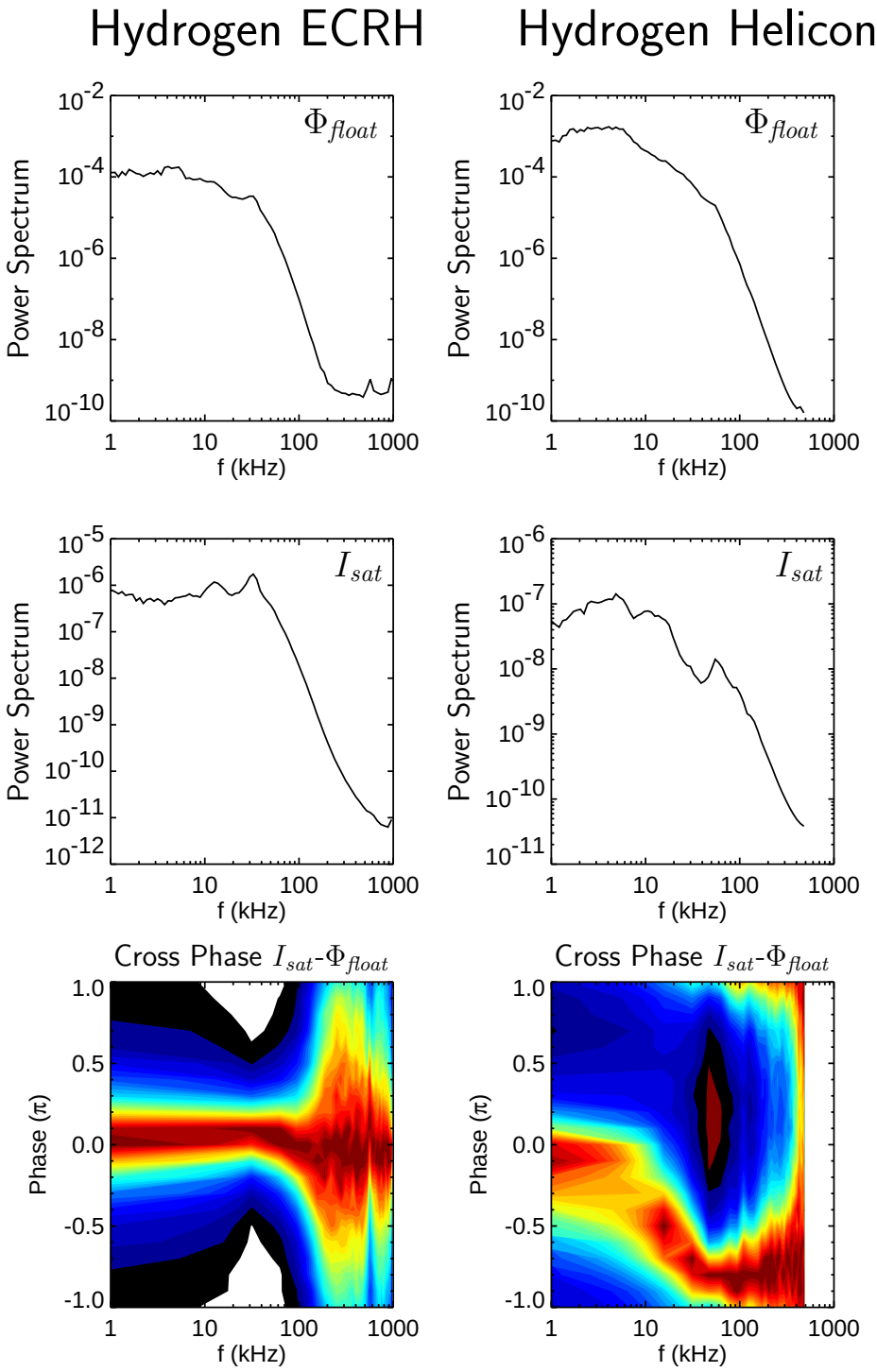

Figure 4.16: Spectra of floating potential (top) and ion saturation current (middle) fluctuations. The raw frequency resolved phase between saturation current and potential is given at the bottom. A phase correction that depends on the structure size has to be applied. The left column belongs to the hydrogen ECRH discharge plotted in Figs. 4.11, 4.12 and 4.14, the right one is for the hydrogen helicon discharge from Fig. 4.13.

4.2.4 Conditional Averaging Summary

The conditional averaging method was used to detect coherent structures in the turbulent plasmas of helicon and ECRH discharges in hydrogen, helium and argon. The ECRH discharges yielded smooth averaged structures, while the helicon discharges were much noisier, which is mainly attributed to rf pickup from the heating system.

The turbulent spectra of ion saturation current and floating potential all showed the most fluctuation power at small frequencies (1 kHz) which then fell towards the high end of the spectrum at 1 MHz. Sometimes, large modes were present on top of this behaviour.

Nevertheless, all discharge types yielded coherent structures that were classified as (single) blobs, dipoles or quasi-coherent modes. Quasi-coherent modes can dominate the power spectrum (argon ECRH), but this is not necessary, as the ECRH discharge in hydrogen shows, which has quasi-coherent modes at several scales, none of which results in a pronounced peak in the power spectrum. The strength of the quasi-coherent mode in the argon ECRH discharge can be explained by the presence of a 2/7 rational flux surface at that radial position, which gives rise to a mode with toroidal mode number seven and poloidal mode number two. While the same rational surface is present in all ECHR discharges, the growth rate of the mode seems to be too small for the other gases.

All structures move in the direction of the electron diamagnetic drift, whose magnitude is several kilometres per second. A radial propagation takes place when the potential structures generate radial flows a positions where density structures are present. This necessitates a non-zero (poloidal) cross phase between the poloidally propagating density and potential structures. This cross phase has been found to be zero or near zero for large and intermediate scales. At small scales, near the spatial resolution limit, the cross phases can be significantly larger than zero. In the ECRH discharges, the radial velocity was small compared to the poloidal velocity. In the helicon discharges, the radial velocity was similar in magnitude to the poloidal velocity.

A problem with the poloidal velocities is that they are similar in magnitude to the clockwise diamagnetic drift, but this drift is comparable to the counter-clockwise $E \times B$ drift computed from the background floating potential. In the first three discharges in Tab. 4.1, the observed poloidal propagation speed of the structures is into the opposite direction as the sum of diamagnetic and $E \times B$ drift. Preliminary studies of the plasma potential with emissive probes [75], however, suggest that the actual radial electric field is much smaller than the field computed from the floating potential.

Gas	Heating	A_i	ρ_s (cm)	λ (cm)	v_θ (km/s)	$v_{dia} + v_{E\times B}$ (km/s)	v_r	f (kHz)	Cross phase	Type
Ar	ECRH	40	2.3	16	3.2	-1	-	4	0	m
Ar	Helicon	40	2.5	20	0.9	-4	+	16	0	b
He	ECRH	4	0.7	10/4	1.1/2.3	-1	+/-	11/55	0	d
He	Helicon	4	1.4	10	1.0	3	+	10	0	b
H	ECRH	1	0.4	7/6/2	2.3/2.8/2.5	3	+	33/47/125	$\pi/4$	m
H	Helicon	1	0.6	10	1.5	3	-	15	—	d

Table 4.1: Overview of the results from conditional averaging.

This does not invalidate the previous results, because it is nevertheless expected that the flows computed from the fluctuating floating potential have the same general shape as the ones actually generated by the plasma potential and only differ in magnitude. It has been shown with the hydrogen ECRH discharge that the difference between observed radial flow velocities and electric field is less than one order of magnitude.

The structure sizes are expected to behave like the drift scale ρ_s. As can be seen in Tab. 4.1, this is indeed the case. All sizes are given as wavelengths λ. The characteristic frequencies $f = v/\lambda$ are determined by the wavelength and the propagation speed v.

The frequency spectra presented in the previous sections are all typical of turbulence [76]. The maximum at small frequencies falls off toward higher frequencies. On some spectra, modes are superimposed on the turbulent background.

In order to attempt a scale separation, the data was band-pass filtered with 40–800 kHz or 100–800 kHz. The results from different filters are separated in the table by a slash. This scale separation was successful for ECRH discharges in hydrogen and helium. The column named "Type" takes 'b' for blob, 'd' for dipole and 'm' for quasi-coherent mode. Outward radial propagation is denoted by '+', inward propagation by '-'.

In the ECRH discharges with helium and hydrogen, it was possible to detect small-scale, high-frequency structures by filtering out the low-frequency part of the spectrum prior to analysing the data. The amplitudes of these fluctuations were considerably smaller than for the low-frequency fluctuations. This is in agreement with the power spectrum, which also falls off towards high frequencies.

The findings presented here have a zero cross phase (drift wave behaviour) at large and intermediate spatial scales, while at small scales, phases can become large. The ECRH discharge in hydrogen is an exception. It has a non-zero phase ($\sim \pi/4$) also at intermediate scales. The zero cross phase at large scales is at variance with earlier results from helicon discharges in

helium [77], where a cross phase of $\pi/2$ was found for the large structures. Those experiments were conducted with an extremely outward shifted plasma ($R_{v/h} = 0.44$), where major rational flux surfaces may have been inside the plasma and even inner flux surfaces may have had contact with installations inside the vacuum vessel. Results from W7-AS [78, 20] also find a cross phase of $\pi/2$, but outside the plasma confinement region in the scrape-off layer. It is conceivable that the cross phase of $\pi/2$ is a result of the open magnetic field lines that need not be true for the confined plasma. Finally, cross phases up to $\pi/3$ have been found in the TJ-I tokamak [54].

The cross phase determines the radial transport that is caused by the fluctuations in density and potential [Eq. (2.18)]. The radial propagation of the structures that were detected by conditional averaging can be explained in terms of the flows generated by the turbulent potential structures.

Finally, the maximum correlation between movable probe and reference probe varies from 40–60% in helicon and in hydrogen discharges to 100% in argon ECRH discharges, indicating a strong variation of the structure size parallel to the magnetic field, which seems to scale with the ion mass in the case of ECRH plasmas.

In the next section, results from the poloidal probe array are presented. The wave number spectra of the radial transport can be compared to the turbulent structures that were detected by conditional averaging to reveal the contribution of these structures to the overall transport. Also, the cross phase measurements with the poloidal probe array will confirm that small non-zero cross phases appear at large and medium spatial scales, while at small scales ($\sim 2\,\mathrm{cm}$), phases can become larger. The relatively large phase for the hydrogen ECRH discharge is also reproduced with acceptable accuracy.

4.3 Poloidal Structure of the Fluctuations

In frequency spectra, the spatial information can only be recovered if the Taylor hypothesis holds. In toroidal plasmas this means that the poloidal rotation must be so fast that the turbulence is practically "frozen" in the plasma while it is rotated past the stationary probe. In fully developed plasma turbulence, this is not always the case. The only recourse is then to measure the fluctuating quantities at all spatial positions simultaneously. On TJ-K, this is done with the poloidal probe array, which is shown in Fig. 3.12. It has 64 probe tips that are arranged on a flux surface at about half the plasma radius. The positive poloidal direction is defined as counter-clockwise in Fig. 3.12. In the plots, the position $y = 0\,\mathrm{cm}$ corresponds to the top probe No. 1.

The probes were alternatively set up for ion saturation current, floating potential and transport measurements in helicon and microwave discharges with various magnetic fields, gases, gas pressures and heating powers. The achieved plasma parameters and normalised quantities are given in Secs. 3.4.1 and 3.4.2. All measurements were done with a sampling frequency of 1 MHz and 1048576 samples per channel. For the transport measurement, the probes were alternatingly set up for ion saturation current and floating potential measurements. This halves the spatial resolution compared to pure ion saturation current or floating potential measurements, which is why the pure measurements were carried out in addition to the transport measurements.

The main points of interest are the poloidal autocorrelation length L_{corr}, the wave number spectra of density, potential and transport fluctuations and the wave number spectra of the mean transport, with special attention to the cross phases between density and potential. A cross phase near zero indicates drift wave dynamics, while a phase near $\pi/2$ indicates MHD interchange modes.

In order to benefit from the high spatial resolution, all 64 probes are used for computing wave number spectra and correlation functions. The averaging over a flux surface that this implies can however bury important differences between e.g. the high- and low-field side of the plasma. This is detected by computing the poloidal correlation lengths for the 32 probes on the high-field and the 32 probes on the low-field side separately. Asymmetries appear to be stronger in helicon discharges.

In the next sections, results from the correlation length analysis will be presented, followed by the analysis of the wave number spectra of the fluctuating quantities (ion saturation current and floating potential) and the scale resolved mean transport Γ, defined in Eq. (2.18).

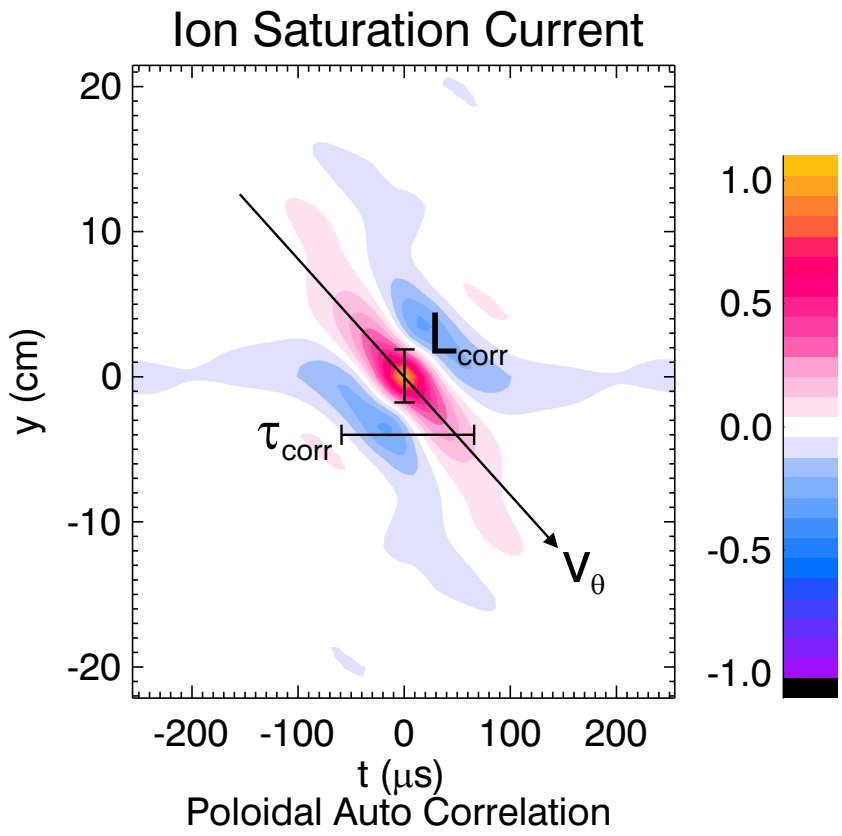

Figure 4.17: Typical auto correlation function in space and time of an ECRH discharge in helium. The y coordinate is along a flux surface at a fixed toroidal position. The correlation length L_{corr}, correlation time τ_{corr} and phase velocity v_θ are defined in the text.

4.3.1 Autocorrelation Functions

Figure 4.17 shows a typical auto correlation function $C(y,t)$ in space and time of an ion saturation current measurement. The poloidal phase velocity v_θ is defined as the displacement of the location of the correlation maximum over time. The auto correlation length L_{corr} is the full width at half the maximum (FWHM) of the correlation function *at a time lag of 0 s*, while the correlation time τ_{corr} is the total life time of the structure. It is computed by taking the FWHM of the projection $C_{proj} = \max_{y\in\mathbb{R}}\{C(y,t)\}$ onto the time axis. This asymmetry between time and space comes from the picture of a localised blob that propagates in time. Some discharges have periodic auto correlation functions, either in the y or t direction, usually when there is a

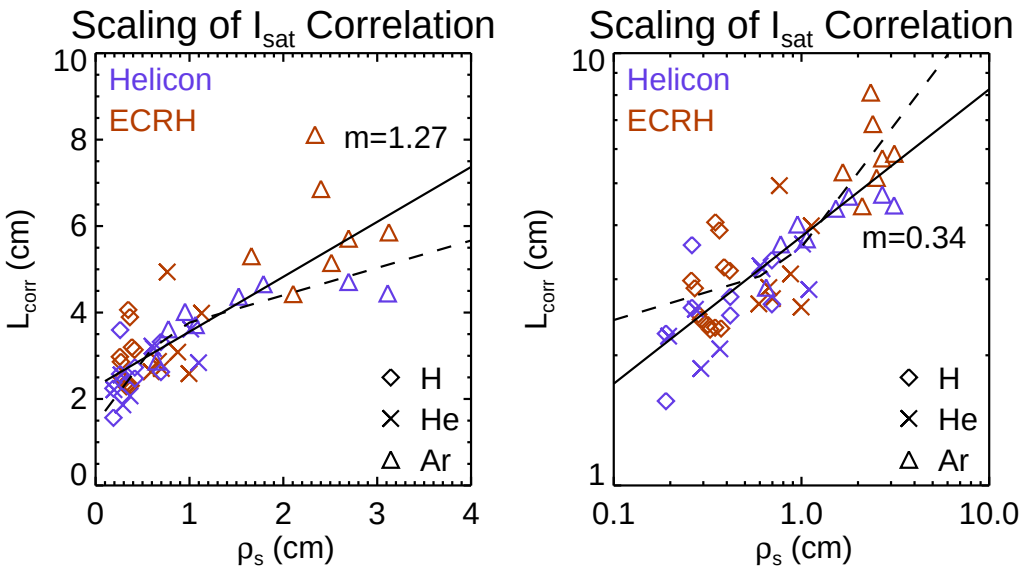

Figure 4.18: Poloidal correlation lengths for helicon (blue) and ECRH (red) discharges as measured by the probe array. The data illustrate the relation between drift scale and L_{corr}. The solid black line represents the linear fit $m\rho_s$ (left) and the power-law fit ρ_s^m (right) to the data. The dashed lines show the linear fit in the log-log plot and vice versa.

dominant mode in the spectrum.

The main results for the correlation analysis are given in Fig. 4.18. The density correlation length is plotted as a function of the drift scale ρ_s. While at first glance the linear relationship seems obvious, the sum of the squared differences is practically the same for the power law fit that goes as $\rho_s^{1/3}$. The spatial resolution limit of the array is ≈ 1.25 cm, which is two times the distance between probes. It is nearly reached for the small values of L_{corr}.

At the other end of the scale, the poloidal size would allow correlation lengths as large as 40 cm. If one has the picture of the blobs being rotating eddies, the poloidal size might however be limited by the radial size of the plasma (typically 5–10 cm). Hence, suppressing data with $L_{corr} \geq 4$ cm yields a linear fit coefficient of $m \approx 3$ and a power-law fit of $m = \approx 0.5$.

The calculation of $\rho_s \propto \sqrt{T/m_i}/B$ is relatively robust: ion mass and magnetic field are well known. The electron temperature is more error-prone, but the dependence is weak. There is a clear trend that increasing ρ_s is followed by increasing density structure sizes. A similar relationship holds for the potential structure sizes. Helicon and ECRH discharges show the same scaling behaviour.

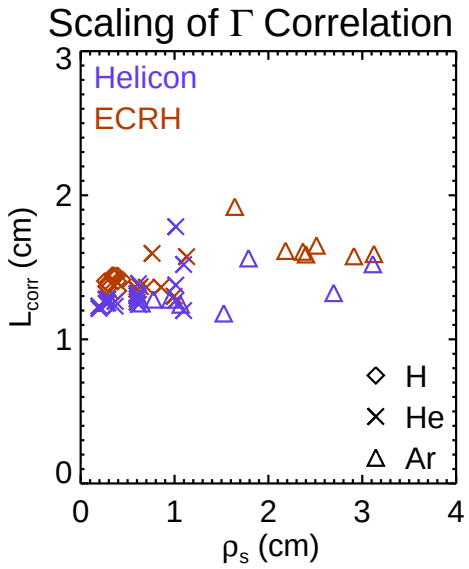

Figure 4.19: Poloidal correlation lengths for transport events in helicon (blue) and ECRH (red) discharges. The data illustrate the independence of L_{corr} on the drift scale, which may be due to the resolution limit (1.25 cm) of the array.

The transport correlation lengths shown in Fig. 4.19 does not display a ρ_s dependence. However, most of the data points are at the resolution limit for the array, which is twice as large in transport mode because two probes are needed for one measurement point. The auto correlation is 1 at $y = 0$ and about zero at the neighbouring measurement points, causing the FWHM to be interpolated to two times the distance between probes, which is about 1.25 cm. Apart from the fact that transport correlation lengths are much smaller than density correlation lengths, no quantitative statement can be made. As has been established in Sec. 2.2, the transport fluctuations are not a measure of the net or mean transport. It is therefore not necessary that their correlation lengths reflect the size of the density blobs that are responsible for the transport. As will be seen in Sec. 4.3.2, the transport fluctuation spectrum is dominated by the wave number-doubled oscillations, which causes the correlation length to be very short.

The poloidal variation of the correlation length is shown in Fig. 4.20. There is a general trend for all investigated plasmas that the outboard (low-field) side has about 50% larger correlation lengths. Helicon discharges have more scatter, while ECRH discharges are more tightly clustered except for argon, which has especially large outboard correlation lengths compared to

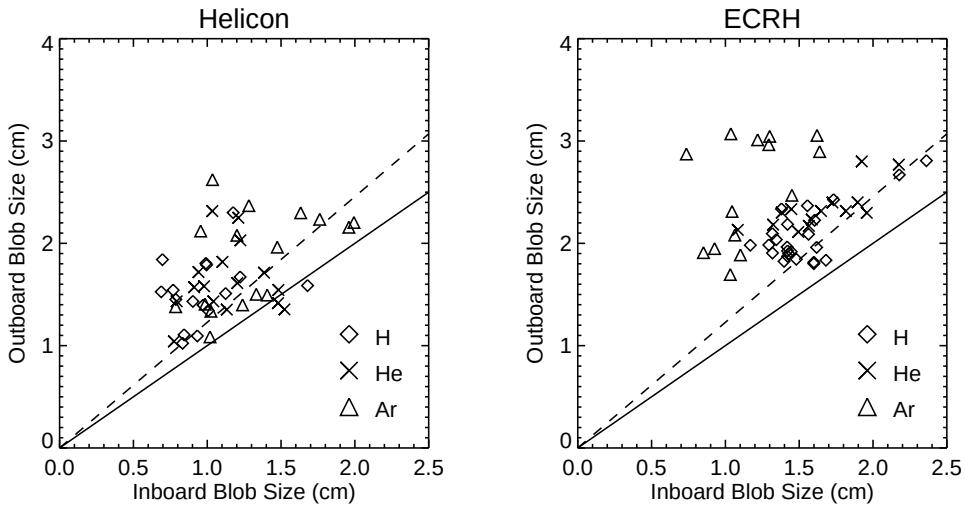

Figure 4.20: Poloidal correlation lengths for the density on the inboard and outboard side. The dashed line shows how the gyro radii and the drift scale ρ_s are smaller on the inboard side where the magnetic field is stronger.

the inboard correlation lengths. The dashed line in the figure gives the correction to the gyro radius and the drift scale, which is 20% smaller on the inboard side with its higher magnetic field strength and smaller on the outboard side. This explains some of the enlargement of structure sizes observed on the outboard side.

Nevertheless, these results show that the poloidal variation of the turbulence structure is moderate and that meaningful results are obtained when averages over the whole flux surface are taken.

4.3.2 Poloidal Wave Number Spectra

The poloidal wave number spectra presented in this section carry all information on the spatial scales of the fluctuations. The measurements that were conducted in TJ-K concentrate on the low and intermediate wave numbers (from the plasma size to the plasma size divided by the number of probes). In the following, the spectral properties of a particular ECRH discharge in helium are given as a generic example of turbulent spectra in TJ-K. In the next sections, the variations of the spectra with the different gases and heating systems is treated in detail. In Sec. 4.3.5, spectra from simulated drift wave turbulence are investigated for comparison.

Figure 4.21 shows spectra from a particularly nice ECRH discharge in helium at $B = 89\,\mathrm{mT}$, neutral pressure $p_0 = 2\times10^{-5}\,\mathrm{mbar}$ and heating power $P = 1.8\,\mathrm{kW}$. The achieved density is $n = 1.2 \times 10^{18}\,\mathrm{m}^{-3}$ and the electron temperature is $T_e = 19\,\mathrm{eV}$. Floating potential, ion saturation current and transport were measured in shots #1887, #1890 and #1893, respectively.

In the top left, the k-f-spectrum of the ion saturation current fluctuations is shown. It displays the broadband features of fully developed turbulence [12], where each wave number has a broad range of frequencies and the fluctuation power is concentrated at low wave numbers and low frequencies. In particular, no linear dispersion relation of e.g. linear drift waves or interchange modes is visible.

The radial transport fluctuations Γ_{fl} have their peak power at low frequencies and high wave numbers. The transport fluctuations show where the transport oscillates most, not where most of the transport happens. In Sec. 2.2, the *mean transport* Γ was introduced as a measure of the contribution of a particular wave number to the overall transport. The difference is revealed in the wave number spectra shown in Fig. 4.21. The fluctuations of the directly measured quantities (ion saturation current and floating potential) have the highest fluctuation level at small wave numbers. The poloidal electric field $E_\theta \approx \nabla\Phi_{float}$ has its peak shifted to intermediate wave numbers by the differentiation. Multiplication with the ion saturation current yields the turbulent transport. Since the multiplication of two oscillating quantities results in oscillations at twice the frequency or wave number, the maximum of the transport fluctuations Γ_{fl} is shifted to even higher wave numbers. But simple oscillations do not cause a net transport. The mean transport Γ is largest at intermediate wave numbers, corresponding to the correlation length of ion saturation current and floating potential.

These three different scales are not at all apparent in the frequency spectra in Fig. 4.21. The power spectra for ion saturation current, floating potential and poloidal electric field are basically the same. The transport fluctuation

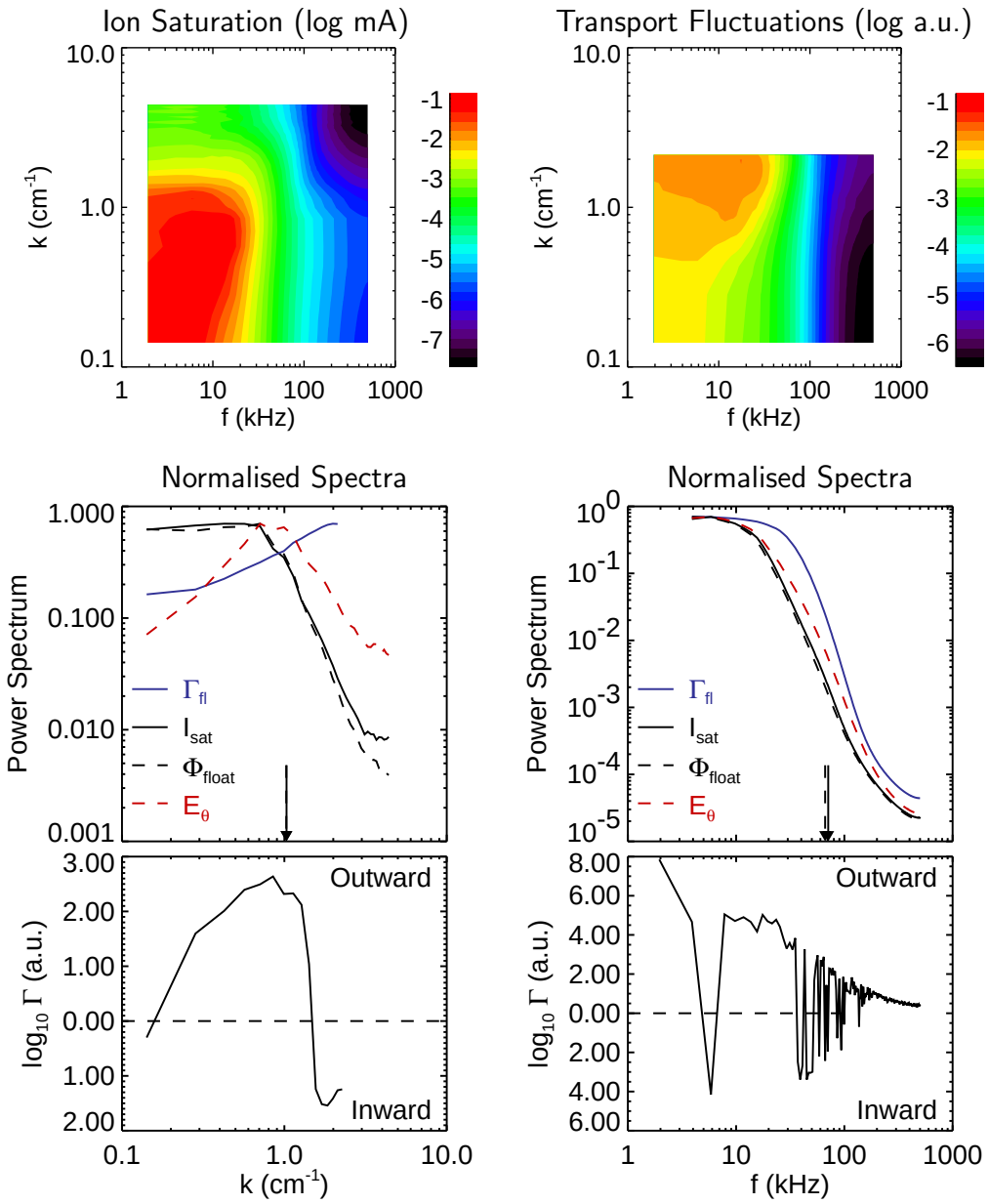

Figure 4.21: Power spectra of a helium ECRH discharge. The upper row shows the wave number and frequency power spectra of ion saturation current and transport fluctuations. Below are the projections of the spectra on the wave number axis (left) and the frequency axis (right). In the wave number spectra, the different scales become evident. The ion saturation current fluctuations have their maximum at small wave numbers, the mean transport Γ *peaks at intermediate wave numbers and the transport fluctuations* Γ_{fl} *are maximal at large wave numbers. The correlation length of the ion saturation current is indicated by the arrow. In contrast, the frequency spectra all peak at low frequencies.*

spectrum is shifted towards higher frequencies for reasons stated above. The mean transport also has its maximum at low frequencies, and it often changes direction. It is clear now that the frequency spectra do not easily allow the recovery of spatial scale information of fluctuations or mean transport.

Nevertheless, frequency spectra have been measured in a variety of fusion devices and their similarity has been noted [79, 76]. One important finding is that self organised criticality should appear in the spectrum with a spectral index of -1. This is not the case in TJ-K discharges. Mean transport frequency spectra were measured in the H-1 Heliac [21], where the transport is concentrated in one very narrow peak, in contrast to the broad spectrum observed in TJ-K.

The turbulence models outlined in Sec. 2.6 make predictions about the wave number spectrum of the flow velocities [2, 5], which is found to have a power law dependence on the wave number k with exponents of -3 and -5/3 (see Figs. 2.8 and 2.9). These exponents are also called *spectral indices*. In fluid turbulence, these spectra are found e.g. in measurements of two dimensional soap films [80] or in three dimensional helium flows [81].

In plasma turbulence, the principal measured quantities are the density and potential fluctuations, not the flow velocities. Since density fluctuations are a consequence of flows, it is reasonable to assume that a similar wave number dependence holds as for the flow velocities. On the other hand, $E \times B$ flow velocities are easily computed from the gradient of the potential fluctuations.

In hot fusion plasmas, wave number power spectra of density fluctuations can be measured by scattering of infra-red laser light or microwaves. For example, in the Tore Supra tokamak, a spectral index of -2.9 was found [19] for the three dimensional power spectrum of the density fluctuations. In the TEXTOR tokamak, a spectral index between -3 and -5.5 was found [82]. The authors conclude that their result is consistent with the spectral index -4 found for large wave numbers in weak drift wave turbulence, calculated in [83]. With Langmuir probe measurements in the scrape-off layer of W7-AS, an index of -3 was found. In all experiments, ten or fewer different wave numbers were measured. Recent results from electromagnetic gyro-kinetic simulations [84] also find a spectral index of about -4 for the density and electron temperature fluctuation power spectrum. This is at variance with the prediction for two dimensional fluid turbulence given in [5].

The wave number spectrum shown in Fig. 4.21 has a constant region at wave numbers $k < 1\,\mathrm{cm}^{-1}$. The power laws hold in the wave number range $k > 1\,\mathrm{cm}^{-1}$, which we call inertial range, in analogy to the Kolmogorov spectra in fluid turbulence. The start of the inertial wave number range is covered by our measurements. In Fig. 4.21, a spectral index of -3 is observed

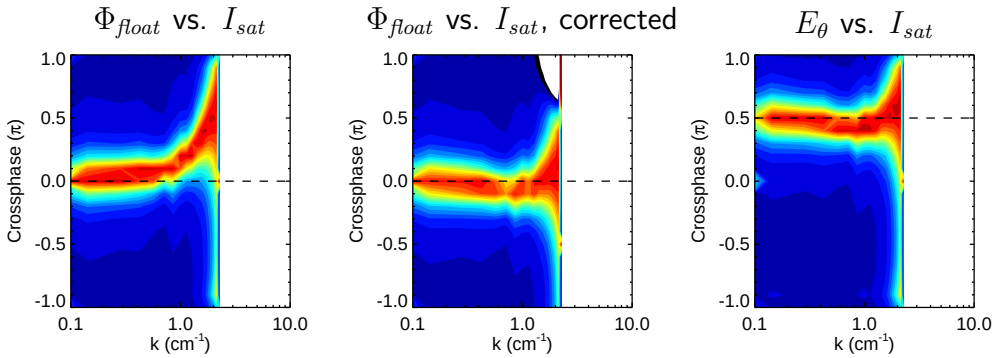

Figure 4.22: Wave number resolved cross phase spectra. The phase difference introduced by the spatial separation between the Φ_{float} and I_{sat} measurements manifests itself in a linear increase in phase difference as the wave number approaches the probe separation (left). The corrected graph is shown in the center. Except for the $\pi/2$ shift introduced by the differentiation, it is identical to the cross phase between electric field and density (right).

for the ion saturation current and the floating potential, while the radial flow velocities, given by E_θ, have an index of -2. These results differ from the predictions given above, and also from experimental results from TEXTOR.

Other discharge, especially the helicon discharges, display different spectral indices in range of -1.5–3 for ion saturation current and floating potential fluctuations. In some discharges, the poloidal electric field shows a constant, noisy spectrum at large wave numbers. Due to the limited wave number range of the probe array, a single mode in the spectrum can totally obscure any underlying power law.

The mean transport Γ has its maximum at intermediate wave numbers. In all discharges, it lies near the wave number that corresponds to the correlation length of the ion saturation current, which is also the near the region where the inertial range starts. In this particular discharge, the transport reverses at large wave numbers. This further supports the notion that the correlation length of the transport fluctuations (shown in Sec. 4.3.1) are not useful for determining the spatial scale of transport events.

The sign of the mean transport is determined by the cross phase between the electric field E_θ and the ion saturation current fluctuations I_{sat}. The wave number resolved cross phase that was used to compute the mean transport in the previous spectra is plotted in Fig. 4.22, which also illustrates a pitfall in determining the cross phase (Eq. 2.21) from measurements. In our setup, the I_{sat} and Φ_{float} probes are interleaved with the distance $\Delta L = 6\,\mathrm{mm}$ between

probes. This means that for wave lengths of 12 mm, we get a phase difference of π between I_{sat} and Φ_{float} just from the displacement between the probes, even if they are in phase. The left graph in Fig. 4.22 shows the raw cross phase. The graph in the middle is compensated by a phase correction of $\Delta\phi = \pi k/k_0$, $k_0 = 2\pi/2\Delta L$.

The computation of the spatial derivative $E_\theta = -\nabla\Phi_{float}$ automatically corrects the phase error, since for every point, two Φ_{float} probes on either side of the I_{sat} probe are used and the result for E_θ is valid exactly at the position of the I_{sat} probe. Consequently, the right graph in Fig. 4.22 is identical to the middle one shifted be $\pi/2$.

The reversal of the mean transport from outward to inward observed in Fig. 4.21 is directly caused by the cross phase going from negative to positive values at $k \approx 1.5\,\mathrm{cm}^{-1}$. It can also be seen that the cross phase is maximally negative where the mean transport is largest ($k \approx 0.9\,\mathrm{cm}^{-1}$).

It should be noted that for drift waves, the cross phase between potential and density fluctuations is expected to be around zero, even in the linearly unstable case [24].

In the following sections, the wave number spectra of ECRH and helicon discharges, as well as results from drift-Alfvén turbulence simulations are presented.

4.3.3 Spectral Properties of Helicon Plasmas

Figure 4.23 shows normalised spectra for argon and helium discharges. Because of ignition problems, there are no hydrogen helicon discharges with the probe array and a helium discharge at a high magnetic field was substituted in order to have a discharge with small drift scale. The drift scales ρ_s for the three discharges are (from left to right) 31, 10 and 3 mm, respectively. The electron temperatures at the radial position of the probes are 12, 13 and 7 eV and the line averaged densities are 6, 4 and $6 \times 10^{17}\,\mathrm{m}^{-3}$.

The spectra are qualitatively similar to those of the ECRH discharge in helium presented in Sec. 4.3.2. A striking difference is the nearly constant spectrum of the poloidal electric field fluctuations E_θ. Also the spectra are generally more noisy and have a spectral index of -2, instead of -3.

The sign of the mean transport Γ in argon oscillates. The low-field helium discharge has inward transport at the ion saturation current correlation length scale, flanked by ranges of outward transport. Alone the high-field helium discharge shows the outward transport maximum at the scale of the ion saturation current correlation length.

The cross phases are broadly scattered around zero. Only the low-field helium discharge shows significant deviations from zero at the scale of the

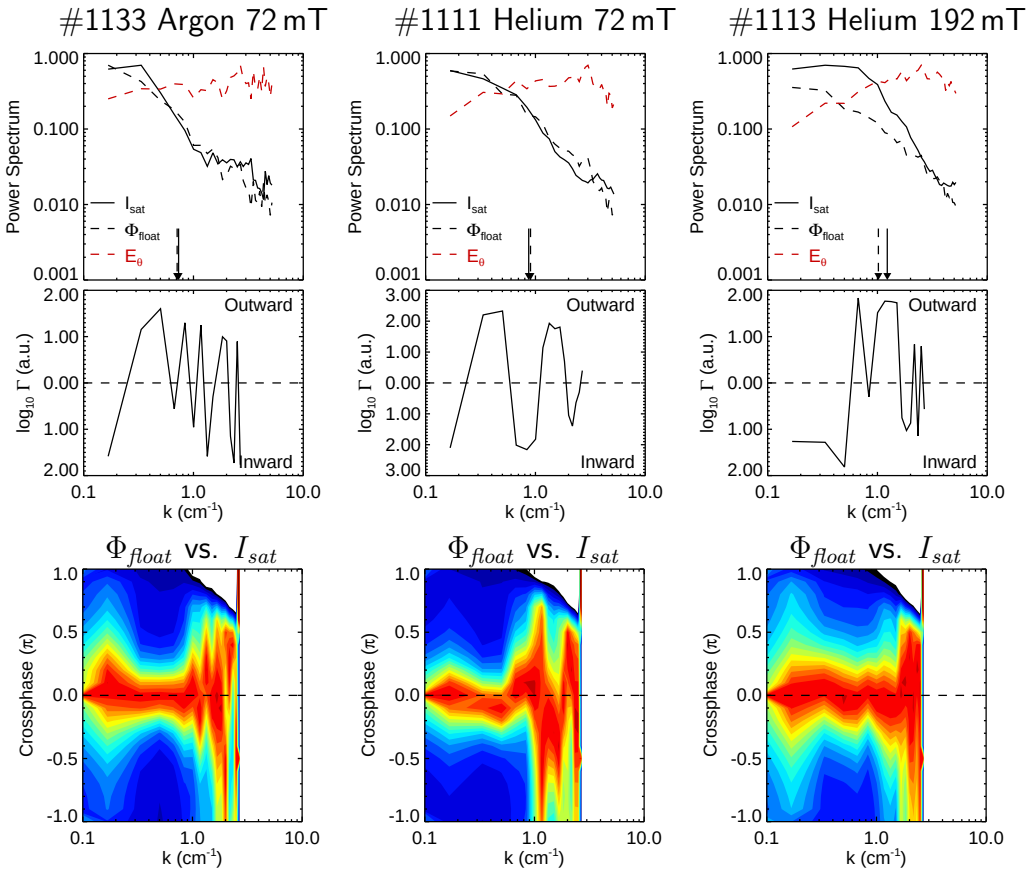

Figure 4.23: Normalised wave number spectra (see Fig. 4.21) and cross phases for helicon discharges. Γ is the mean turbulent transport. The vertical arrows represent the correlation lengths of the respective quantities. The drift scale ρ_s decreases from left to right.

correlation length. At large wave numbers, the phase distribution broadens, which might partly be due to noise. Largely, this behaviour is consistent with the one for ECRH discharges and with drift waves, which would be expected for low-β plasmas.

The drift scaling becomes apparent in Fig. 4.24, where an increasing drift scale ρ_s causes a shift of the ion saturation current spectrum towards larger scales. It is not clear whether the peak in the argon spectrum at large wave numbers is genuine or an artifact of the low signal levels at that scale. When the signal from the plasma fluctuations is low, the diagnostics are particularly susceptible to rf pickup. The power level of $1\text{–}2\times10^{-2}$ might well be the detection limit of the fluctuations and be determined by rf pickup. This

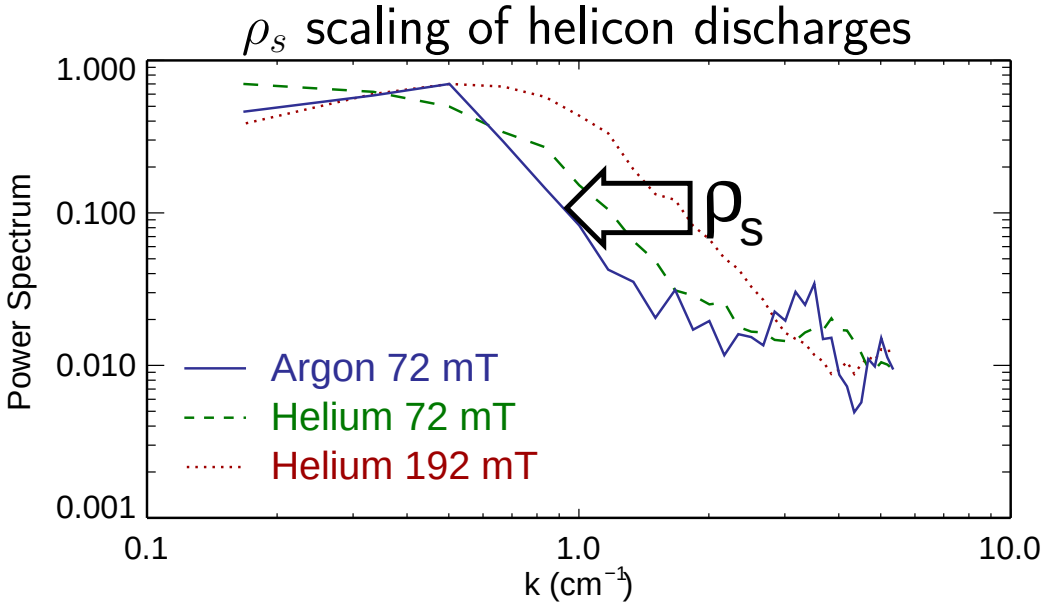

Figure 4.24: Normalised wave number spectra of the ion saturation current from Fig. 4.23, illustrating their dependence on the drift scale ρ_s, which has the values 31, 10 and 3 mm, from left to right.

would explain why the spectra do not decrease further to smaller scales and why the cross phase scatters over $\pm\pi$. The beginnings of similar peaks are also present in the two helium discharges.

In Sec. 4.2, turbulent structures were detected by conditional averaging. The results are compared to the wave number spectra of the mean transport which were taken at the same discharge parameters. The argon spectrum is shown in Fig. 4.23, the helium spectrum is not plotted here. For argon and helium, outward moving structures were found at $k \approx 0.3\,\mathrm{cm}^{-1}$ and $k \approx 0.6\,\mathrm{cm}^{-1}$, respectively, which is reproduced in the mean transport spectra.

4.3.4 Spectral Properties of ECRH Plasmas

Due to the absence of rf noise, the ECRH data have a much higher quality. Figure 4.25 shows normalised spectra for argon, helium and hydrogen discharges. The drift scales ρ_s for the three discharges are (from left to right) 31, 10 and 3 mm, respectively. The electron temperatures at the radial position of the probes are 12, 19 and 7 eV and the line averaged densities are 1.5, 1.2 and $1.1 \times 10^{18}\,\mathrm{m}^{-3}$. Except for the higher density, these parameters are very similar to those of the three helicon discharges presented in the previous

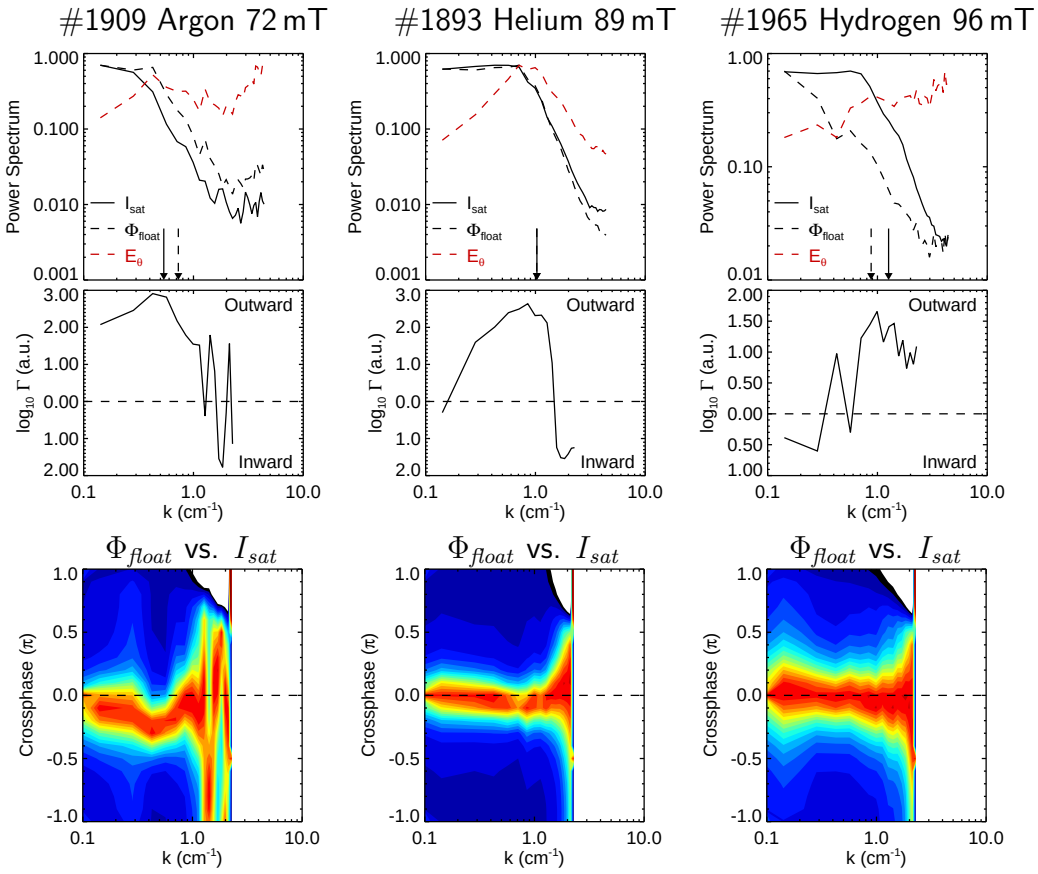

Figure 4.25: Normalised wave number spectra (see Fig. 4.21) and cross phases for ECRH discharges. Γ is the mean turbulent transport. The vertical arrows represent the correlation lengths of the respective quantities.

section.

The helium discharge was already treated in Sec. 4.3.2. In contrast to helium, the poloidal electric field in the argon and hydrogen discharges does not fall off towards large wave numbers. The spectral index of the hydrogen discharge is somewhat smaller then -3.

For all discharges, the mean transport Γ is mainly outward. Its maximum lies at the scale of the correlation length of the ion saturation current, which is very similar to that of the floating potential. This means that the transport scale changes according to the drift scale ρ_s. This striking ρ_s-scaling is also observed for the ion saturation current fluctuations, as shown in Fig. 4.26.

The cross phase is tightly clustered around zero, only argon displays a large noisy scatter at large wave numbers. The other gases also display a

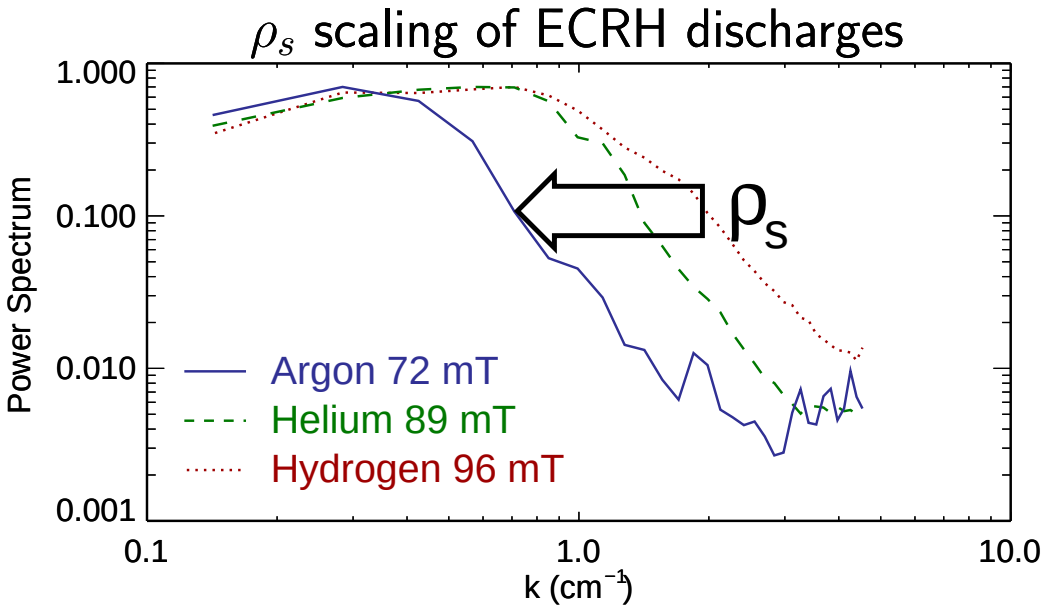

Figure 4.26: Normalised wave number spectra of the ion saturation current from Fig. 4.25, illustrating their dependence on the drift scale ρ_s, which has the values 31, 10 and 3 mm, from left to right.

small systematic broadening of the phase distribution. As expected for low-β plasmas, this behaviour is consistent with drift waves.

In Sec. 4.2, turbulent structures were detected by conditional averaging. The results were compared to the wave number spectra of the mean transport which were taken at the same discharge parameters. The spectra are not plotted here. For argon, a large quasi-coherent mode with $k \approx 0.4\,\mathrm{cm}^{-1}$ was found to propagate very slightly inward. This is at variance with the mean transport spectra, which has its maximum outward transport here. In this case, the structure detected by conditional averaging is not responsible for this transport.

In helium, outward moving structures were found at $k \approx 0.6\,\mathrm{cm}^{-1}$ and inward moving structures were found at $k \approx 1.5\,\mathrm{cm}^{-1}$. This agrees very well with the extrema of the mean transport spectrum. In hydrogen, outward transport was found at $k \approx 0.9\,\mathrm{cm}^{-1}$, $k \approx 1.0\,\mathrm{cm}^{-1}$ and (tentatively) at $k \approx 3.1\,\mathrm{cm}^{-1}$, in agreement with the mean transport spectrum. The cross phase of 0.2π for the first two wave numbers found with the probe array is reasonably close to the $\pi/4$ found by conditional averaging. The last wave number is past the resolution limit of the probe array when it is set up for transport measurements.

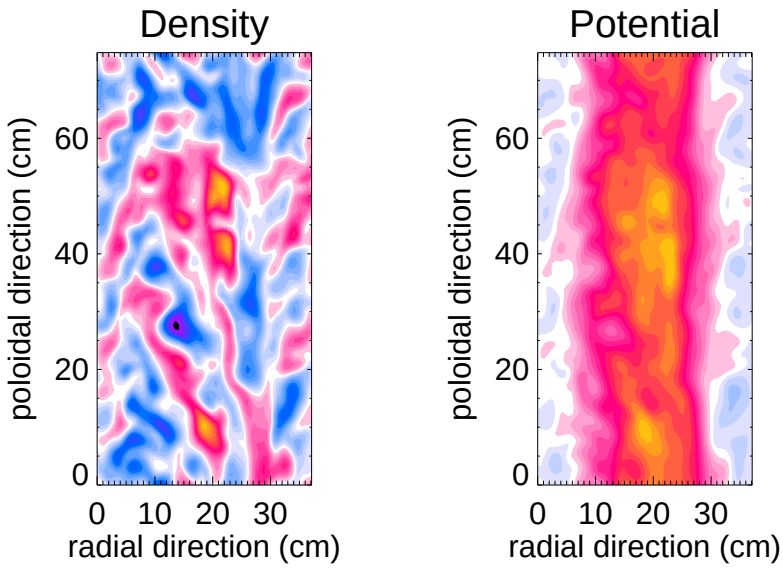

Figure 4.27: Density and potential plot of simulated turbulence in the poloidal plane with the DALF3 simulation code. The radial coordinate range is located in the region of the density gradient with positive values going radially outward.

4.3.5 Spectral Properties of Simulated Plasmas

The DALF3 code (see Sec. 2.1.5) simulates plasma turbulence in three dimensions. Simulations were carried out for dimensionless parameters similar to the ones in the experiments. Details can be found in [25, 24, 85]. A snapshot of the density and potential fluctuations in a poloidal plane is shown in Fig. 4.27. Because of the flux tube geometry, only a fraction of the whole radial and poloidal range is simulated. The three prominent density maxima have corresponding potential maxima, hinting a cross phase between density and potential near zero. The large poloidal structure in the potential is due to a zonal flow [86].

The wave number spectra considered here are taken from a scan of the collisionality parameter $\hat{\nu} \in [4, 8, 12]$ at a normalised plasma beta of 0.75 and a drift scale of $\rho_s = 6\,\mathrm{mm}$ [24]. The power spectra of density and potential fluctuations (Fig. 4.28) are all similar with a power law decay of k^{-6} for large wave numbers and a much shallower decrease at small wave numbers $k < 0.2\,\mathrm{cm}^{-1}$.

The mean transport Γ has a maximum at small wave numbers. It stays at a high level up to intermediate wave numbers, until the inertial range for

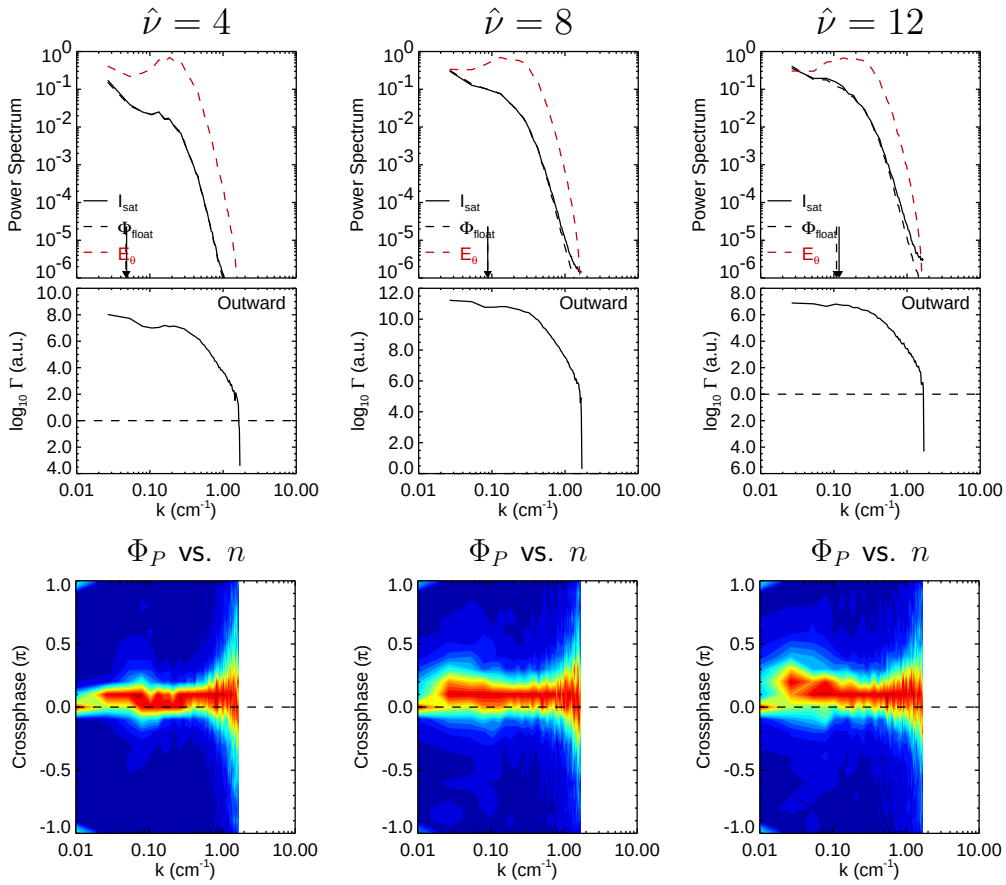

Figure 4.28: Normalised wave number spectra (see Fig. 4.21) and cross phases for simulated turbulence. Γ is the mean turbulent transport. The vertical arrows represent the correlation lengths of the respective quantities.

density and potential fluctuations starts. It then sharply decreases by seven orders of magnitude towards high k, but practically always stays positive (outward). Judging from the location of the inertial range, a similar wave number range as in the experimental investigations was covered. In contrast to the experimental spectra, the transport maximum is located at small wave numbers well below the start of the inertial range. Similar to the experimental results, the transport is maximum around wave numbers corresponding to the density correlation length. It should be noted that, in contrast to the experimental spectra, the lowest wave number does not correspond to one poloidal circumference, but only a fraction thereof. The poloidal scale of the transport events is still considerably smaller than the whole poloidal torus size.

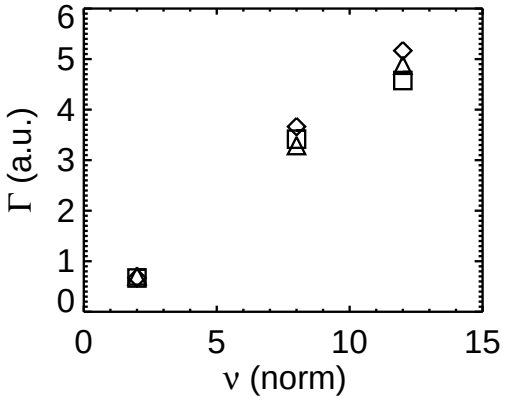

Figure 4.29: Dependence of the total radial transport Γ *on the collisionality* ν *in simulated plasma turbulence. The different symbols mark different radial positions.*

As in the experiment, the cross phases are all drift wave like [24]. In contrast to the experimental setup, positive cross phases correspond to (positive) outward transport. The rising collisionality has the effect of raising the cross phase. This is understandable, because in the drift wave picture, collisionality impedes the parallel electron response, which in turn gives rise to a phase difference between density and potential. For the transport, the increased cross phase term has the effect of increasing the transport at all scales. As Fig. 4.29 shows, transport increases linearly with ν.

4.3.6 Discussion of Spectral Properties

All discharges in TJ-K and the simulated data show turbulent wave number spectra. The spectral indices range from -2 to -3 in the experiment and are near -6 in the simulations. The results for the ECRH discharges with spectral indices of -3 for the density fluctuations agree with the findings for two dimensional turbulence [5]. The hydrogen discharge even shows a small range with a value near -5/3. In the helicon discharges, values between -2 and -3 were found, in agreement with either [2] or [5].

The value of -4 as predicted in [83, 84] was not observed. In fusion experiments, values of -3 and -4 have been found for the density fluctuation power spectra in TEXTOR [82] and Tore Supra [19].

The fact that several spectral indices are present in TJ-K plasmas contra-

dicts the notion of a universally valid value for the spectral index. However, models for two or three dimensions are idealised (local injection of energy, incompressible flows, simple geometry). In plasmas, the injection is due to non-linear instabilities [87] at a broad range of scales. Especially in drift wave turbulence, there is non-trivial coupling between the parallel and perpendicular dynamics, resulting in a mix of two and three dimensional dynamics. The complicated geometry present in fusion plasmas adds further complications. The clear difference between experiment and simulation in the spectral indices (-3 vs. -6) is intriguing and should be examined further.

The measurement of both density fluctuations and transport enabled the comparison of density structure sizes and transport scales. It was found for most discharges, especially ECHR plasmas, that the correlation length of the ion saturation current determined the scale at which the mean transport was maximal. This is also true for the simulated turbulence. In the experiment, the scale of maximum transport was smaller than the scale of largest density or potential fluctuations. The experimental mean transport spectra were almost always in agreement with the coherent structures found by conditional averaging.

Furthermore, it was found that the mean transport and the ion saturation current spectra are shifted in the wave number range according to the drift scale ρ_s. Combined with the ρ_s scaling of the poloidal correlation lengths, this highlights the importance that this quantity has for the turbulence dynamics.

Substantial inward transport was only observed in the experiment. It might be linked to an inward particle transport (inward pinch), which is observed in many fusion experiments [88, 89, 90].

The cross phase between density and potential was found to be drift wave like for practically all discharges. In the simulation, the same behaviour was found. This differs from results found in fusion experiments, where phases close to $\pi/2$ are found. Specifically, measurements with Langmuir probes in the scrape-off layer of W7-AS have found values of $\pi/2$ [78, 20]. Phases of up to $\pi/3$ were found in the confinement region of the TJ-I tokamak [54]. Conditional averaging studies in the DIII-D tokamak found density blobs coinciding with poloidal electric field peaks, which means the cross phase between density and potential is around $\pi/2$. On the other hand, investigations of weak drift wave turbulence in a cylindrical plasma yields cross phases of zero [91].

Chapter 5

Conclusions

The turbulent fluctuations of density and potential and the turbulent transport in magnetically confined plasma of the torsatron TJ-K was investigated using Langmuir probe arrays and drift-Alfvén turbulence simulations. TJ-K has a helicon (rf) and an ECRH (microwave) heating system. Discharges in hydrogen, helium and argon were studied, which allows to assess the theoretically predicted variation of the turbulent scales with the drift scale ρ_s.

In order to identify the spatial scales of fluctuations and transport, a poloidal Langmuir probe array with 64 probes was employed. From the comparison of the density fluctuation wave number spectrum and the spectrum of the actual mean transport conclusions were drawn on the the type of density structures that are responsible for the transport. In earlier measurements of wave number spectra in fusion devices, only the density fluctuation power spectrum was available via scattering diagnostics.

The turbulent wave number spectra of density and potential in TJ-K and in the simulation have a typical Kolmogorov-like shape with a power law decrease $\propto k^m$ at large wave numbers. In analogy to fluid turbulence, this wave number range is referred to as the inertial range. The spectral index m for density fluctuations found in the experimental data varies from -2 to -3. In the well documented ECRH discharges, a spectral index near -3 was always observed. This is in agreement with analytical models of two dimensional fluid turbulence, which predict values of -5/3 and -3. In W7-AS, an index of -3 was found in the scrape-off layer. Other fusion devices (Tore Supra and TEXTOR) report values near -3 and -4 at large wave numbers, where the latter is in agreement with theoretical predictions for weak drift wave turbulence.

In the simulations, a spectral index of -6 was found, which is a very large deviation both from analytical theoretical predictions and from results found in other numerical simulations.

One major result from experiment as well as from simulation is that the maximum transport takes place at scales that are determined by the correlation length of the density. In the experiment, this maximum was near the start of the inertial range, while in the simulations, the maximum was at wave numbers well below the start of the inertial range. In some discharges, the radial transport is inward at some wave number ranges. In the ECRH discharges, this might by related to an inwards particle pinch. These results stress the importance of simultaneous wave number resolved measurements of the density structures whose propagation ultimately is responsible for plasma transport, and the measurement of the actual transport that is caused by these structures. These results are not available for fusion plasmas.

In the experiments, the drift scale ρ_s was varied between 3 and 31 mm by using gases with different atomic masses. It was found that the main features in the wave number spectra are shifted according to the change in ρ_s. The correlation length of the ion saturation current was found to scale with ρ_s, in agreement with theory. The drift scale was thus found to be an important scale parameter for the turbulence in TJ-K.

The cross phase between density and potential fluctuations determines the radial transport. In practically all discharges, the cross phase was very small, which is a clear sign that drift wave turbulence is dominating the dynamics. The same result was found in the simulated turbulence. In other fusion experiments, large cross phases of up to $\pi/2$ are reported. While most of the results are from the scrape-off layer, one is from the plasma confinement region of TJ-I, hinting at a different underlying dynamic process.

The wave number spectra measurements were complemented by radially and poloidally resolved conditional averaging measurements of density and potential fluctuations. The advantage of the conditional averaging method is that it allows the taking of spatially resolved data in one, two or three dimensions without the massive disturbance (and expense) of having hundreds of probes in the plasma. The disadvantage is that only the repetitive, coherent signal with the largest amplitude is detected.

The shape of turbulent structures were characterised at different scales and their radial and poloidal motion was explained in terms of the plasma drifts. Single blob structures were found as well as quasi-coherent modes. In nearly all cases, the radial motion of the detected structures at a particular scale was in agreement with the transport measured by the probe array at the respective scale.

The cross phase was determined by noting the relative position of density and potential extrema in the conditional averaging results. The findings are consistent with the near-zero cross phase found from the probe array measurements.

The conditional averaging method has proven to be a reliable diagnostic method for determining the shape and propagation of large turbulent structures.

In summary, these results are very encouraging. The underlying mechanism for turbulence in TJ-K has been identified as drift waves and the scale of the turbulent transport has been found to be determined by the scale of the density fluctuation. Both scales scale with the drift radius ρ_s. The spectral indices of the experimental wave number spectra are in agreement with theoretical predictions.

In the future, experiments with larger probe arrays (128 probes) and/or smaller probe separations are suggested to investigate regions of larger wave numbers. A two dimensional probe arrangement is currently being employed to allow simultaneous radial and poloidal measurements. In the simulations, the question of the large spectral indices should be addressed.

Bibliography

[1] U. Frisch, *Turbulence* (Cambridge University Press, New York, 1995).

[2] A. Kolmogorov, Dokl. Akad. Nauk. SSSR **30**, 9 (1941), reprinted in Proc. R. Soc. Lond. A 434 (1991).

[3] A. Kolmogorov, Dokl. Akad. Nauk. SSSR **31**, 538 (1941).

[4] A. Kolmogorov, Dokl. Akad. Nauk. SSSR **32**, 16 (1941), reprinted in Proc. R. Soc. Lond. A 434 (1991).

[5] R. H. Kraichnan, Phys. Fluids **10**, 1417 (1967).

[6] L. Artsimovich, Nucl. Fusion **12**, 215 (1972).

[7] H. Furth, Nucl. Fusion **15**, 487 (1975).

[8] F. Wagner and U. Stroth, Plasma Phys. Controll. Fusion **35**, 1321 (1993).

[9] J. Callen, Phys. Fluids B **2**, 2869 (1990).

[10] J. Connor, Plasma Phys. Controll. Fusion **35**, B293 (1993).

[11] C. Liewer, Phys. Fluids **25**, 543 (1985).

[12] A. J. Wooton, B. A. Carreras, H. Matsumoto, K. McGuire, W. A. Peebles, *et al.*, Phys. Fluids, B **2**, 2879 (1990).

[13] C. Hidalgo, Plasma Phys. Controll. Fusion **37**, A35 (1995).

[14] B. A. Carreras, IEEE Trans. Plasma Sci. **25**, 1281 (1997).

[15] M. Endler, H. Niedermeyer, L. Giannone, E. Holzhauer, A. Rudyj, *et al.*, Nucl. Fusion **35**, 1307 (1995).

[16] R. J. Fonck, N. Bretz, G. Cosby, R. Durst, E. Mazzucato, *et al.*, Plasma Phys. Controll. Fusion **34**, 1993 (1992).

[17] H. Thomsen, M. Endler, B. J., A. V. Chankin, S. K. Erents, *et al.*, Plasma Phys. **9**, 1233 (2002).

[18] I. Garcia-Cortes, R. Balbin, A. Loarte, J. Bleuel, A. Chankin, S. J. Davies, M. Endler, S. K. Erents, C. Hidalgo, G. F. Matthews, B. van Milligen, and H. Thomsen, Plasma Phys. Controll. Fusion **42**, 389 (2000).

[19] G. Antar, F. Gervais, P. Hennequin, A. Quemeneur, R. Sabot, A. Truc, P. Devynck, C. Fenzi, X. Garbet, and C. Laviron, Plasma Phys. Controll. Fusion **40**, 947 (1998).

[20] J. Bleuel, M. Endler, H. Niedermeyer, M. Schubert, H. Thomsen, *et al.*, New J. Phys. **4**, 38 (2002).

[21] M. G. Shats and D. L. Rudakov, Phys. Rev. Lett. **79**, 2690 (1997).

[22] E. Ascasibar, J. Quin, A. Fraguas, I. Pastor, and J. Herranz, Nucl. Fusion **37**, 851 (1997).

[23] N. Krause, C. Lechte, U. Stroth, S. Niedner, E. Ascasibar, and J. Alonso, Rev. Sci. Instrum. **73**, 3474 (2002).

[24] S. Niedner, B. D. Scott, and U. Stroth, Plasma Phys. Controll. Fusion **44**, 397 (2002).

[25] S. Niedner, Ph.D. thesis, Christian-Albrechts-Universität, Kiel, Germany, 2002.

[26] B. D. Scott, Plasma Phys. Controll. Fusion **34**, 1977 (1992).

[27] B. D. Scott, Plasma Phys. Controll. Fusion **39**, 471 (1997).

[28] C. Lechte, J. Stöber, and U. Stroth, Plasma Phys. **9**, 2839 (2002).

[29] A. Hasegawa and K. Mima, Phys. Fluids **21**, 87 (1978).

[30] K. Nishikawa and M. Wakatani, *Plasma Physics* (Springer, Berlin, 2000).

[31] M. Wakatani and A. Hasegawa, Phys. Fluids **27**, 611 (1984).

[32] A. Yoshizawa, S.-I. Itoh, K. Itoh, and Y. Nobumitsu, Plasma Phys. Controll. Fusion **43**, R1 (2001).

[33] A. Kendl and B. Scott, Phys. Rev. Lett. **90**, 35006 (2003).

[34] S. Chandrasekhar, *Hydrodynamic and Hydromagnetic Stability* (Oxford University Press, London, England, 1961).

[35] F. Chen, Phys. Fluids **8**, 912 (1965).

[36] W. Horton, Rev. Mod. Phys. **71**, 735 (1999).

[37] D. Block and A. Piel, Plasma Phys. Controll. Fusion **45**, 427 (2003).

[38] E. jin Kim and P. H. Diamond, Plasma Phys. **10**, 1698 (2003).

[39] J. Nührenberg, W. Lotz, and S. Gori, in *Theory of Fusion Plasmas*, edited by E. Sidoni, F. Troyon, and J. Vaclavik (SIF, Bologna, 1994).

[40] G. Van Oost *et al.*, Plasma Phys. Controll. Fusion **45**, 621 (2003).

[41] F. Wagner, G. Becker, K. Behringer, D. Campbell, W. Eberhagen, *et al.*, Phys. Rev. Lett. **49**, 1408 (1982).

[42] U. Stroth, K. Itoh, S.-I. Itoh, H. Hartfuß, and H. Laqua, Phys. Rev. Lett. **86**, 5910 (2001).

[43] M. Hirsch, P. Amadeo, M. Anton, J. Baldzuhn, R. Brakel, J. Bleuel, S. Fiedler, T. Geist, P. Grigull, H. J. HartfuB, E. Holzhauer, R. Jaenicke, M. Kick, J. Kisslinger, J. Koponen, F. Wagner, H. Wobig, and S. Zoletnik, (1997), IAEA Technical Committee Meeting on H-Mode Physics (6th Workshop), 22 - 24 Sept 1997, Seeon FRG, submitted to Plasma Phys. Control. Fusion.

[44] U. Stroth, K. Itoh, S.-I. Itoh, H. Hartfuß, and H. Laqua, J. Plasma Fus. Res. Series **4**, 43 (2002).

[45] C. Hidalgo, M. A. Pedrosa, E. Sanchez, R. Balbin, A. Lopez-Fraguas, *et al.*, Plasma Phys. Controll. Fusion **42**, A153 (2000).

[46] T. Dudok de Wit and V. Krasnosel'skikh, Nonl. Proc. Geoph. **3**, 262 (1996).

[47] W. R. Hamming, in *Introduction to applied numerical analysis* (Hemisphere Publishing Company, New York, 1989), Chap. 12.

[48] C. Ritz *et al.*, Rev. Sci. Instrum. **59**, 1739 (1988).

[49] A. Khintchine, Math. Ann. **109**, 604 (1934).

[50] T. Huld, A. H. Nielsen, H. H. Pecseli, and J. J. Rasmussen, Phys. Fluids B **3**, 1609 (1991).

[51] H. Johnsen, H. L. Pecseli, and J. Trulsen, Phys. Fluids **30**, 2239 (1987).

[52] O. Grulke, Ph.D. thesis, Christian-Albrechts-Universität, Kiel, Germany, 2001.

[53] N. Mahdi-Zadeh, Master's thesis, Christian-Albrechts-Universität, Kiel, Germany, 2003.

[54] B. A. Carreras, C. Hidalgo, E. Sanchez, D. E. Newman, V. E. Lynch, *et al.*, Plasma Phys. **3**, 2664 (1996).

[55] C. Gourdon, *Programme optimise de calculs numerique dans les configurations magnetique toroidales* (CEN, Fontenay aux Roses, 1970).

[56] N. Krause, Ph.D. thesis, Christian-Albrechts-Universität, Kiel, Germany, 2003.

[57] F. Chen and R. W. Boswell, Transact. in Plasma Sci. **25**, 1245 (1997).

[58] G. Borg and R. Boswell, Plasma Phys. **5**, 564 (1998).

[59] R. Boswell and F. Chen, Transact. in Plasma Sci. **25**, 1229 (1997).

[60] M. Michel, Master's thesis, Christian-Albrechts-Universität, Kiel, Germany, 2003.

[61] T. H. Stix, *The Theory of Plasma Waves* (McGraw-Hill, New York, 1962).

[62] J. Stöber, Master's thesis, Christian-Albrechts-Universität, Kiel, Germany, 2001.

[63] H. Hartfuß, T. Geist, and M. Hirsch, Plasma Phys. Controll. Fusion **39**, 1162 (1997).

[64] T. Geist, E. Würsching, and H. Hartfuß, Rev. Sci. Instrum. **68**, 1162 (1997).

[65] N. Hershkowitz, *Plasma Diagnostics* (Academic Press, Boston, 1989).

[66] H. Niedermeyer, M. Endler, L. Giannone, A. Rudyj, G. Theimer, ASDEX team, and W7-AS team, Plasma Phys. **34**, 3614 (1994).

[67] L. Giannone, R. Balbin, H. Niedermeyer, M. Endler, G. Herre, *et al.*, Plasma Phys. **1**, 3614 (1994).

[68] M. Druyvesteyn, Z. Phys. **64**, 781 (1930).

[69] U. Pfeiffer, M. Endler, J. Bleuel, H. Niedermeyer, G. Theimer, and W7-AS Team, Contrib. Plasma Phys. **38**, 134 (1998).

[70] V. I. Demidov, S. V. Ratynskaia, R. J. Armstrong, and K. Rypdal, Physics of Plasmas **6**, 350 (1999).

[71] R. R. Arslanbekov, N. A. Khromov, and A. A. Kudyavtsev, Plasma Sources Sci. Technol. **3**, 528 (1994).

[72] F. Chen, Plasma Sources Sci. **3**, 163 (1994).

[73] R. Westphal, Master's thesis, Christian-Albrechts-Universität, Kiel, Germany, 2002.

[74] H. Stenzel, Master's thesis, Christian-Albrechts-Universität, Kiel, Germany, 2003.

[75] K. Rahbarnia, Master's thesis, Christian-Albrechts-Universität, Kiel, Germany, 2003, in preperation.

[76] M. A. Pedrosa, C. Hidalgo, B. A. Carreras, R. Balbin, I. Garcia-Cortez, *et al.*, Phys. Rev. Lett. **82**, 3621 (1999).

[77] C. Lechte, S. Niedner, and U. Stroth, New J. Phys. **4**, 34 (2002).

[78] O. Grulke, T. Klinger, M. Endler, A. Piel, and W7-AS Team, Plasma Phys. **8**, 5171 (2001).

[79] B. A. Carreras, R. Balbin, B. van Milligen, J. Bleuel, M. Endler, A. Chankin, *et al.*, Plasma Phys. **6**, 4615 (1999).

[80] M. Rutgers, Phys. Rev. Lett. **81**, 2244 (1998).

[81] F. Champagne, J. Fluid Mech. **86**, 67 (1978).

[82] H. van Andel, A. Boileau, and M. von Hellermann, Plasma Phys. Controll. Fusion **29**, 49 (1987).

[83] A. Rogister and G. Hasselberg, Phys. Fluids **26**, 1467 (1983).

[84] F. Jenko and A. Kendl, New J. Phys. **4**, 35.1 (2002).

[85] S. Niedner, C. Lechte, U. Stroth, N. Krause, B. Scott, and J. Stöber, in *Proc. of the ISSS-6, Garching*, edited by M. S. J. Büchner, C.T. Dumm (Copernicus Gesellschaft, Katlenburg-Lindau, Germany, 2001), p. 202.

[86] M. Ramisch, U. Stroth, S. Niedner, and B. Scott, New J. Phys. **5**, 12 (2003).

[87] B. Scott, New J. Phys. **4**, 52 (2002).

[88] B. Coppi and N. Sharky, Nucl. Fusion **21**, 1363 (1981).

[89] D. R. Baker, M. R. Wage, G. L. Jackson, R. Maingi, R. E. Stockdale, *et al.*, Nucl. Fusion **38**, 485 (1998).

[90] U. Stroth, T. Geist, J. P. T. Koponen, H. J. Hartfuß, and P. Zeiler, Phys. Rev. Lett. **82**, 928 (1999).

[91] O. Grulke, T. Klinger, and A. Piel, Plasma Phys. **6**, 788 (1999).

Acknowledgements

This work would not have been possible without the support of many people and organisations. I thank Ulrich Stroth for taking me into his research group and providing the challenge of this work and the means for accomplishing it. Nils Krause, Sven Niedner, Franko Greiner, Mirko Ramisch, Navid Mahdi-Zadeh and also Marco Michel and Kian Rahbarnia have supported me in the lab by working with me on the experiment and discussing all the aspects of plasma turbulence. All our analysis work was made easier be the free exchange of IDL and LaTeX code snippets.

Experimental physics needs hardware to run on. I thank the CIEMAT, Madrid, for supplying us with the TJ-1U device, which is the foundation of TJ-K. Alexander Piel has provided us with the data acquisition system used for the probe array. Without him, a major part of this work would not have been possible. Finally, the financial support of IPP Garching has helped us greatly in the startup phase of our group.

Much of the hands-on work in the lab was done by our technician Volker Rohwer, who is always helpful. The institute's metal workshop has turned many ideas for diagnostics into reality — sometimes 64-fold.

On the home front, I thank my parents and my physics friends Henning Thomsen, Jörg Riechen and Ernst Lenz, and also my non-physics friends for giving me reasons to sometimes leave the lab.

I also thank Joe Talmadge and David Anderson for letting me broaden my horizon on HSX and for accepting me as a post-doc.

Finally, I thank all the people who have contributed to free (as in speech and in beer) software, for I cannot imagine a world without their operating systems, type-setting and other data processing software. In Extremo have provided the musical background for the final days (and nights) of preparing this document. This probably says a lot.

Eidesstattliche Erklärung

Hiermit erkläre ich an Eides statt, dass die vorliegende Dissertation, abgesehen von der Beratung durch meine wissenschaftlichen Lehrer und der Verwendung der angegebenen Hilfsmittel, nach Inhalt und Form meine eigene ist. Sie hat weder ganz noch zum Teil an einer anderen Stelle im Rahmen eines Prüfungsverfahrens vorgelegen.
Kiel, im April 2003

(Carsten Lechte)